

Microfluidics for Biophysical Studies on Artificial Lipid Membranes

Yahyazadeh Shourabi, A.

DOI

[10.4233/uuid:57912020-277b-421c-a25c-f4340f23ee3c](https://doi.org/10.4233/uuid:57912020-277b-421c-a25c-f4340f23ee3c)

Publication date

2025

Document Version

Final published version

Citation (APA)

Yahyazadeh Shourabi, A. (2025). *Microfluidics for Biophysical Studies on Artificial Lipid Membranes*. [Dissertation (TU Delft), Delft University of Technology]. <https://doi.org/10.4233/uuid:57912020-277b-421c-a25c-f4340f23ee3c>

Important note

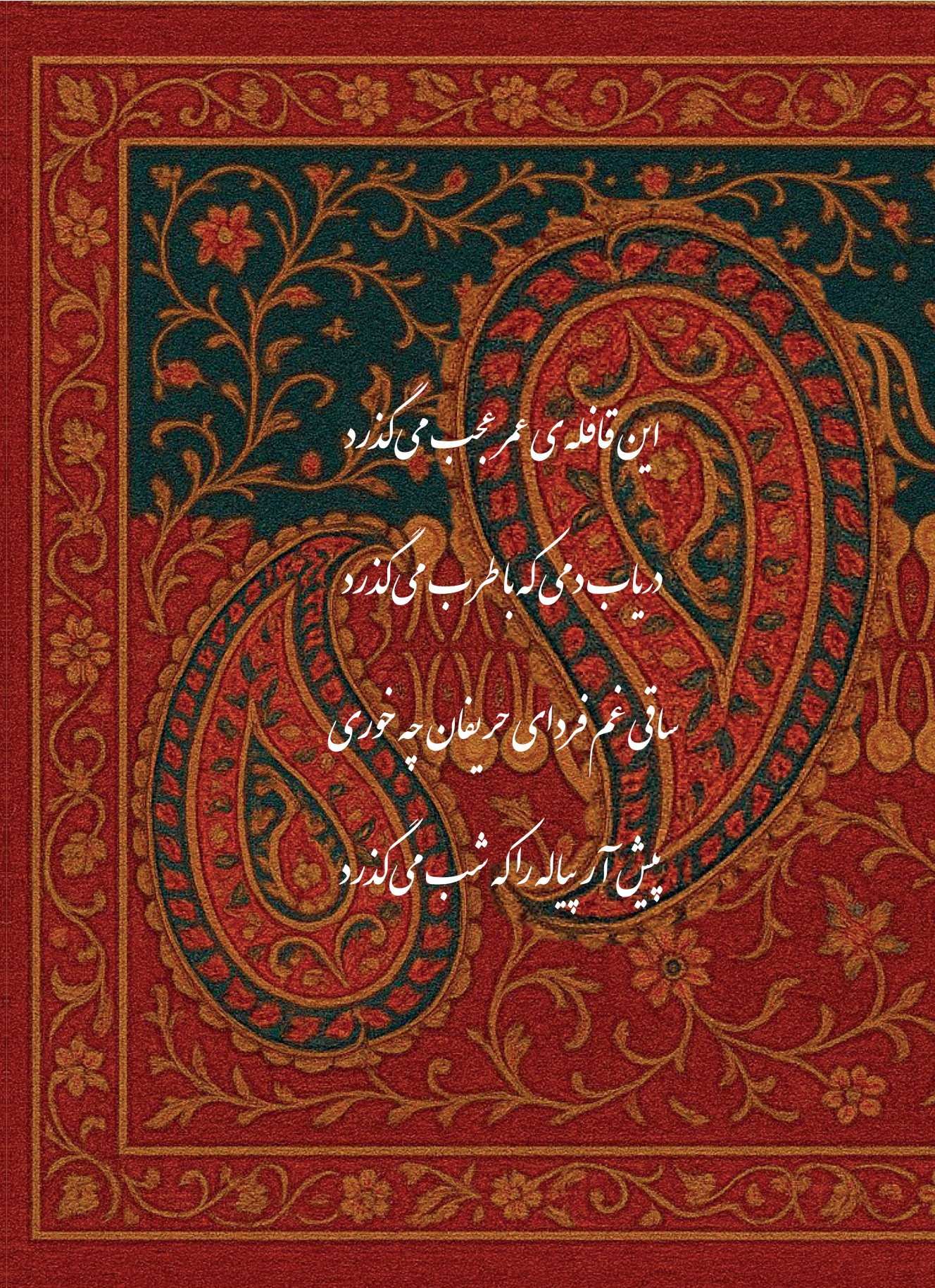
To cite this publication, please use the final published version (if applicable). Please check the document version above.

Copyright

Other than for strictly personal use, it is not permitted to download, forward or distribute the text or part of it, without the consent of the author(s) and/or copyright holder(s), unless the work is under an open content license such as Creative Commons.

Takedown policy

Please contact us and provide details if you believe this document breaches copyrights. We will remove access to the work immediately and investigate your claim.



این قافله می‌عمر عجب می‌گذرد

دریابدمی که با طرب می‌گذرد

ساقی غم فردای حریفان چه خوری

پیش آرزو راه راکه شب می‌گذرد

Microfluidics for Biophysical Studies on Artificial Lipid Membranes

Arash Yahyazadeh Shourabi

Microfluidics for Biophysical Studies on Artificial Lipid Membranes

Dissertation

for the purpose of obtaining the degree of doctor
at Delft University of Technology
by the authority of the Rector Magnificus, Prof. dr ir. T.H.J.J. van der
Hagen,
chair of the Board for the Doctorates
to be defended publicly on
Monday 30th June 2025 at 12 o'clock

by

Arash Yahyazadeh Shourabi

Master of Mechanical Engineering,
Sharif University of Technology, Iran
born in Damavand, Iran

This dissertation has been approved by the promoters.

Composition of the doctoral committee:

Rector Magnificus	chairperson
Dr. M.-E. Aubin-Tam	Delft University of Technology, promotor
Prof. dr. G. Koenderink	Delft University of Technology, promotor

Independent members:

Prof. dr. C. Dekker	Delft University of Technology
Prof. dr. M. Dogterom	Delft University of Technology
Prof. dr. D. Fernandez Rivas	University of Twente
Dr. P. Boukany	Delft University of Technology
Prof. dr. P. Bassereau	Institut Curie, Paris



Keywords: Lipid bilayers, Optical tweezers, Microfluidics, Mechanical properties

Cover: An AI-rendered cell membrane image, depicted in a Persian carpet style, shows molecular transport between its distinct internal and external aqueous environments.

Back cover: Lo, Caravan of Life is on its way,
 The momentary halt Here prize, O pray!
 Why fret about the Rivals' Coming Day -
 Fill up the cup, the evening steals away!
 [By Khayyam – Translation: Edward FitzGerald]

Printed by: Gildeprint

Copyright © 2025 by A. Yahyazadeh Shourabi

ISBN

Casimir PhD Series

An electronic version of this dissertation is available at

<https://repository.tudelft.nl/>

This thesis is dedicated to my mother:

Thank you madaari

Contents

Summary.....	10
Samenvatting.....	15
Chapter 1	20
Introduction.....	20
1.1 Lipid bilayers at the core of artificial cell membranes	21
1.2 Formation of freestanding planar lipid bilayers in microfluidic platforms.....	25
1.3 Characterizing physical properties of lipid membranes	28
1.4 Delivery of particles/drugs to lipid bilayers using microfluidics.....	30
1.5 Challenges and Research Aim.....	32
1.6 Thesis Outline	33
Chapter 2	38
Combination of optical tweezers with lipid bilayers formed on an integrated microfluidic platform	38
2.1 Introduction to optical tweezers	39
2.2 High-throughput formation of freestanding planar membranes.....	42
2.2.1 Microfluidic system description	44
2.2.2 Quantifying the effect of the bubble trap	48
2.3 Conclusion	51
2.4 Methods and Experimental	52
2.4.1 Microfabrication	52
2.4.2 Fabrication of the molds.....	52
2.4.3 Device fabrication protocol	52
2.4.4 Heating and temperature control	53
2.4.5 Optical tweezers experiments.....	53
2.4.6 COMSOL Simulation.....	54

2.4.7 Statistical.....	55
2.5 Supplementary Information	56
Chapter 3	58
Microfluidic system for efficient molecular delivery to artificial cell membranes.....	58
3.1 Introduction	59
3.2 Microfluidic system description	62
3.3 Flow simulation.....	67
3.4 Experimental characterization of media replacement around membranes	74
3.5 Materials and Methods	77
3.5.1 Microfluidic chip fabrication.....	77
3.5.2 Chemicals, buffers, lipids, and flows	79
3.5.3 Numerical simulations	79
3.5.4 Video and image analysis	80
3.6 Supplementary information	81
Chapter 4	84
A single-gap microfluidic chip for electrical characterization of lipid bilayers.....	84
4.1 Introduction	86
4.2 Microfluidics system description and working principles	89
4.3 Device characterization	96
4.4 Lipid membrane formation and electrophysiology on chip	100
4.5 Conclusion	103
4.6 Materials and Methods	103
4.6.1 Master mold fabrication.....	103
4.6.2 Minor mold fabrication.....	104
4.6.3 Microfluidic chip fabrication.....	104
4.6.4 Lipids and buffers	105

4.6.5 Electricals.....	106
4.7 Supplementary information	107
Chapter 5	109
Mechanical characterization of freestanding lipid bilayers with temperature-controlled phase	109
5.1 Introduction.....	111
5.2 Hydrodynamics at the interface of membranes.....	115
5.3 Surface tension and bending rigidity of membranes	121
5.3.1 Membrane tension	124
5.3.2 Lipid nanotube formation.....	126
5.3.3 Bending rigidity.....	129
5.4 Conclusion	130
5.5 Methods and Experimental	132
5.5.1 Thermal chip and temperature control	132
5.5.2 Lipids and membrane formation	132
5.5.3 Optical tweezers experiments.....	133
5.5.4 Image processing for surface tension measurements.....	134
5.5.5 Statistical analysis.....	134
5.6 Supplementary information	135
Chapter 6	142
Effect of lipid tail-asymmetry and cholesterol on the mechanical properties of lipid bilayers.....	142
6.1 Introduction.....	144
6.2 Combining optical tweezers and microfluidics.....	149
6.3 Mechanics of bilayers of lipid molecules varying in tail-asymmetry.....	151
6.3.1 Membrane tension	152
6.3.2 Bead entry into tail-asymmetric bilayers.....	155

6.3.3 Bending rigidity of tail-asymmetric lipid bilayers	158
6.4 Hydrodynamics of lipid bilayers.....	160
6.4.1 Fluid slip at the interface of tail-asymmetric membranes	160
6.4.2 Effect of cholesterol on hydrodynamics at the interface of bilayers of tail- asymmetric lipids.....	166
6.5 Conclusion	170
6.6 Materials and Methods	171
6.6.1 Lipids and membrane formation	171
6.6.2 Optical tweezers experiments.....	172
6.6.3 Image processing for surface tension measurements.....	173
6.6.4 Statistical analysis.....	173
6.5 Supplementary Information	174
Chapter 7	176
Effect of azithromycin on the mechanical properties of POPC membranes	176
7.1 Introduction.....	177
7.2 On-chip delivery of azithromycin to POPC lipid bilayers	178
7.3 Conclusion	184
7.4 Materials and Methods:	184
7.4.1 Chemicals, buffers, lipids, and flows	184
7.4.2 Optical tweezers experiments.....	185
7.4.3 Statistical analysis.....	186
Chapter 8	188
Conclusions and Outlook.....	188
8.1 Conclusion and Outlook.....	189
8.2 Recommendations for future work	196
References	201

Acknowledgements	227
Curriculum Vitae	230
List of Publications.....	231

Summary

Lipid bilayers serve as the fundamental structural components of cell membranes. Despite appearing as a simple two-dimensional material, they possess surprising complexity due to the intricate structure of individual lipid molecules and their interactions within the bilayer. This complexity results in membranes exhibiting diverse microscopic and bulk properties.

For decades, researchers have been developing platforms enabling them to form lipid bilayers as models for artificial cell membranes and characterizing them *in vitro*. However, the stability of such membranes, the flexibility in possible lipid compositions, and the compatibility of these platforms to perform various kinds of biophysical tests has always been an experimental challenge.

In this thesis, I explore different topics related to the biophysics of lipid bilayers utilizing newly developed opto-microfluidics. After an introductory chapter (**Chapter 1**), the thesis is structurally divided in two sections, each containing 3 chapters. The first section (**Chapters 2 to 4**) comprises a description and characterization of the different microfluidic systems that are developed in this thesis. These new tools are used for the biophysical studies on lipid bilayers that are included in the second section (**Chapters 5 to 7**).

In **Chapter 2**, entitled “Combination of optical tweezers with lipid bilayers formed on an integrated microfluidic platform”, I explain the passive bubble trap system and the lipid bilayer formation around micropillars designed in a microfluidic chip. These microfluidic modules are the core of the technical design of this thesis. Since optical tweezers is the main method of membrane biophysical characterization used throughout this thesis, a brief introduction on optical tweezers and its implementation is also provided.

In **Chapter 3**, entitled “Microfluidic system for efficient molecular delivery to artificial cell membranes”, the integrated microchip is further developed to be turned into a drug delivery chip, solving a well-known challenge in microfluidics, i.e. reversible buffer change around lipid bilayers. I describe the concept, design, computational simulation, and experimental characterization of the microchip.

While the microfluidic designs developed in Chapters 2 and 3 are suitable for mechanical characterizations of lipid bilayers, they are not applicable for bilayer electrophysiological measurements. So, in **Chapter 4**, entitled “A single-gap microfluidic chip for electrical characterization of lipid bilayers”, a microfluidic chip design is developed that enables electrical characterization of the bilayers on chip. The chip works based on a novel bidirectional fluidic diode system that balances the fluidic condition at each side of the membrane while keeping the buffer

on both side isolated, preventing them from being mixed, which is essential when performing electrical measurements on the bilayers. As a further advantage, since the solutions of each side of the membrane are isolated, this chip should allow to form and characterize lipid membranes under asymmetric conditions.

Having the developed microfluidic system of Chapter 2 at hand, **Chapter 5** (entitled “Mechanical characterization of freestanding lipid bilayers with temperature-controlled phase”) focuses on thermomechanical properties of membranes with gel-fluid coexisting structures. Phase separation is known to govern the mechanical properties of the cell membrane, influencing protein functioning within the membrane and membrane-drug interaction. Despite its significance, there is a limited amount of literature on the mechanical characterization of such membranes. This scarcity is largely attributed to the low stability of non-fluid lipid bilayers, potential introduction of artifacts by the experimental platform that hinders phase change/separation, and technical issues concerning temperature regulation and control.

The chip developed in Chapter 2 is again used in **Chapter 6** (entitled “Effect of lipid tail-asymmetry and cholesterol on the mechanical properties of lipid bilayers”) to address how tail-asymmetry in the structure of lipid molecules affects the bulk mechanical properties of lipid bilayers. In this chapter, a diverse range of

membranes in fluid, ripple, gel phases with tail-symmetric and tail-asymmetric lipid structures are successfully fabricated on the chip and characterized. The beauty is that the membranes studied here are all single component, which makes it easier to understand how each specific tail-asymmetric lipid molecule contributes to the bulk mechanical properties of the cell membrane, a long-lasting question in bacterial cell membrane research. Additionally, at the end of this chapter, I also investigated how cholesterol affects membranes formed from tail-asymmetric and tail-symmetric membranes.

In **Chapter 7** (entitled “Effect of azithromycin on the mechanical properties of POPC membranes”), I used the microfluidic delivery platform described in chapter 3 to study the effect of an antibiotic, azithromycin, on POPC bilayers as a proof of concept for the developed system. The primary motivation for this chapter is to demonstrate the application of the microfluidic chip in drug-screening studies. Beyond this, while the effect of azithromycin on lipid bilayers has been studied in the literature, it has not been investigated on freestanding planar bilayers. This study provides a unique opportunity to compare the drug’s interactions with the current membrane configuration against those reported in the literature.

Finally, in **Chapter 8**, I recap the key take away of the current piece of work and provide suggestion for later research.

Altogether, the contribution of the present thesis to the field can be viewed from two aspects: First, the novel microfluidic designs that are provided pave the way for a broad set of studies on artificial cell membranes. Second, it reports novel results on the biophysical properties of freestanding lipid bilayers. I hope that this piece of work can contribute to a better understanding of lipid bilayers in cell biology and drug delivery.

Samenvatting

Lipid dubbellagen vormen de fundamentele structurele componenten van celmembranen. Hoewel ze op het eerste gezicht een eenvoudig tweedimensionaal materiaal lijken, hebben ze een verrassende complexiteit door de ingewikkelde structuur van individuele lipidemoleculen en hun interacties binnen de dubbellaag. Deze complexiteit resulteert in membranen met diverse microscopische en bulk-eigenschappen.

Al decennia lang ontwikkelen onderzoekers platforms waarmee ze lipid dubbellagen kunnen vormen als modellen voor kunstmatige celmembranen en deze *in vitro* kunnen karakteriseren. Echter, de stabiliteit van dergelijke membranen, de flexibiliteit in mogelijke lipidesamenstellingen en de compatibiliteit van deze platforms om verschillende soorten biofysische tests uit te voeren, vormen altijd een experimentele uitdaging.

In dit proefschrift onderzoek ik verschillende onderwerpen die verband houden met de biofysica van lipid dubbellagen, gebruikmakend van nieuw ontwikkelde opto-microfluidica. Na een inleidend hoofdstuk (**Hoofdstuk 1**) is het proefschrift

opgedeeld in twee secties, elk bestaande uit drie hoofdstukken. De eerste sectie (**Hoofdstukken 2 tot 4**) beschrijft en karakteriseert de verschillende microfluidische systemen die in dit proefschrift zijn ontwikkeld. Deze nieuwe tools worden gebruikt voor de biofysische studies over lipid dubbellagen, die zijn opgenomen in de tweede sectie (**Hoofdstukken 5 tot 7**).

In **Hoofdstuk 2**, getiteld "Combinatie van optische pincetten met lipid dubbellagen gevormd op een geïntegreerd microfluidisch platform", bespreek ik het passieve bubbelval-systeem en de vorming van lipid dubbellagen rond microzuilen ontworpen in een microfluidische chip. Deze microfluidische modules vormen de kern van het technische ontwerp van dit proefschrift. Aangezien optische pincetten de belangrijkste methode van membraan-biofysische karakterisering zijn die in dit proefschrift wordt gebruikt, wordt ook een korte introductie tot optische pincetten en de implementatie daarvan gegeven.

In **Hoofdstuk 3**, getiteld "Microfluidisch systeem voor efficiënte moleculaire aflevering aan kunstmatige celmembranen", wordt de geïntegreerde microchip verder ontwikkeld tot een geneesmiddelleveringschip, waarmee een bekende uitdaging in microfluidica wordt opgelost, namelijk de omkeerbare bufferwisseling rond lipid dubbellagen. Ik beschrijf het concept, ontwerp, de computationele simulatie en experimentele karakterisering van de microchip.

Hoewel de microfluidische ontwerpen ontwikkeld in Hoofdstukken 2 en 3 geschikt zijn voor mechanische karakterisering van lipid dubbellagen, zijn ze niet toepasbaar voor elektro-fysiologische metingen van dubbellagen. Daarom wordt in **Hoofdstuk 4**, getiteld "Een enkelspleet-microfluidische chip voor elektrische karakterisering van lipid dubbellagen", een microfluidisch chipontwerp ontwikkeld waarmee elektrische karakterisering van de dubbellagen op chip mogelijk is. De chip werkt op basis van een nieuw bidirectioneel vloeistofdiodesysteem dat de vloeistofconditie aan elke zijde van het membraan in balans houdt, terwijl de buffers aan beide zijden gescheiden blijven, wat essentieel is bij elektrische metingen aan de dubbellagen. Een bijkomend voordeel is dat, doordat de oplossingen aan beide zijden van het membraan geïsoleerd blijven, deze chip het mogelijk maakt om lipid membranen te vormen en te karakteriseren onder asymmetrische omstandigheden.

Met het in Hoofdstuk 2 ontwikkelde microfluidische systeem in handen, richt **Hoofdstuk 5** ("Mechanische karakterisering van vrijstaande lipid dubbellagen met temperatuur-gecontroleerde fasen") zich op thermomechanische eigenschappen van membranen met gel-vloeistof co-existentiestructuren. Fasescheiding is bekend als bepalend voor de mechanische eigenschappen van celmembranen en beïnvloedt de functie van eiwitten binnen het membraan en de interactie tussen het membraan

en geneesmiddelen. Ondanks het belang hiervan is er slechts een beperkte hoeveelheid literatuur over de mechanische karakterisering van dergelijke membranen. Deze schaarste is grotendeels toe te schrijven aan de lage stabiliteit van niet-vloeibare lipid dubbellagen, mogelijke artefacten door het experimentele platform die faseverandering/-scheiding belemmeren, en technische problemen met temperatuurregeling en -controle.

De chip ontwikkeld in Hoofdstuk 2 wordt opnieuw gebruikt in **Hoofdstuk 6** ("Effect van lipidenstaart-asymmetrie en cholesterol op de mechanische eigenschappen van lipide dubbellagen") om te onderzoeken hoe asymmetrie in de structuur van lipidenstaarten de bulkmechanische eigenschappen van lipide dubbellagen beïnvloedt. In dit hoofdstuk wordt een breed scala aan membranen in vloeibare, geribbelde en gel-fasen met staart-symmetrische en staart-asymmetrische lipide structuren succesvol op de chip vervaardigd en gekarakteriseerd. Het bijzondere is dat de membranen die hier worden bestudeerd allemaal uit één enkele component bestaan, wat het gemakkelijker maakt om te begrijpen hoe elk specifiek staart-asymmetrisch lipidemolecuul bijdraagt aan de bulkmechanische eigenschappen van het celmembraan, een langbestaande vraag in bacteriële celmembraanonderzoek. Daarnaast wordt aan het einde van dit hoofdstuk

ook onderzocht hoe cholesterol membranen gevormd uit staart-asymmetrische en staart-symmetrische lipiden beïnvloedt.

In **Hoofdstuk 7** ("Effect van azithromycine op de mechanische eigenschappen van POPC membranen") wordt het microfluidische afleverplatform beschreven in Hoofdstuk 3 gebruikt om het effect van een antibioticum, azithromycine, op POPC-dubbellagen te bestuderen als een proof-of-concept voor het ontwikkelde systeem.

Tot slot vat ik in **Hoofdstuk 8** de belangrijkste bevindingen van dit werk samen en doe ik aanbevelingen voor toekomstig onderzoek.

Al met al kan de bijdrage van dit proefschrift aan het vakgebied vanuit twee aspecten worden bekeken: ten eerste bieden de nieuwe microfluidische ontwerpen een basis voor een breed scala aan studies over kunstmatige celmembranen. Ten tweede rapporteert het nieuwe resultaten over de biofysische eigenschappen van vrijstaande lipid dubbellagen. Ik hoop dat dit werk bijdraagt aan een beter begrip van lipid dubbellagen in celbiologie en geneesmiddellevering.

Chapter 1

Introduction

This chapter provides basic information about lipid bilayers, their physical properties, their formation and their characterization in microfluidics systems, as well as a brief introduction to microfluidics-based drug-delivery to cell membranes.

*“If learning is what you would hold most dear,
With wisdom you will stride the turning sphere.”*

Ferdowsi Toosi

1.1 Lipid bilayers at the core of artificial cell membranes

The cell membrane, for both eukaryotic and bacterial cells, functions as a selective barrier separating the cell interior from the outer environment (Figure 1.1 a)¹⁻². Cell membranes are additionally involved in cell communication (via membrane proteins), import/export of molecules, cell growth, and motility (Figure 1.1 b). Cell membranes are mainly composed of lipid bilayers (Figure 1.1 c). The lipid bilayer is fundamentally a pair of zipped lipid monolayers (leaflets) of phospholipid molecules. A phospholipid molecule is an amphiphilic fat molecule comprising a hydrophilic polar phosphate "head" and a hydrophobic nonpolar lipid "tail" (Figure 1.1 d)¹⁻².

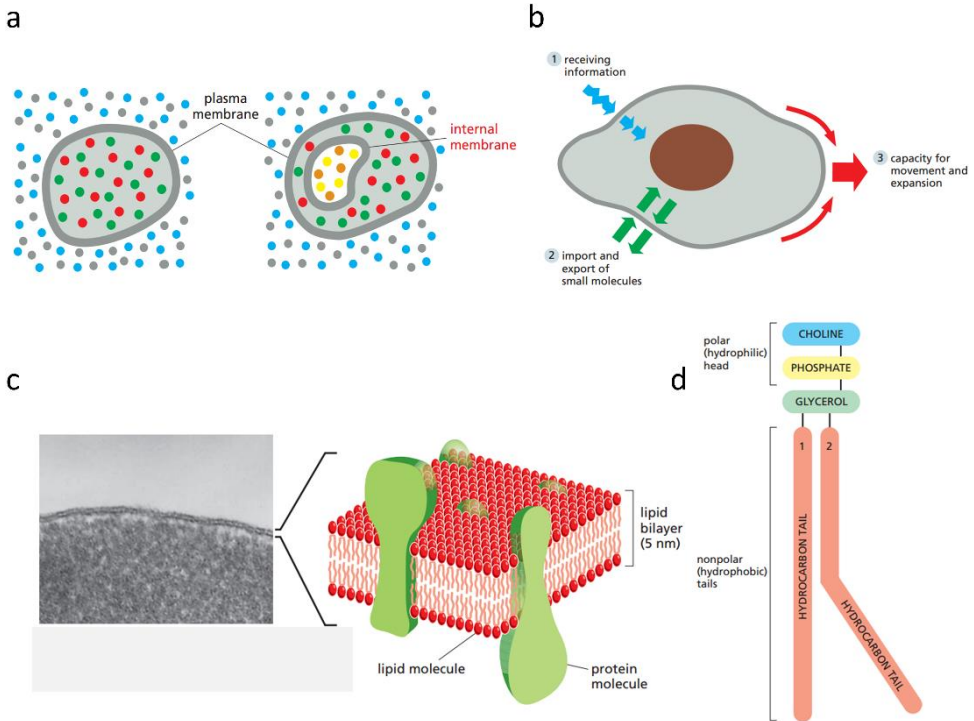


Figure 1.1: Cell (plasma) membrane. (a) Cell membrane as a barrier for both bacterial and eukaryotic cells. (b) Schematic illustrating the role of cell membranes in some biological functions. (c) Human red blood cell. Lipid bilayers are the main structural unit of cell membrane. (d) Schematic of a phospholipid molecule (this image is adapted from ref 2).

The physical properties of the membrane, including its phase behavior ³, mechanical traits ⁴, electrophysiology ⁵, and the membrane's interaction with external stimuli such as drugs or particles ⁶, depends on the arrangement of lipid molecules within each leaflet, the tail/head structure of lipid molecules ⁷, their

interactions with neighbouring molecules ⁸, and the manner in which the leaflets are fused together ⁹⁻¹⁰, along with environmental conditions ¹¹.

In vitro artificial cell membrane systems are central to a wide range of scientific research, including bottom-up artificial cell synthesis ¹² and studies on cell-drug interactions ¹³. The quest for dependable methods to create durable artificial cell membranes has been a focal point of research for some time. Typically, artificial membranes are made either as a supported lipid bilayer (SLB) ¹⁴ or in a freestanding ¹⁵ configuration. The freestanding configuration can appear in 5 different arrangements: (1) a lipid vesicle ¹⁶, (2) droplet interface bilayer (DIB) ¹⁷, (3) pore-suspended lipid bilayer (PsLB) ¹⁸, (4) black lipid membrane (BLM) ¹⁹ which includes also vertical planar freestanding bilayers ²⁰⁻²², and (5) lipid bilayer floating over an SLB ²³. A summary of all freestanding and supported bilayers is shown in

[Figure 1.2](#).

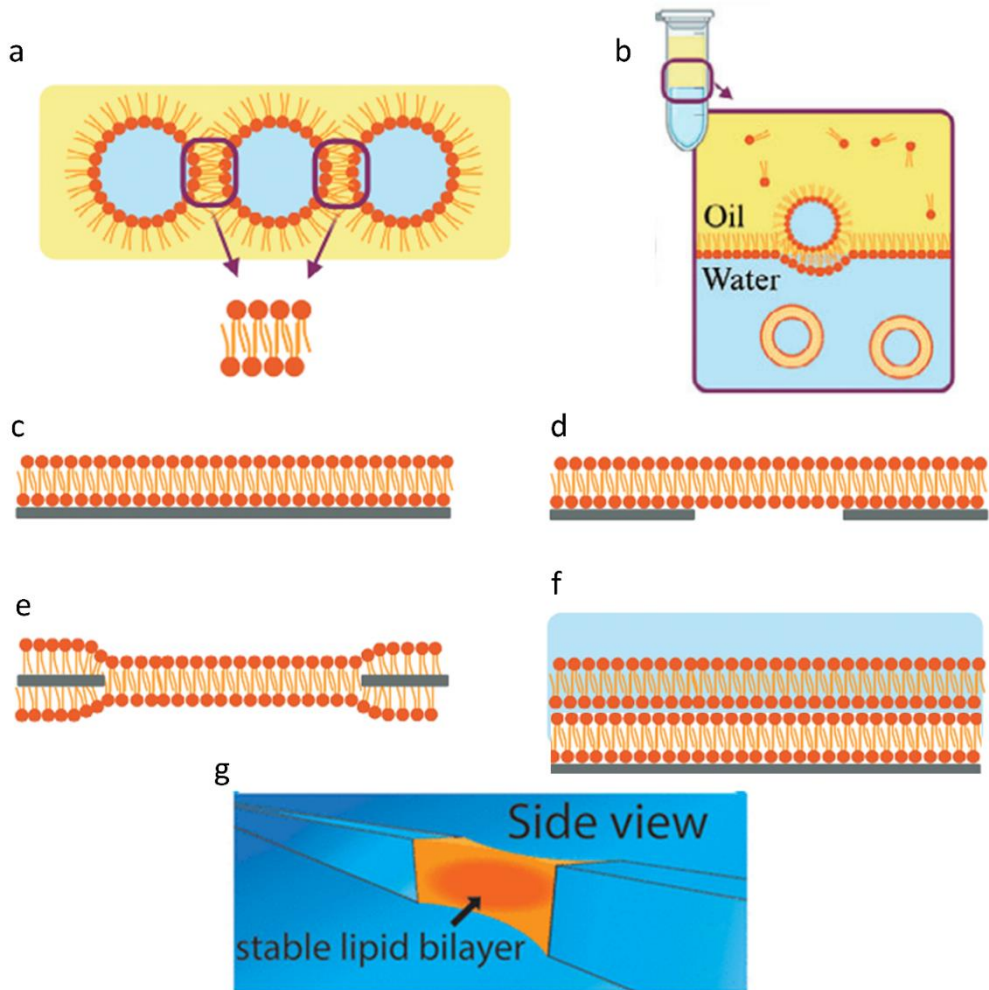


Figure 1.2: Schematic side view of various supported/free-standing membrane arrangements. (a) Droplet interface bilayers, (b) vesicles, (c) supported lipid bilayer, (d) pore-suspended lipid bilayer, (e) black lipid membrane, (f) floating lipid bilayer, (g) vertical planar freestanding bilayer (top view would be similar to figure (e)). Figures 1.2 a to f are taken from ¹³ and Figure 1.2 g is taken from ²².

The unsupported configurations are often preferred over the supported one since the contact between the support and the adjacent leaflet of the membrane affects phase behaviour and other physical properties of the membrane to the extent that the membrane features become heavily dependent on the substrate topography²⁴⁻²⁷. Among the unsupported configurations, the vertical freestanding planar bilayers have the advantages of being compatible with optical tweezers (since they are vertical to the microscope focal plane)²⁰⁻²¹. Additionally, both aqueous media and the leaflet on either side of the membrane are readily accessible and formation of asymmetric bilayers is also possible²⁸. For this reason, throughout this thesis, the vertical freestanding arrangement has been implemented.

1.2 Formation of freestanding planar lipid bilayers in microfluidic platforms

Microfluidics offers a cost-effective, reproducible, and scalable platform for mimicking physiological environments, enabling precise and high-throughput studies of molecular interactions with artificial cell membranes¹³. Formation of planar freestanding bilayers, either in horizontal²⁹⁻³³ or vertical configuration^{6, 20-22, 28, 34}, in microfluidic chips has been gained more popularity recently. The main concept is to zip two lipid monolayers at a gap connecting two microfluidic

channels/chambers, sometimes followed by organic solvent drainage until a minimum amount of the solvent is left ^{21, 30}. [Figure 1.3](#) shows some examples of current microfluidics platforms. [Figure 1.3 a](#) presents the side view of a platform consisting of two microfluidic chambers separated at the gap with hexadecane oil ³³. Lipid vesicles are injected into both chambers and lipid molecules from the vesicles are adsorbed at the hexadecane interface. After two lipid monolayers are formed, the oil in between is drained until the monolayers are zipped and the horizontal freestanding bilayer is formed at the gap. [Fig 1.3 b](#) and [c](#) show microfluidic chips forming vertical bilayers ^{22, 28}. The flow carrying the leaflets (monolayers) is injected into both parallel channels on the chip until the leaflets join at the gap and form the bilayer. These two aforementioned microfluidic chips are based on the concept of forming a single vertical planar freestanding bilayer on a single chip containing only one gap. Higher throughput has been achieved on microfluidic designs based on a similar concept of zipping two monolayers over a gap, but now with an array of gaps to enable several bilayers on a same chip ²⁰⁻²¹. In the present thesis, the concept of arrays of membranes was applied for the development of microchips used for mechanical characterization of bilayers. Only one section (Chapter 4) is based on a chip with a single membrane, which was required for membrane electrophysiological measurements.

Microfluidics platforms based on horizontal configuration ease the imaging of the full membrane as the membrane can be aligned with the focal plane of the microscope³². However, platforms with vertical orientation of the membrane make membrane deformations readily observable²⁸, making them ideal to be combined with optical tweezers for indentation and mechanical characterization²⁰⁻²¹.

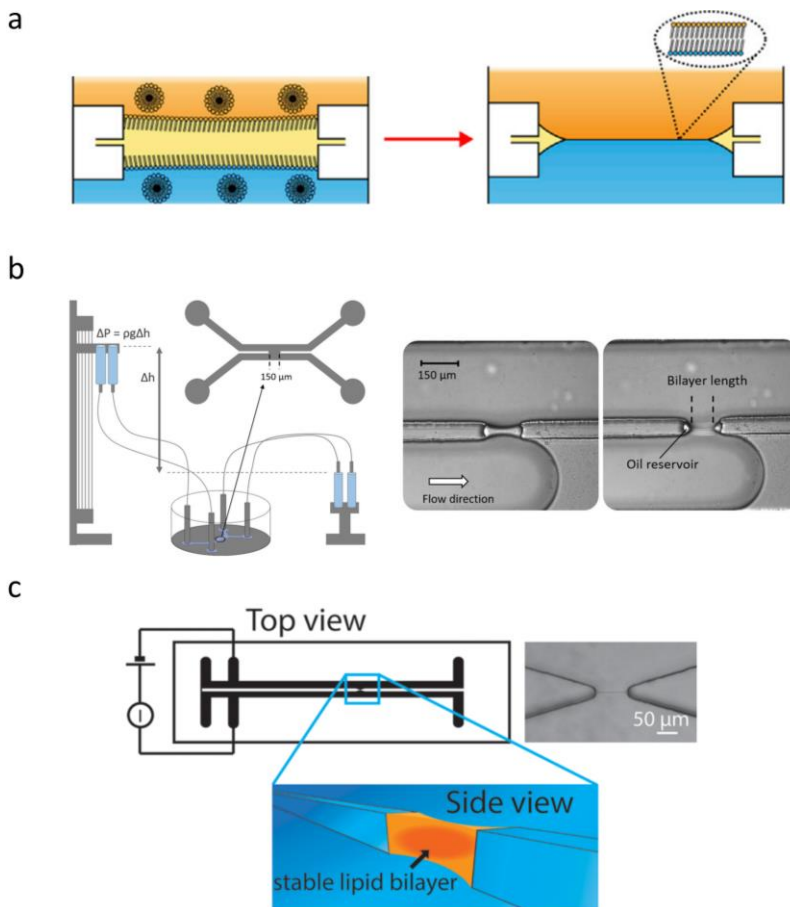


Figure 1.3: Examples of planar freestanding bilayers formed in microfluidic platforms. Bilayers can either be formed in a (a) horizontal (where organic phase (yellow) is separating the vesicle

containing aqueous phases (blue and orange)) or (b, c) vertical orientation. *Figure 1.3 a* is taken from ³³, *Figure 1.3 b* is taken from ²⁸, and *Figure 1.3 c* is taken from ²². The gap size in *Figure 1.3 b* is 300 μm width.

1.3 Characterizing physical properties of lipid membranes

Several biological phenomenon taking place at the cellular level are directly affected by the physical characteristics of the cell membrane. For instance, cell division ³⁵, trafficking ³⁶, motility ³⁷, polarization ³⁸, cell-drug interaction ³⁹, fusion ⁴⁰, and growth ³⁵ are all governed by the physical features of the cell membrane such as membrane elasticity (tension and rigidity), membrane hydrodynamics, and electrophysiology. Interestingly, these physical characteristics of cell membranes are influenced by the environmental conditions of the membrane (like pH ⁴¹, temperature ⁴², or salt concentration ⁴³) and also the presence of specific molecules like drugs ⁴⁴, nanoparticles ⁴⁵, or even microplastics ⁶. Throughout the present thesis, characterizing various lipid bilayers under different circumstances is done via analysing their elasticity (surface tension and bending rigidity), interfacial hydrodynamics (fluid slip), and electrical capacitance, all on-chip.

Analysing the deformation of lipid bilayers, whether induced by external force or occurring naturally due to thermal energy, is a prevalent method for evaluating membrane elasticity. Applying unequal fluidic pressures on membrane leaflets and

recording its deformation is a microfluidic method used to measure membrane tension²⁸. Measuring the fluctuations of freestanding lipid bilayers due to thermal energy is another way of assessing membrane tension and also its bending rigidity⁴⁶. Optical tweezers have also been employed to manipulate membranes directly, not only to extract their elastic properties^{21, 47-51}, but also to investigate membrane hydrodynamics, including interfacial fluid slip and membrane viscosity. This is achieved by shearing the membrane with an optically trapped bead and recording the hydrodynamic response²⁰. The unique advantage of optical tweezers lies in their ability to shear vertical, planar, freestanding lipid bilayers. In contrast, other methods rely on flowing fluid over a supported bilayer at the bottom of a microchannel⁵² or on generating flow around vesicles⁵³ or droplet interface bilayers (DIBs)⁵⁴. The use of a support in shearing experiments on supported membranes can interfere with lipid lateral diffusion, thereby affecting membrane hydrodynamics⁵⁵. Additionally, flow generation around vesicles and DIBs is limited to shearing the outer leaflet, offering no control over the inner leaflet, and does not allow for more complex hydrodynamic measurements, such as interleaflet coupling, which are crucial for accurate membrane viscosity measurements²⁰. As illustrated in [Figure 1.4](#), combining optical tweezers with vertical, planar, freestanding bilayers provides access to both leaflets, allows for direct indentation

of the bilayer, and enables the measurement of its elastic properties (such as tension and rigidity) and hydrodynamic properties (including interfacial fluid slip, interleaflet shear dissipation, and membrane viscosity).

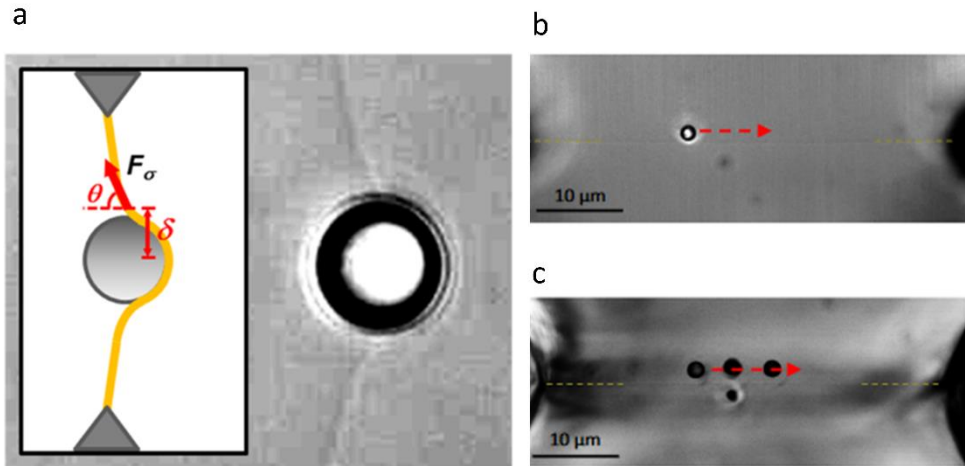


Figure 1.4: Examples of interfacing optical tweezers with vertical, planar, freestanding lipid bilayers inside microchannels (all top view). (a) An optically trapped bead is pushed against a membrane to deform it. By analyzing the applied force and resulting deformation of the membrane, elastic properties of the membrane can be figured out. (b) Shearing the membrane with the trapped bead for analyzing its interfacial fluid slip. (c) Shearing the membrane on one side while sensing its effect on the other side to characterize interleaflet coupling and the membrane viscosity. Figure 1.5 a is taken from ²¹, figures. 1.5 b and c are taken from ²⁰.

1.4 Delivery of particles/drugs to lipid bilayers using microfluidics

The majority of therapeutic molecules either target the cell membrane directly or must traverse it to access the encapsulated contents of the cell. Clearly, the cell

membrane, as a selective barrier, is a key player defining drug efficiency or its toxicity⁵⁶⁻⁵⁷. Although the pharmaceutical industry aims to standardize the profiling of drug candidates to facilitate quicker and more efficient drug screening at the early stages of drug discovery, research on drug-membrane interactions using microfluidic systems remains inconclusive. This is especially true for high-throughput approaches, which require arrays of stable lipid bilayers¹³. Delivery of drugs to freestanding membranes requires the reversible replacement of the aqueous media around the formed membranes, which is challenging due to the flaccid nature of membranes⁵⁸⁻⁵⁹. Even the slightest unfavorable hydrodynamic flow during the delivery stage can warp or completely destroy the bilayers on the chip⁵⁸. For this reason, drug delivery and screening is mostly performed on cell-based microfluidic systems, where the drug is delivered to trapped bacteria⁶⁰ or cellular tissues⁶¹, biofilms (Figure 1.5)⁶², or formed cell monolayers⁶³ in microchannels. Cell-based platforms, while widely used and stable, lack the ability to perform controlled biophysical studies or extract molecular-level information that is critical for ADMET (absorption, distribution, metabolism, excretion, and toxicity) profiling and molecular optimization^{13,64-65}. Consequently, there is a strong demand for more targeted platforms, such as chips specifically designed to study drug-membrane interactions, although such platforms are currently underrepresented in the

literature¹³. A part of the effort in this thesis is to address this lack of robust bilayer-based drug-screening platforms.

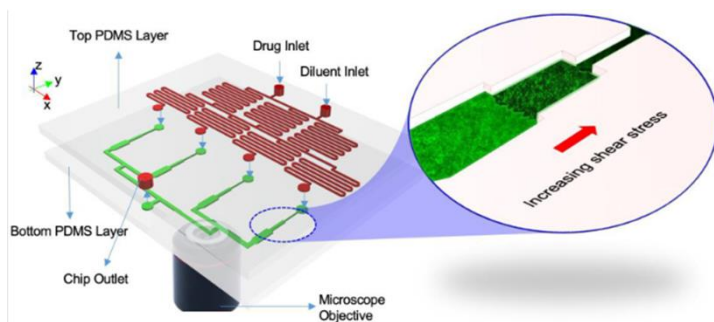


Figure 1.5: An example of a microfluidic chip for drug delivery to bacterial biofilms grown inside microchannels. The system involves the integration of a microfluidic diluter, allowing the biofilm to be treated simultaneously with four different diluted concentrations of a drug. Unlike a freestanding membrane within a microchannel, a biofilm that coats and adheres to the channel walls is less susceptible to unfavorable fluidic conditions that may arise during the drug delivery phase (the image is taken from⁶²).

1.5 Challenges and Research Aim

High-throughput and robust formation of artificial cell membranes is highly demanded in both research and industry. However, the current platforms are either low-throughput or limited in terms of lipid compositions and compatibility with various biophysical tests. A new generation of microfluidic systems are required to

enable the formation of various types of lipid bilayers and to perform diverse biophysical tests on them.

The overall aims of this thesis are firstly to develop microfluidic platforms that pave the way toward better on-chip artificial cell membrane formation, and secondly, to perform biophysical measurements on the membranes formed on the developed chips. “**How to fabricate robust artificial cell membranes on microfluidic chips?**”, “**How do temperature, cholesterol content, and lipid tail asymmetry affect the mechanical properties of freestanding planar bilayers?**”, and “**How to develop an on-chip lipid bilayer-based drug-screening platform?**” are the three major questions addressed in this thesis.

1.6 Thesis Outline

This thesis entitled “**Microfluidics for Biophysical Studies on Artificial Lipid Membranes**” is organized in two parts: PART I (chapters 2, 3, and 4) relates to the development of new microfluidic tools, and PART II (chapters 5, 6, and 7) relates to the use of these newly designed tools in biophysical studies of lipid bilayers.

Part I starts with **Chapter 2**, where a key question is addressed: How to form stable lipid bilayers in microfluidic chips? To do so, a high-throughput pillar-based microfluidic platform integrated with a novel bubble-trap system and a thermocouple for precise temperature control is developed. This integrated chip

allows for the formation of arrays of freestanding planar flat lipid bilayers that can be interfaced with optical tweezers (OTs). The microfluidic bubble trapping and microfluidic formation of lipid bilayers discussed in this chapter are the technical core of the present thesis. All the steps for design, fabrication, implementation, and OT characterization of the novel passive bubble trap are presented in this chapter.

In **Chapter 3**, the integrated chip developed in **Chapter 2** is further developed to address a long-standing microfluidic challenge: reversible buffer change around lipid bilayers on chip. Through this development, it is possible to transform the initial design into a drug-screening chip. The function of the chip is quantified from a mechanical point of view with laser-induced fluorescent microscopy (LIF) and particle image velocimetry (PIV).

In **Chapter 4**, we aim to develop a microfluidic chip enabling us to do electrophysiological tests on-chip. Integrating a novel bidirectional fluidic-diodes to the single-gap microchips, we develop a novel platform that enhance the success rate of the conventional single-membrane on a single chip concept. The microfluidic platform developed in this chapter delicately balances the pressure on each leaflet, leading to the formation of flat, planar freestanding bilayers. Unlike the chips introduced in **Chapter 2** and **Chapter 3**, pressure balancing is not achieved *via* direct contact/mixing of the buffers surrounding each leaflet, but

instead *via* fluidic diodes. This means that the buffer around each leaflet is isolated from the buffer on the other side of the membrane, paving the way for more complex experiments like electrical measurements on bilayers, forming lipid bilayers under asymmetric conditions, and studying transmembrane transport phenomena.

Then, the thesis continues with **Part II**, which describes how the newly developed microfluidic technologies are used for biophysical characterization of lipid bilayers. In **Chapter 5**, the thermal microchip developed in **Chapter 2** is used for robust and high-throughput formation of lipid bilayers below their phase transition temperature with the possibility of adjusting the temperature to induce thermal-induced phase separation. The known challenge of forming stable non-fluid bilayers is therefore attempted on this chip. Membranes of either DOPC:DPPE (3:2) or PMPC are formed and their thermomechanical properties are investigated by assessing the effect of temperature on the elasticity (tension and bending rigidity) and hydrodynamics (interfacial fluid slip) of these bilayers. Both lipid compositions possess a similar melting point (27 °C) and form gel-fluid membranes at room temperature. However, their structures are intrinsically different. The DOPC:DPPE lipid mixture forms gel-fluid domains while PMPC lipids adopt a ripple structure below the melting point.

In **Chapter 6**, we use the same microchip to now investigate the mechanical properties of a group of less studied lipids, namely tail-asymmetric lipids. The effect of tail-asymmetry on the elasticity and hydrodynamics of both saturated and unsaturated lipid bilayers is studied with optical tweezers. The main challenge of this chapter is the formation of single component bilayers in phases other than fluid, i.e., gel and ripple. Thanks to the robust microfluidic system, this challenge is successfully tackled. At the end of this chapter, we also investigate the effect of lipid tail-asymmetry in combination with cholesterol on the mechanical properties of freestanding lipid bilayers.

In **Chapter 7**, utilizing the developed delivery chip of **Chapter 3**, the effect of Azythromycin at two different doses, 5 μM and 250 μM , is studied on 1-palmitoyl-2-oleoyl-sn-glycero-3-phosphocholine (POPC) bilayers on the chip. We show how membrane tension in POPC bilayers is reduced in the presence of the drug in a dose-dependent manner.

Finally, in **Chapter 8**, conclusions of the thesis is presented. Also, the outlook and possible future directions are discussed. This chapter aims to provide insights to researchers who are willing to continue on the concept of the present thesis.

Section 1

Chapter 2

Combination of optical tweezers with lipid bilayers formed on an integrated microfluidic platform

Abstract:

The majority of the experiments conducted throughout this thesis are based on forming lipid bilayers within micropillar based microfluidic platforms and interfacing them with optical tweezers for physical characterization. In this chapter, an introduction to optical tweezers is first presented. Then, a novel high-throughput integrated microfluidic platform for the formation of lipid bilayers is described. Specifically, two components of the microfluidic platforms used in the present thesis are explained and characterized, i.e., the micropillars chamber and the bubble trap, which are both essential for lipid bilayer formation.

Part of this chapter contains published material from: Yahyazadeh Shourabi, Arash, et al. "Mechanical characterization of freestanding lipid bilayers with temperature-controlled phase." *Soft Matter* 20.42 (2024): 8524-8537.

2.1 Introduction to optical tweezers

Since their inception, optical tweezers have become increasingly used in investigation of nonlinear optics⁶⁶, soft matter physics⁶⁷, molecular biology⁶⁸, and analytical chemistry⁶⁹, and for micro/nano manipulation⁷⁰⁻⁷¹. Optical tweezers utilize a highly focused laser beam to apply optical forces on micro- and nanoscale objects, driven by the principle of linear momentum conservation during light-matter interactions. When the experimental conditions are appropriately set—such as the laser power, particle size, and the refractive indices of both the surrounding medium and the particle—these forces can trap and confine a particle near the focal point of the laser beam⁷¹⁻⁷².

Figure 2.1 depicts the basics of an optical tweezers setup and also the principles of trapping a bead with the optical tweezer. In Figure 2.1 A, the main components of a typical setup are schematically illustrated. A laser beam generated by a laser source is expanded using two lenses. The expanded beam is then directed by a dichroic mirror to fill the back aperture of a high numerical aperture (NA) objective. The optical trap is formed at the focal point of the beam. A dielectric particle positioned near the focal point experiences a force resulting from the transfer of momentum caused by the scattering of incoming photons. This optical force is typically divided into two components: (1) the scattering force, which acts along the direction of the light's propagation, and (2) the gradient force, which acts in the direction of the light's spatial intensity gradient⁷³. The interferogram

produced by the interaction between the light scattered by the particle is gathered by the condenser lens. This interferogram, which contains details about the particle's position, is then reflected by a dichroic mirror onto a position sensitive device (PSD). The voltage signal generated by the PSD is then filtered and transmitted into a computer (PC). These signals carrying information on the position of the bead at each moment can be analyzed to find the trap stiffness. While this setup typically uses the same laser for both trapping and detection, a separate laser can also be employed for detection. Using a separate detection laser improves sensitivity and accuracy in position detection as it helps with calibration.

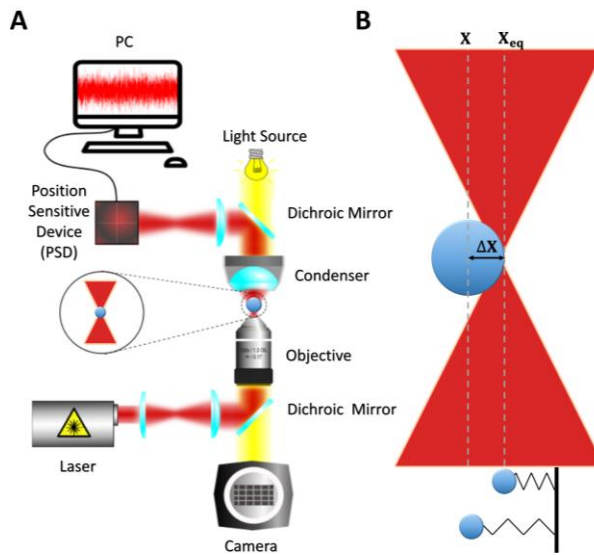


Figure 2.1: Principles of optical trapping. A) Basic parts of an optical tweezer setup. B) Schematics of a bead trapped by an optical tweezer. For small displacements (ΔX), the trap

behaves like a Hookean spring. The image in panel A is a modified version of the original version in ⁷¹.

To achieve stable trapping in all three dimensions, the axial gradient force that pulls the particle toward the focal point must surpass the scattering force that tends to push the particle away from this region. This requires creating a steep light intensity gradient by tightly focusing the trapping laser beam to a diffraction-limited spot using a high numerical aperture objective. The balance between these two forces, the gradient force and the scattering force, causes the particle's axial equilibrium position to be slightly downstream from the focal point. For small displacements (typically around 150 nm or less), the gradient force behaves like a Hookean spring (Figure 2.1 B, $F_{trap} = k_{trap}(X - X_{eq})$), with the restoring force proportional to the particle's displacement from its equilibrium. Subsequently, the stiffness of the optical trap is directly related to the intensity of the laser light.

To calculate the trap stiffness (k_{trap}), i.e., the stiffness of the equivalent Hookean spring, various methods have been proposed in the literature depending on the nature of the experiment, including the drag force method ⁷⁴, the power spectrum density method ⁷⁵, and the equipartition method ⁷⁶. Throughout this thesis, the equipartition method has been implemented for the calibration of the optical trap.

According to the equipartition theorem, in a system at thermal equilibrium, the total energy is evenly distributed among all available forms or modes. Therefore, each degree of freedom associated with the system's kinetic energy contributes equally to the total energy. Dielectric beads within optical tweezers interact with water molecules, each carrying an energy of $1/2 k_B T$; where k_B is the Boltzmann constant and T is the temperature. Assuming a harmonic optical trap this relationship leads to the following equation ⁷⁷⁻⁷⁸:

$$\frac{1}{2} k_B T = \frac{1}{2} k_{trap} \langle x_{bead}^2 \rangle \quad (1)$$

Here, $\langle x_{bead}^2 \rangle$ is the experimentally measured variance of the trapped bead's displacement from its equilibrium position.

2.2 High-throughput formation of freestanding planar membranes

In this thesis, freestanding lipid bilayers are formed in microfluidic devices by the contact of two lipid monolayers based on reported methods ^{21, 79} that are here modified for increased lipid membrane formation and stability (Figure 2.2). The core of the improvement revolves around tackling three primary challenges that existed in previous systems.

The first challenge is to deal with unwanted bubbles in the channels often formed at the interface between the aqueous and organic phases, disrupting the contact process

between monolayers. Air bubbles are a common hurdle in microfluidics⁸⁰, in particular for experiments conducted at varying temperatures⁸¹. The bubbles have several possible origins: air trapping due to the geometry and various components of the system (tubing, connection, inlet, microchannels), wettability properties of the chip material, temperature variations, and injecting both an organic and an inorganic solution into the chip⁸². To capture and/or remove air bubbles from microfluidic systems, bubble traps are often used. They are categorized as passive or active traps with regards to their function⁸⁰, and as in-plane or out-of-plane with regards to their configuration^{63, 81}. Here, a novel passive bubble trap with an in-plane configuration is designed with an asymmetric architecture (discussed more in details later on).

The second challenge is the frequent low success rate of membrane formation in microchips, specifically with cholesterol-free non-fluid lipid compositions or non-conical lipids^{29, 83}. To tackle this issue, a chamber filled with several micropillars was designed downstream of the bubble trap. This results in a high-throughput membrane formation, with several stable membranes forming per microchannel at a time. Using multiple membranes on a single chip allows various experiments on different membranes without the time-consuming process of forming new membranes for each new experiment^{21, 79}. Having several membranes on the chip is a key point here, since designs with a single membrane per microchannel have reproducibility and throughput issues, making them unsuitable for mechanical characterization when a large number of experiments with

different lipid compositions are usually required. However, we should mention that single-membrane designs are still necessary for electrical measurements^{22,34} (See chapter 4 of the present thesis), for asymmetric membrane formation²⁹, and for membrane protein channels studies⁸⁴.

Finally, the third challenge is to ensure that the pressure and the flow velocity on each side of the bilayer are comparable, during and after membrane formation. This is a requirement for smooth leaflets zipping, and it ensures the flatness and improves the membrane long-term stability under ongoing fluid flow. To do so, we designed the pillar chamber with an architecture that follows the fluid-flow pattern (contracting – expanding width of walls in the chamber, see [Figure 2.2 B](#)), making the flow at the gaps fully symmetric (i.e., balanced fluidic pressure at the gap), thus ideal for membrane formation.

2.2.1 Microfluidic system description

Considering the abovementioned challenges (i.e. bubbles removal, high-throughput membrane production, stability, fluidic symmetry, and flatness), we introduce a design that facilitates freestanding membrane formation for thermal and mechanical tests. For this, a microfluidic system integrated with a thermocouple is fabricated ([Supplementary Figure S2.1 A](#)). It includes two sections ([Figure 2.2 A](#)): (1) a passive trap for capturing bubbles upstream, (2) a chamber made of an array of micropillars, where membranes can be formed in the gaps between the micropillars. For the system, we use 30 gaps (two rows each containing 16 gaps) constructed by 32 micropillars (two rows of micropillars with 16

micropillars in each row) to increase the system's throughput, resulting in the formation of several stable flat membranes for each infusion. The material NOA81 (Norland Optical Adhesive 81) is selected for the fabrication of the chip (including the micropillars and the bubble trap) sandwiched between a glass slide and a cover slip ([Supplementary Figure S2.1 B](#)). NOA is a UV-curing adhesive composed of thiol-ene resin with hydroxyl function on the surface⁸⁵. Channels made of NOA have shown lipophilic and slight hydrophilic surface characteristics (water contact angle of $69.3^\circ \pm 1.3^\circ$)^{22, 86}. Most importantly, NOA81 was shown to produce membranes with reduced annulus size (which is essential for interfacing the bilayers with optical tweezers) when chloroform is used as organic solvent compared to the cases where organic solvent is not pure chloroform^{21, 79}. To elevate the temperature of the membrane within the microchannel, we placed the membrane-containing chip onto an optical tweezer setup featuring a coiled objective ([Supplementary Figure S2.1 B](#)). A 3D COMSOL simulation is performed to model the temperature within the flow cell ([Supplementary Figure S2.2](#)), showing that a homogeneous temperature distribution is expected in the channel with less than 1°C of temperature gradient across the height of the channel.

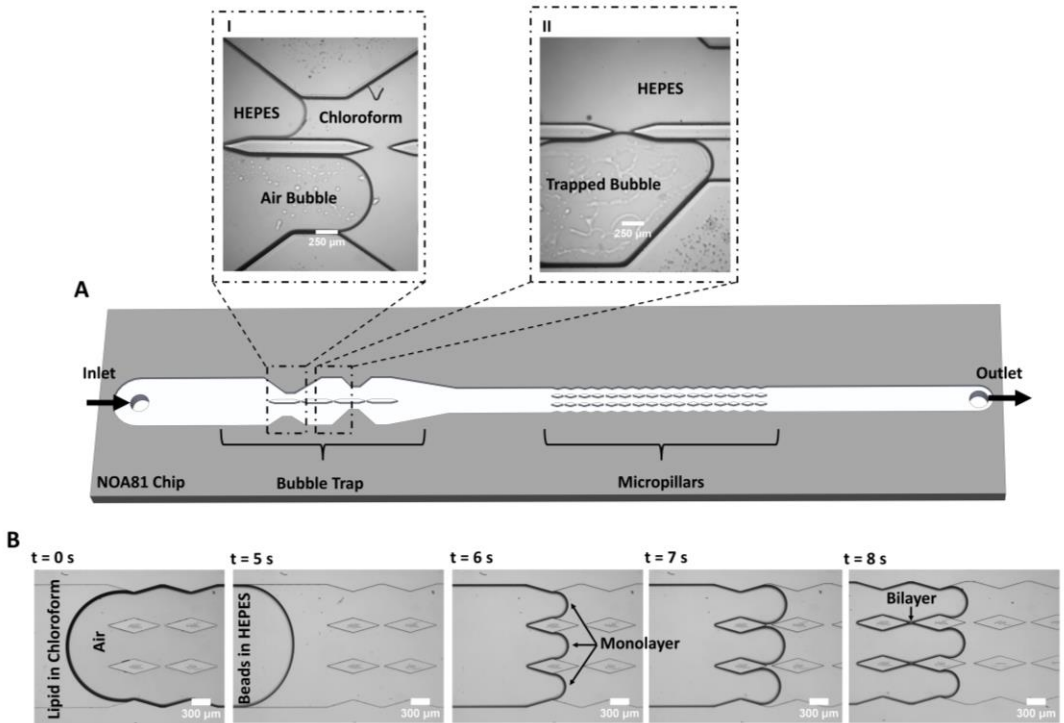


Figure 2.2 Microchip structure and procedure for membrane formation. A) Design of microchip. The NOA81 chip consists of two major sections: a bubble trap (with an asymmetric structure and barriers on the center line) and a micropillars section, including 30 gaps and 32 micropillars. The three-phase flow – air, chloroform with lipids, aqueous HEPES buffer with microbeads- is introduced at the inlet port and reaches the bubble trap, which divides the main channel into two channels of unequal widths (I). The organic phase wets well the channels, and fills and passes the bubble trap immediately, while the bubble(s) get trapped in the wider side of the trap (II). B) Time sequence of membrane formation in the micropillars chamber. The bubble-free HEPES solution ultimately escapes the trap and enables a clean, bubble-free lipid monolayer interface with the

organic phase. Due to the streamline-shaped wall design and being bubble-free, the pressure at each gap is balanced, and lipid monolayers are zipped together to form the flat, planar bilayers.

To form membranes, a solution of lipids dissolved in chloroform is flown into the chip followed by the aqueous buffer HEPES. During this process, air bubbles are often observed at the organic/aqueous interface or in the chloroform. If air bubbles are not captured and reach the micropillars, they affect the flow and prevent membrane formation. The bubble trap is divided into two channels of unequal widths, enabling the trapping of air bubbles in the upstream section of the chip (Figure 2.2). Due to the strong wettability of NOA81 for chloroform, the chloroform solution flows into both channels almost simultaneously (Figure 2.2 A, panel I). Subsequently, we observe that any air bubble present in the system will enter one of the channels, preferably the wider one (Figure 2.2 A, panel I). Bubbles are trapped and slowed down at the constricted sections of the channel (Figure 2.2 A, panel II), enabling the aqueous phase to freely flow in the other channel and resulting in a continuous bubble-free buffer-chloroform interface in the micropillars section (Figure 2.2 B). Lipid bilayers can then be formed by the junction of two monolayer leaflets that 'zip' together after each pillar (Figure 2.2 B).

To demonstrate the added value of using the bubble trap, we compared DOPC:DPPC (3:2) lipid bilayers formed either with the bubble trap or without (by infusing from the outlet).

With the use of the bubble trap, a continuous leaflet-leaflet zipping allows the formation of several stable, flat membranes on the chip (statistics are discussed in Chapter 3). Without the bubble trap, due to the highly asymmetric flow at the gap and the fluidic disturbances generated by the bubbles, the membranes are either not forming, are very short lived, or are highly curved. The bubble trap design substantially enhances the formation of stable flat membranes even at flowrates as high as $5 \mu\text{l}/\text{min}$ (at the inlet). In general, we find that membranes composed of phosphatidylcholines (PC) lipid compositions that are in liquid phase at room temperature (*e.g.*, 16:0 18:1 PC, 18:1 18:1 PC, 18:0 18:1 PC, and 16:0 18:2 PC) remain stable for weeks in our chip if all ports are sealed with silicon grease.

2.2.2 Quantifying the effect of the bubble trap

To quantify the effect of the bubble trap on the pressure balance on each side of the lipid bilayers, the velocity of the flow around the gaps between the micropillars is analyzed in a chip without lipids. When the pressure is not balanced on either side of the gap, a flow can pass through the gap which would prevent membrane formation or lead to the formation of curvy membranes in less extreme cases. With a balanced pressure, the flow on the midline of the gap (inset of [Figure 2.3 A](#)) is expected to be parallel to the channel orientation, with no significant flow passing through the gap, facilitating membrane formation.

To measure the local flow velocities in the gap, a polystyrene bead of $2\ \mu\text{m}$ diameter is optically trapped at the center of the gap's midline as indicated in the inset of [Figure 2.3 A](#), while liquid is flown through the chip from the outlet (for the case with no bubble trap) and from the inlet (for the case with the bubble trap). For this purpose, a similar procedure as for lipid bilayer formation is followed, except that no lipid is added to the organic solvent. Then, while a flow of $2\ \mu\text{l}/\text{min}$ is applied with the syringe pump, the displacement of the beads from the center of the optical trap is measured for a 6-second period and converted to flow velocity for both cases ($N = 3$ experiments for each case). [Figure 2.3](#) reports the velocity components of the flow at the gap for both cases. Without the bubble trap, the velocity along the y -axis (v_y) reaches $1216 \pm 153\ \mu\text{m}/\text{s}$, which indicates that fluid flows across the gap because of a pressure imbalance between the two channels caused by the presence of bubbles in the system. With the bubble trap however, bubbles are trapped upstream in the system ([Figure 2.3 B](#)) and no bubble can reach the micropillars section to disturb the flow pattern. We find a significantly lower v_y of $16 \pm 9\ \mu\text{m}/\text{s}$ in the case of using a bubble trap, which demonstrates that the pressure in both channels is almost equal. This pressure balance shows the benefits of using the bubble trap for membrane formation.

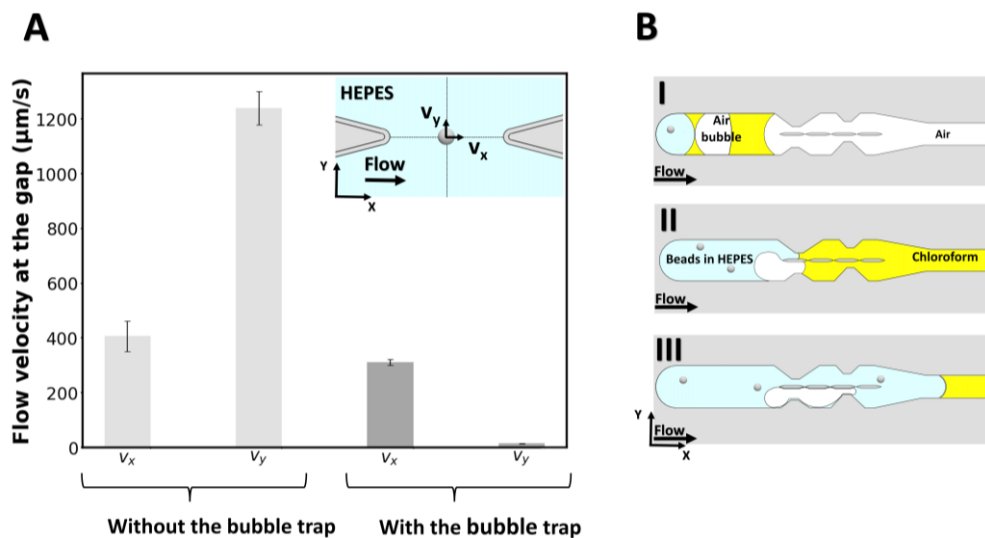


Figure 2.3 Characterizing the effect of the bubble trap. A) The velocity of the fluid is measured at the gap with an optical tweezer, with or without the use of a bubble trap. The velocity v_x corresponds to the fluid moving in a direction parallel to the flow infused in the device. The velocity v_y corresponds to the fluid moving across the gap, in a direction perpendicular to v_x . The inset represents the schematic of the experiment, where a bead is optically trapped at the centre of the gap's midline and the flow is infused into the channel. B) Step by step schematic of the bubble trapping function.

We can directly estimate the pressure difference in the two channels from a hydraulic circuit analysis. From the geometry of our channel, we find a value for the hydraulic resistance of each channel section on the order of $R_h \approx 1.6 \times 10^{10} \text{ kg m}^{-4} \text{ s}^{-1}$. We can estimate the volumetric flow rate from the velocity measurement, which yields an

estimate for the pressure difference between the channels of $\Delta P \approx 10^{-3} Pa$ for $v_y = 16 \mu m s^{-1}$ (with bubble trap) and on the order of $\Delta P \approx 10^{-1} Pa$ for $v_y = 1216 \mu m s^{-1}$ (without bubble trap).

These estimates of the pressure difference in the channels can be directly related to the curvature of the membrane that will form in the gap. Given the membrane tensions previously measured in similar freestanding membranes (ranging between $\sigma = 3 - 6 \times 10^{-6} N \cdot m^{-1}$)²¹, we can estimate the radius of curvature of a membrane formed in the device with bubble trap to be on the order of $\sim 1 mm$, which can be approximated as a flat membrane given the size of the gap. For the device without bubble trap, the radius of curvature of the membrane formed would be $\sim 10 \mu m$, which is smaller than the gap size and we therefore do not expect a membrane to form.

2.3 Conclusion

In this chapter, an opto-microfluidic setup is introduced, consisting of a high-throughput microfluidic system integrated with a bubble trap and a thermocouple. This setup is compatible with optical tweezers and enables the formation and indentation of lipid bilayers at various temperatures (room temperature up to 32 degrees Celsius). As this chapter forms the foundation for the designs used in subsequent chapters, detailed descriptions and quantifications of the chip design parameters are provided. The concepts presented here can be broadly applied to the design of various microfluidic chips for diverse applications.

2.4 Methods and Experimental

2.4.1 Microfabrication

We fabricated NOA81 microfluidic chips integrated with thermocouples for our experiments. The fabrication of the NOA81 chip requires the preparation of a master and a minor mold which are described in this section. This is because casting NOA81 directly on the conventional SU-8 master molds would not allow for easy demolding due to the high stiffness of both the silicon wafer and the NOA81 cured polymer. We therefore used an intermediate minor mold made of PDMS.

2.4.2 Fabrication of the molds

We implemented conventional lithography by etching SU-8 on top of a silicon wafer (Siegert CZ Si, N-type (Phosphorous), 4", 525um thick, 100 oriented, 1- 10Ωcm) to make the master mold (MicroFabspace, IBEC, Spain). The height of the rectangular channels throughout the mold was $115.6 \pm 1.9 \mu\text{m}$. To make the minor PDMS mold, the following steps were followed: PDMS and its curing agent (SYLGARD 184®) with 10:1 ratio were well mixed, degassed in vacuum, and then casted on the master mold and degassed again. Afterwards the mixture was cured in an oven at 85°C during 8 hours. Finally we diced out the PDMS from the master mold and performed surface silanization (tri-chloro (1H,1H,2H,2H-perfluorooctyl)silane (PFOTS, Sigma-Aldrich)) in a desiccator under vacuum. For the silanization, we connected 50 μl of the silane in a glass tube to the vacuumed chamber with a well-sealed connector for at least 2 hours such that the silane is vaporized and treats the surface of the mold.

2.4.3 Device fabrication protocol

The flow cells were fabricated by casting NOA81 (Norland Products) on the PDMS mold and placing the tip of the custom-made k-type thermocouple from Alumel and Chromel wires (TFAL-003 and

TFCY-003, Omega) inside the liquid NOA. Then, a clean glass slide (Corning Micro Slides, thickness: 0.96 to 1.06 mm) was deposited on top of the liquid NOA. The flow cell was then exposed to UV (Promed UVL-36 with four UV-9W-L bulbs) for 5 minutes. Afterwards, the PDMS minor mold was removed, inlet/outlet ports were drilled, and the channels were closed by bonding a cover slip (Deckgläser, thickness: $170 \pm 5 \mu\text{m}$) previously spin-coated with NOA81 (partially UV-cured for 60 seconds). Finally, a 10-minute UV exposition is applied and the chip was then baked for 8 hours on an 85 °C hot plate.

2.4.4 Heating and temperature control

To precisely control the temperature of the chip, a proportional integral derivative (PID) heating system was installed on the objective. Two k-type thermocouples were used to monitor the temperature inside the chip at the edge of the objective. During the experiment, the top layer of the chip was in contact with the condenser. The room temperature was maintained at 21 °C. The chip was mounted on the optical tweezers setup. Then, the objective wrapped in wire elements was heated by applying voltage (Figure S2.1).

2.4.5 Optical tweezers experiments

A 1.2 NA water immersion objective (FI Plan Apo VC 60×, Nikon) was used to optically trap a bead inside microchannels mounted on a piezostage (NANO-LPS100, Mad City Labs) with a 1064 nm trapping laser (YLR-10-LP-Y12, IPG Laser) and a 830 nm detection laser (LDT830-30GC, TOPAG). Anti-aliasing filtering and pre-amplification (10 dB) was performed with a KROHN-HITE 3364 on the voltage signals from a position sensitive detector (PSD, DL100-7-PCBA3, First Sensor). For setup calibration, trap stiffness calculation, and bubble trap quantification (flow measurement through

the gap), signals were sampled at 50 kHz with a cut-off frequency of 24.5 kHz. All the signals from the PSD were processed and converted to nm and pN with a custom-made python code.

For the flow measurements to quantify the effect of the bubble trap, a similar process to the membrane formation procedure was followed. A ProSense NE-30 syringe pump was used to infuse the flow into the chip. To do so, a syringe connected to tubing is filled with the buffer and mounted on the syringe pump. Chloroform, free of lipids, was injected into the channels followed by 10 mM 4-(2-hydroxyethyl)-1-piperazineethanesulfonic acid (HEPES), adjusted to pH 7.4 with concentrated KOH, containing 2 μm polystyrene beads (real diameter = 1.93 μm , Polysciences Inc.) and KCl (150 mM) and bovine serum albumin (0.5 mg/ml). After stabilization, the inlet port remained connected to the pumping line and the outlet was not sealed. A 2 μm bead was trapped at the centre of a gap while the pump was pushing at 2 $\mu\text{l}/\text{min}$ and the signal was measured during 6 seconds.

2.4.6 COMSOL Simulation

The COMSOL Multiphysics 6.2 simulation was conducted using a 3D stationary heat transfer in solid model. The objective, microfluidic chip and condenser were reproduced using built-in thermal properties of the COMSOL library: aluminium for the objective and condenser core (density: 2700 kg/m^3 , thermal conductivity: 238 $\text{W}/(\text{m}\cdot\text{k})$, heat capacity: 900 $\text{J}/(\text{kg}\cdot\text{k})$), silica glass for the lenses and the chip (density: 2203 kg/m^3 , thermal conductivity: 1.38 $\text{W}/(\text{m}\cdot\text{k})$, heat capacity: 703 $\text{J}/(\text{kg}\cdot\text{k})$). The thermal properties of NOA81 were approximated to be the same as those of acrylic plastic (density: 1190 kg/m^3 , thermal conductivity: 0.18 $\text{W}/(\text{m}\cdot\text{k})$, heat capacity: 1470 $\text{J}/(\text{kg}\cdot\text{k})$) and condenser oil as vegetable oil (temperature-dependant physical properties were

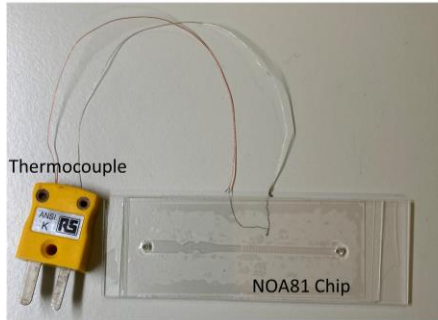
directly used from the COMSOL library). All surfaces not assigned with fixed temperatures as boundaries were assigned as surface-to-ambient radiation boundary conditions.

2.4.7 Statistical

Results shown on [Figure 2.4](#) were obtained from experiments repeated 3 times for each condition. For each experiment, a new bead was trapped. A Kruskal-Wallis one-way statistical analysis was executed, utilizing a significance criterion of $p = 0.05$ to ascertain significance. P-values on the graphs are represented via * for $p < 0.05$, ** for $p < 0.01$ and *** for $p < 0.001$. Error bars in all figures represent the standard deviation of the data. In the box plots in all figures, the box shows the quartiles, the horizontal line is the median, and the whiskers are extending to the most extreme data points.

2.5 Supplementary Information

A



B

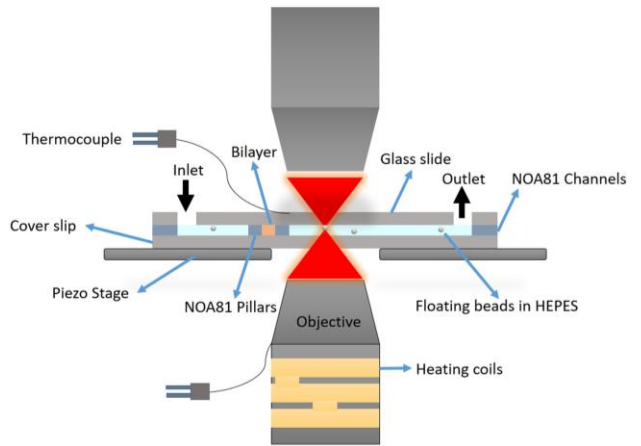


Figure S 2.1: Experimental setup. A) Example of microchip used in this study, with the thermocouple for temperature measurement. B) Schematic side view of the experimental setup. Thermocouples are connected to both the objective and the top layer of the chip for precise temperature measurements. The objective is heated via heating coils.

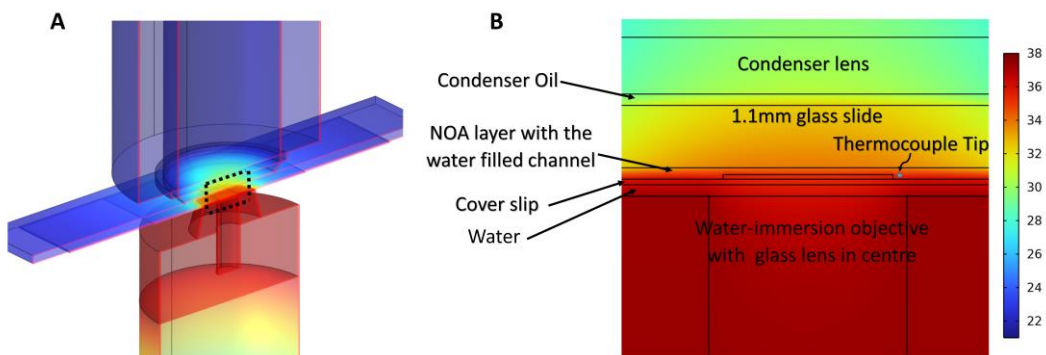


Figure S 2.2: Results of the COMSOL simulation (temperature distribution in the thermal microfluidic setup). A) 3D representation of the COMSOL simulation. B) Middle cut plane view from the 3D COMSOL simulation, represented by the dashed line in panel A. The blue point above the channel is where the tip of the thermocouple is located.

Chapter 3

Microfluidic system for efficient molecular delivery to artificial cell membranes

Abstract:

The cell membrane represents a crucial interface to consider in biomedical research, as a significant proportion of drugs interacts with this barrier. While understanding membrane-drug interactions is important, existing *in vitro* platforms for drug screening predominantly focus on interactions with whole cells or tissues. This preference is partly due to the instability of membrane-based systems and the technical challenges associated with buffer replacement around lipid membranes formed on microfluidic chips. Here, we introduce a novel microfluidic design capable of forming stable freestanding lipid bilayers with efficient replacement of the media in their local environment for molecular delivery to the membrane. With the use of bubble traps and resistance channels, we achieved sufficient hydrodynamic control to maintain membrane stability during the membrane formation and the molecular delivery phases.

Part of this chapter is included in a paper: Yahyazadeh Shourabi, Arash, Martina Iacona, and Marie-Eve Aubin-Tam. "Microfluidic system for efficient molecular delivery to artificial cell membranes." *Lab on a Chip* 25.7 (2025): 1842-1853.

3.1 Introduction

Drug discovery is a time-consuming, complex and expensive process. The drug industry is heavily researching *in vitro* platforms for evaluating the absorption, distribution, metabolism, excretion, and toxicity (ADMET) of therapeutic agents at early stages of the drug development^{56, 87}. A large group of therapeutic agents targets cell membranes or have to infiltrate it to reach the cell content⁸⁸⁻⁸⁹. In either case, the cell membrane is at the frontline, hence the importance of considering the physicochemical and mechanical properties of membranes when evaluating drug-membrane interactions⁹⁰⁻⁹¹. The interaction between drugs and cell membranes can also be viewed from another angle: drug molecules can alter membrane properties (e.g. elasticity⁴⁴, which is linked to vital processes like cell growth and division³⁵). Therefore, an *in vitro* platform for controlled molecular delivery to cell membranes is highly demanded, preferably with high throughput¹³. This would provide insights into how the physicochemical properties of molecules delivered to the membrane (e.g., drug candidates) affect the cell membrane properties^{65, 92-93}.

While drug-membrane interactions are an important aspect to consider in pharmaceutical research, most microfluidic drug-screening systems are cell-based with on-chip drug delivery to bacteria⁹⁴, cellular tissues⁹⁵, cell monolayers⁶³, or biofilms⁶². Cellular models are limited in their ability to facilitate controlled biophysical studies or provide detailed molecular-level information, both of which are crucial for accurate ADMET profiling and

molecular optimization^{13, 64}. The use of on-chip artificial membranes would enable such biophysical studies of pharmaceutical relevance. Artificial membranes are *in vitro* models of biological cell membranes that can be formed in microfluidic chips^{21, 29}, and that are frequently used to study the physical properties of cell membranes⁹⁶. However, due to the challenges of artificial membrane stability and throughput⁹⁷, there is a need for better microfluidics platforms for molecular screening¹³.

The reversible replacement of the media around on-chip artificial membranes is a known experimental challenge^{58-59, 98}, which is specifically due to the low stability of such *in vitro* membranes^{29, 58, 83}. Hence, in such assays, the artificial membranes are typically established initially with the treating agent already present in the buffer to circumvent the need for media exchange²¹. However, this strategy is not ideal as the molecules initially present in the buffer might influence the bilayer formation process, and online monitoring of changes caused by the treating agent is not feasible. Reversible media replacement is not limited to the drug delivery field, but it also applies to studying how buffer changes (e.g. shift in pH)⁵⁹ or molecules/particles delivery (like microplastics⁹⁹) affect artificial membranes.

Various methods have been proposed to treat membranes post their formation via replacing their surrounding media, such as using microinjection for giant vesicles to alter the milieu or to deliver specific molecules to the membrane⁵⁹. However, this approach

lacks high-throughput capabilities and falls short in providing precise control over concentration and reversibility of the treatment⁵⁸. An alternative method involves the use of microfluidics, such as incorporating a diffusion chamber into vesicle-on-chip systems. This approach allows molecules to diffuse and reach the bilayer without the conventional damages that flow causes to membranes, making it a promising tool^{58, 98}. Nonetheless, this approach necessitates the production of vesicles off-chip and is also low-throughput. Previous microfluidic approaches for solution exchange around freestanding lipid bilayers have been reported¹⁰⁰⁻¹⁰¹, but these systems show low throughput or require complex multi-layer chip fabrication. A microfluidic platform acceptable for membrane screening should provide a stable array of such bilayers⁵⁸. Moreover, for numerous measurements including those requiring the accessibility of both sides of the membrane, vesicles may not be suitable, and the use of a planar freestanding configuration becomes essential^{20, 102}. The microfluidic device presented in the current work requires simple chip fabrication methods, without any need for inlet tubing connection/disconnection for solution exchange or off-chip membrane formation, and also it enables rapid buffer replacement (and molecule delivery) through convection to a whole array of several membranes with media on both sides of the planar vertical membrane being exchanged.

In this study, we introduce an easy-to-operate high-throughput microfluidic chip capable of forming an array of stable freestanding planar lipid bilayers and reversibly replacing the aqueous buffer around them for the goal of molecular delivery on artificial membranes.

The chip enables rapid online delivery of molecular agents to the bilayers without imposing significant fluidic tension on them. The chip functions with two separate conventional syringe pumps without the need for any off-chip preparations or any mid-experiment connecting/disconnecting of the tubes. Delivery of the new media to replace the old one is done through convection, making the whole process faster than diffusion-based delivery methods. Thanks to the chip's favourable hydrodynamic design and the fluidic dampers incorporated into it, the membranes remain stable during the molecular delivery process. The chip benefits also from two passive bubble traps enhancing the membrane formation and facilitating the delivery of the substitute media to the bilayers. As a proof of concept, we formed arrays of freestanding planar POPC bilayers on the chip and used optical tweezers to investigate the effect of azithromycin on the elastic properties of the membranes.

3.2 Microfluidic system description

The microfluidic device is made of Norland Optical Adhesive 81 (NOA81)²² with an architecture as shown in [Figure 3.1](#). It comprises dual inlets supplying two parallel channels, each driven by separate syringe pumps. One inlet is for the “membrane channel”, and the other one is for the “replacement channel”. These two parallel channels are connected together via two resistance channels. There are two additional resistance channels on the other side of the membrane channel to keep flow symmetry, which is necessary for the formation of planar bilayers^{28, 102}. With

this design, the flow in the membrane channel experiences the same pressure condition on both sides via symmetric resistance channels both connected to atmospheric pressure. From one side, the resistance channels are connected to exit 1 and exit 2 which are at atmospheric pressure. From the other side, the resistance channels are connected to the yet empty replacement channel, itself connected to atmospheric pressure via its outlet. The chip contains four total outlet ports. Outlets 1 and 2 serve as the egress points for the membrane channel and replacement channel respectively. Exits 1 and 2 allow for balancing the flow during the membrane formation process and for better flow control during the replacement process. More details on the channels and their dimensions can be found in the supplementary information ([Supplementary Figure 3.1](#) and [Supplementary Table S 3.1](#)).

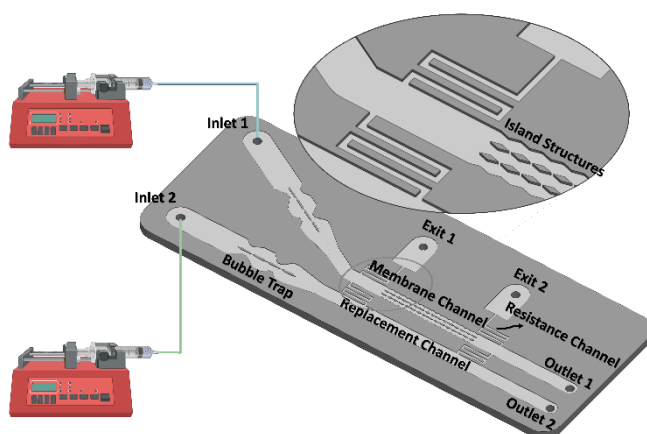


Figure 3.1: Graphical description of the microfluidic design and its main components: the bubble trap, the membrane channel, the replacement channel, and the resistance channels.

The working principle of the chip is illustrated schematically in Figure 3.2. The formation of artificial cell membranes around micropillars was already described in chapter 2 ¹⁰², and is based on flowing lipids dissolved in chloroform into the chip from inlet 1 followed by an aqueous media, called here the Aqueous Phase I (Figure 3.2 A). From inlet 2, the replacement medium (Aqueous Phase II) is flown into the chip until the flow front reaches the first resistance channel (Figure 3.2 B). The bubble traps ensure that a bubble-free liquid flows toward the micropillars. Then, by pushing the flow further in the membrane channel, the flow is partitioned into three separate streams when reaching the two rows of micropillars, and these three streams repetitively join again at the gaps. Lipid monolayers, which are present at the water-chloroform interfaces, join at the gaps and zip with one

another to form lipid bilayers, i.e. artificial membranes (Figure 3.2 C). This partitioning-zipping process goes on continually until all the gaps are filled with bilayers (Figure 3.2 D). At this stage, a part of the Aqueous Phase I flows through the resistance channel toward the exit 1 and the replacement channel. The amount of Aqueous Phase I in the resistance channel is limited since the resistance channel is engineered with a narrow size and an extended zig-zag length to induce a substantial pressure drop.

Once the lipid bilayers are formed, the pump feeding the membrane channel is stopped and the pump for the replacement media (Aqueous Phase II, which could contain drugs) is started. The replacement flow initially washes away all of the Aqueous Phase I that had reached the replacement channel out to outlet 2, after which outlet 2 is blocked. Then, Aqueous Phase II is pushed through the resistance channels (Figure 3.2 E) and fills the membrane channel. At this stage, the media around the lipid bilayers is fully replaced and the content of Aqueous Phase II (e.g. the drug) is delivered to the artificial membranes (Figure 3.2 F).

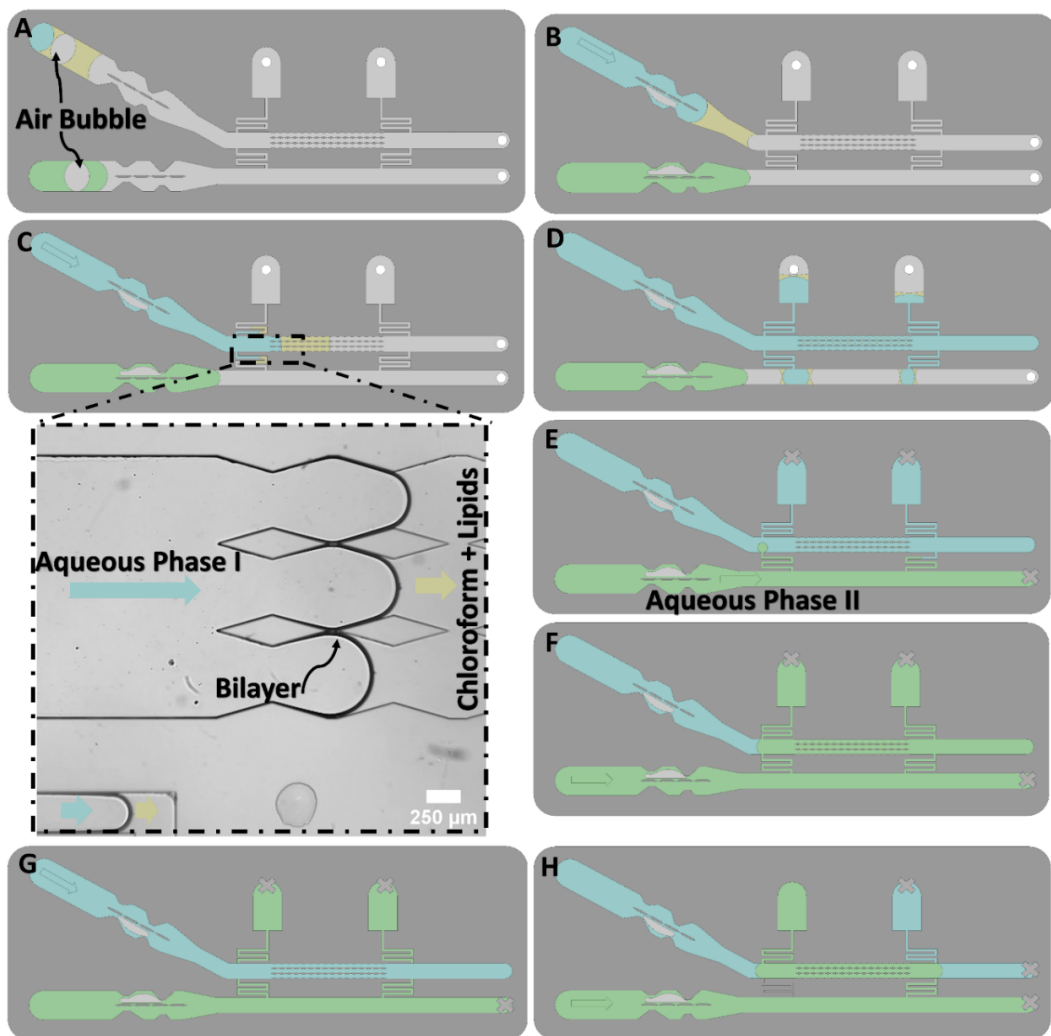


Figure 3.2: Schematic representation of different stages of chip function. A) Lipids dissolved in chloroform (yellow) are introduced from inlet 1 followed by the Aqueous Phase I (blue). The Aqueous Phase II (green) is introduced from inlet 2. B) Bubbles get trapped at the bubble trap. C & D) Replacement flow is stopped before the first resistance channel while the flow in the membrane channel is pushed further until membranes are formed at the gaps. E) After membrane formation, outlet 2 is blocked and the replacement flow is pumped into the system. F) Pumping is continued until all media around the bilayers is replaced by Aqueous Phase II. G) Aqueous Phase I can fill again the membrane channel by flowing Aqueous Phase I into the chip again, while outlet 2 and

both exit 1 & 2 are blocked. H) As a solution to the occasional clogging of the resistance channel (connected to exit 1), the second resistance channel can be implemented as a substitute.

Finally, the membrane channel can be filled again with Aqueous Phase I by simply running again the pump connected to the membrane channel while both exits are sealed (Figure 3.2 G). This can be useful for example when delivering fluorescent molecules to the artificial membranes and then washing those molecules from the channel after a specific time for fluorescent imaging with less background.

A second resistance channel and its corresponding exit port (exit 2), located downstream the micropillars section, are incorporated in the design in case the first resistance channel fails (Figure 3.2 H). This can happen if the first resistance channel is clogged by droplets formed via the unwanted mixing happening between chloroform and aqueous buffer at the connecting points of the resistant channels to the membrane channel or even in the resistance channel itself. In this case, both outlets and exit 2 are blocked, and the replacement media is pumped to go through the resistance channels and treat the membrane and finally leave the system from exit 1 port.

3.3 Flow simulation

To optimize and test the microchip, we used a finite element method (FEM) in COMSOL Multiphysics 5.6. The chip was designed taking three key criteria in

account: ensuring a symmetric flow on both sides of membranes at all time; keeping the drug concentration at desired level with even distribution over all membranes; and minimizing shear stress applied on the membranes to avoid rupturing them or altering their properties^{53, 58}.

Regarding the fluidic design of the system, the resistance channels should be long and narrow enough so the flow cannot easily go through them and leave the system during the membrane formation phase (criteria I). However, if they impose too much pressure drop on the flow, a very high fluidic pressure would be needed to flow the replacement buffer into the main membrane channel (criteria II). So, the optimized dimensions should satisfy both criteria. Regarding the junction point of resistance channels (the location from where the resistance channels branch out from the membrane channel) also one should consider the fact that they should be far enough from the micropillars so the affected flow streamlines due to the resistance channels are fully developed again by the time the flow reaches the micropillars.

The laminar flow in the channels was modelled using the laminar flow module in COMSOL^{62-63, 103-104}. In the first simulations, the pump connected to inlet 1 was run as done when membranes are formed (Figure 3.2 C) with an inlet flow rate of $5 \mu\text{l}/\text{min}$ ¹⁰². It is crucial that the flow remains symmetric at the gaps to ensure

that flat membranes form without any significant warping that may lead to membrane rupture. To help with flow symmetry across the gaps, a streamline-shaped design was used for the outer walls of the membrane channels (in the micropillars sections), making the geometry through which the liquid flows identical and symmetrical. The COMSOL simulations show that Aqueous Phase I reaches the micropillars such that the flow and pressure on either side of the gap remains similar during this phase (Figure 3.3 A-B). As a result, the three fingers of the flow partitioned by the two rows of micropillars behave similarly, with less than a 5% deviation between each finger for the average flow rate passing by the micropillars. Additionally, the corresponding resistance channels on either side of the membrane channel exhibit very similar behaviour, with less than 5% deviation in the average flow rate through each resistance. These two factors cause parallel streamlines and balanced pressure distribution (Figure 3.3 A) at the gaps throughout the micropillars section, which is favourable for the stable formation of flat membranes.

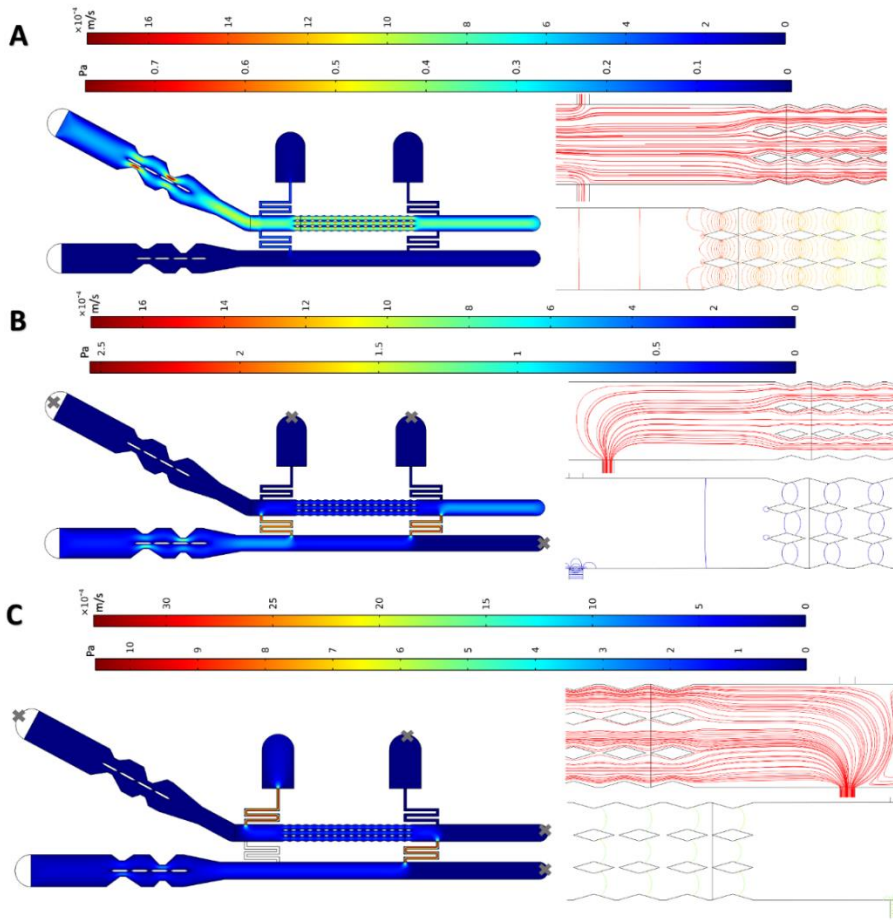


Figure 3.3: Flow simulation results for different stages of operation of the chip. Pressure distribution, velocity field, and flow pattern for the A) membrane formation, B) replacement, and C) fallback delivery stages. Grey crosses (x) in each figure indicate that in these simulations, the crossed-out inlet/outlet port was considered blocked. The left side of each panel represents the flow velocity field within the chip. The color bar indicates the color code for velocities. The right side of each panel shows (at the top) the flow streamlines when the flow is entering the pillar region, and (at the bottom) the pressure contours. The gradient of the color bar varies from blue to red (zero value to maximum value).

After membrane formation, the replacement flow is pumped into the system (as shown in [Figure 3.2 E-F](#)). This simulation was conducted with a flow rate of $2.5 \mu\text{l}/\text{min}$ infusing into the chip via inlet 2 ([Figure 3.3 B](#)). The streamline patterns at the gaps are parallel and a balanced pressure at all the gaps is observed. The crucial point in the replacement phase is that it is carried out in such a way to minimize shearing the membranes, thanks to the gap design and the profile of the micropillars, which create an almost zero-velocity stationary region between the gaps. A closer look at the simulation results of the velocity field around the gaps during the delivery phase shows this, as depicted in [Supplementary Figure S 3.2](#).

A simulation was also performed to evaluate the "fallback delivery" scenario (shown in [Figure 3.2 H](#)), which occurs if the first resistance channel becomes clogged and the second one is used for media replacement. The results for pressure distribution and flow patterns show that the flow remains symmetric and balanced at all the gaps ([Figure 3.3 C](#)), which is favourable for membrane stability.

COMSOL simulations were also used to investigate whether the molecule of interest at inlet 2 reaches all the membranes with a uniform concentration, and to determine the time required for Aqueous Phase II to fully replace Aqueous Phase I. To achieve this, we coupled the laminar flow equations with the dilute mass

transport equation, and solved them in 2D for molecular species with a diffusion coefficient of $D = 10^{-9} \text{ m}^2/\text{s}$ ¹⁰⁵. This simulation technique is well described in drug-delivery screening microchips^{62-63, 103}. [Figure 3.4 A](#) shows the time-dependent delivery of the new solution to the bilayer. The average local concentration at the last two gaps ([Figure 3.4 B](#)) shows that, in 170 sec, the two membranes furthest downstream receive the same concentration of delivered molecules (with less than 3% deviation) as the membranes upstream. In the case of using the second resistance channel when the first one is out of circuit (fallback delivery), it takes 70 sec for the membranes downstream to experience a complete media replacement ([Figure 4.4 C](#)). The homogenous delivery and short delivery times that are achieved with this chip highlight the effectiveness of a convection-based replacement method.

If the microchip is to be used for long term incubation times, it is important to consider the diffusion of the drug toward inlet 1 which is connected to the drug-free source. Our COMSOL simulations show that after the delivery phase is completed and the pump is turned off, the drug concentration around the first row of membranes (which are more exposed to serious concentration drop) drops by up to 2.5% in 1 hour, and 7% in 2 hours. To prevent this in long-term incubations, one can simply keep exit 1 open (while blocking all other ports) and keep the replacement flow pumping to the system during the long incubation time.

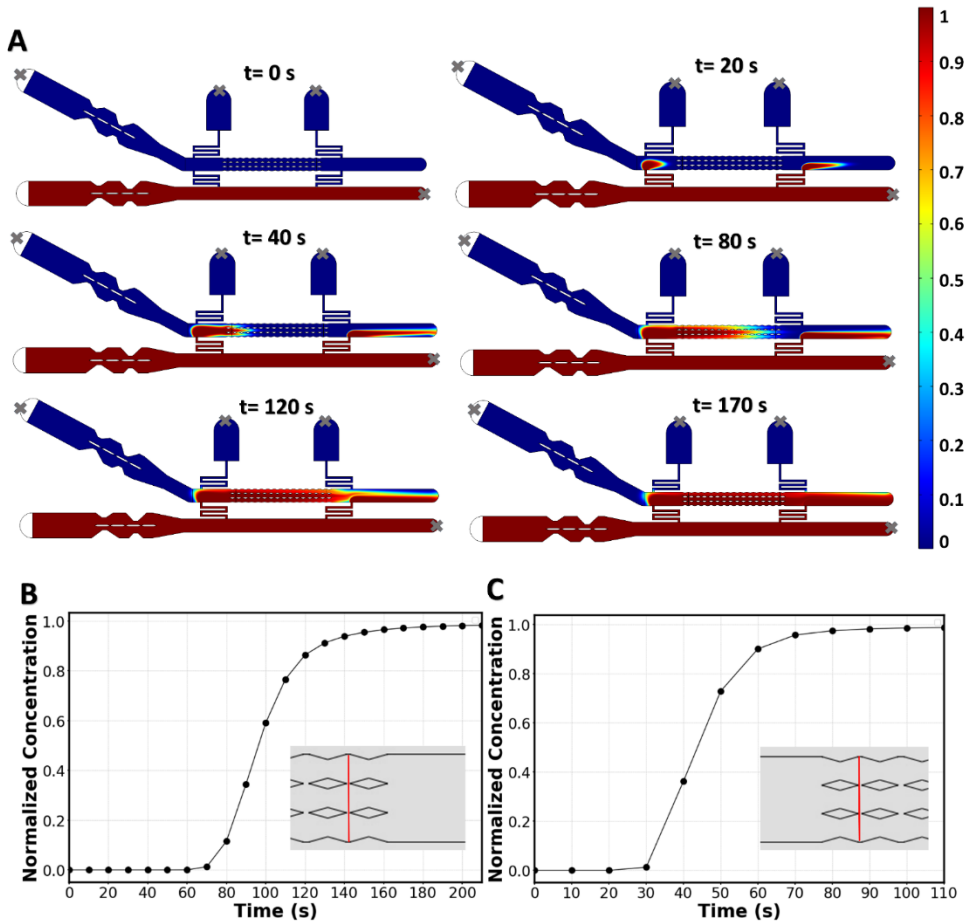


Figure 4.4: Results of the mass transport simulation. A) Timeline of media replacement simulated in COMSOL. The color bar represents the drug concentration normalized by the concentration at the inlet. Grey crosses (x) indicate the crossed-out inlet/outlet port was considered blocked. B) Average drug concentration at the last two membranes, normalized by the concentration at the inlet. The averaging is performed over the width of the membrane channel passing through the last two gaps (i.e. over the red line in the inset). C) Average drug concentration at the first two membranes during the “fallback delivery”, normalized by the concentration at the inlet. The averaging is done over the width of the membrane channel going through the first two gaps (i.e. over the red line in the inset).

3.4 Experimental characterization of media replacement around membranes

To experimentally observe the applicability of the chip in forming bilayers and delivering molecules of interest without disrupting the bilayers, a particle tracking experiment was performed. Chloroform containing POPC lipids was flowed from inlet 1, followed by the HEPES solution. Consequently, membranes were formed at the gaps of the micropillars, and after formation, the chloroform was absorbed into NOA81 until the annuli reduce in size²¹. During this process, some membranes may pop, but the remaining membranes maintain their stability at the gaps.

During the replacement phase, 2 μm polystyrene beads diluted 3000 times in the HEPES solution was introduced into the system from inlet 2 at a flow rate of 2.5 $\mu\text{l}/\text{min}$. Although the chip can handle higher flow rates (tested up to 9.9 $\mu\text{l}/\text{min}$), we experimentally found that 2.5 $\mu\text{l}/\text{min}$ was the maximum flow rate that can be used without causing warping of some membranes and risking their rupture.

To verify flow symmetry during the replacement process, particle flow around the first membrane (the one at the highest risk of flow asymmetry) was tracked using ImageJ. The streamlines of the flow were found to be parallel to the channel's direction (Figure 3.5 A), as predicted in simulations (Figure 3.3 B). Additionally, we

conducted a count of membranes that were initially formed and that survived after the flow replacement with beads (Figure 3.5 B), showing that while some membranes did not survive the process, a significant number of membranes (on average 77% of the initially formed membranes) remained intact following the flow replacement on the chip, allowing for subsequent measurements.

At flowrates around $2.5 \mu\text{l}/\text{min}$, membranes start to warp as shown in Figure 3.5 A. However, the membranes remain stable and after the flow is stopped the membranes flatten. Above $2.5 \mu\text{l}/\text{min}$, the warping risks to disrupt the membrane. For particle tracking, the maximum flowrate ($2.5 \mu\text{l}/\text{min}$) is chosen to minimize beads sinking in the channel while traveling in the channels, which would affect particle tracking.

To experimentally assess the concentration of molecules delivered to the membranes and the minimum time required to achieve a homogenous concentration throughout the chip, a laser-induced fluorescent test was conducted. For this purpose, chloroform (no lipids) followed by the HEPES solution (no beads) were flown into the system from inlet 1 and when the membrane channel was filled, Rhodamine B in the HEPES solution was pushed from inlet 2 at the rate of $2.5 \mu\text{l}/\text{min}$. The relative change in Rhodamine-B concentration at the most downstream gaps were recorded over time. Within ~ 200 seconds the dye

concentration around the last gaps reaches the input concentration (Figure 3.5 C) as predicted from the mass transport simulations (Figure 3.4 B).

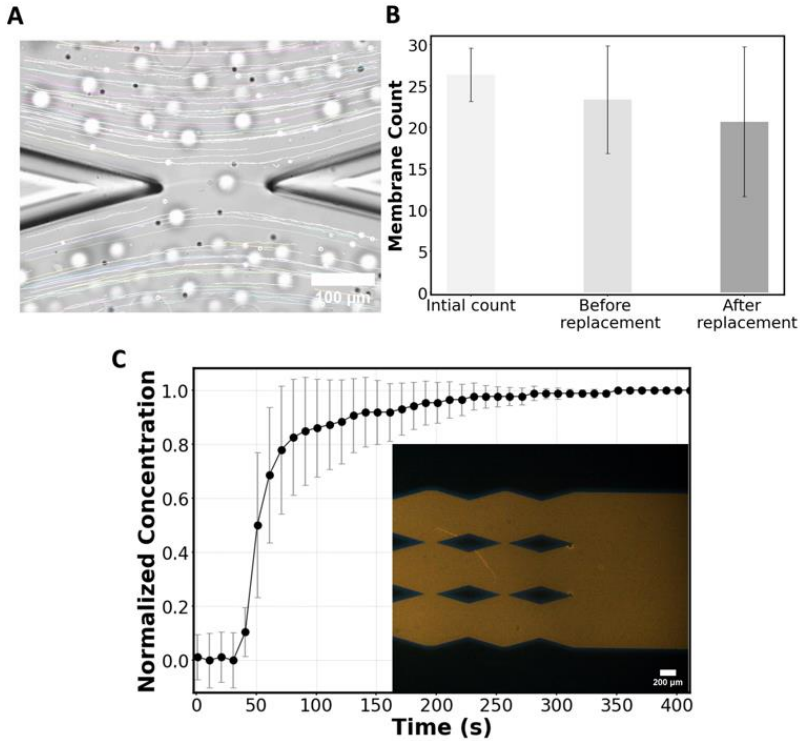


Figure 3.5: Experimental validation of the chip. A) Flow streamlines around the first membrane illustrated by tracking 2 μm beads. B) Membrane count just when they are formed, after 1 hour of formation, and after the surrounding media of the membranes is replaced via the replacement channel; from 3 independent experiments. C) Rhodamine-B concentration (normalized fluorescent intensity) at the location of the two last membranes normalized over Rhodamine-B concentration at the inlet of the drug channel. Data points are averaged over 3 independent experiments. The inset

of panel C shows an image of the distribution of Rhodamine-B around the last gaps 170 sec after the start of the media replacement procedure.

3.5 Materials and Methods

3.5.1 Microfluidic chip fabrication

The master mold was fabricated following conventional cleanroom techniques. Briefly, positive resist S1813 (MICROPOSIT®) was spincoated on a 4-inch silicon wafer to reach a thickness of $\sim 3 \mu\text{m}$. The design of the chip was drawn in Autocad and converted into a dxf file using Klayout. Utilizing a laser writer (μMLA , Heidelberg Instruments) the design was patterned on the resist and later developed for 80 seconds in MF322 solution (MICROPOSIT®), followed by rinsing with deionised water. The mask was spun to dry. The developed mask was descummed with low power plasma (100 Watts for 5 minutes) and then etched using PlasmaPro 100 Estrelas DRIE (Oxford Instruments) to reach a channel depth of approximately $75 \mu\text{m}$. For the etching process, conventional Bosch process of silicon etching was implemented. To remove any remaining resists, the final mold was immersed in remover (Ar600-71), sonicated for 5 minutes and rinsed with isopropanol. The mold was then dried using nitrogen gas. Then, plasma cleaning (PVA Tepla 300) was performed on the mold (600 Watts for 5 minutes). Finally, vapor deposition of trichloro (1H,1H,2H,2H-perfluorooctyl)silane (PFTOS, Sigma-Aldrich) on the mold was done overnight in a vacuum chamber. For the silanization, 50 mL of the PFOTS silane was placed in a glass tube and connected to the evacuated chamber via a

tightly sealed connector. The chamber was maintained under vacuum for at least 2 hours to allow the silane to vaporize and treat the mold surface.

The PDMS mold was fabricated by first thoroughly mixing PDMS with its curing agent (SYLGARD®) in a 10:1 (mass) ratio. The mixture was then degassed in a standard desiccator. Casting of PDMS onto the master mold was followed by another round of degassing. Subsequent curing was accomplished in an oven at 85°C for 8 h. After curing, PDMS was carefully diced out from the master mold, and surface silanization with PFTOS was performed as described above.

Finally, NOA81 (Norland Products) was cast onto the PDMS mold. A microscope glass slide was placed on top of liquid NOA, allowing it to flatten and form a uniform layer beneath it. Subsequently, the assembly was exposed to UV light (Promed UVL-36 with four UV-9W-L bulbs) for 5 min. Following UV exposure, the PDMS was peeled off from the NOA channels. All ports were drilled with 1mm drilling tips. NOA81 was spin-coated onto a glass coverslip (Deckglaser, thickness: $170 \pm 5 \mu\text{m}$, previously thoroughly washed with Hellmanex and rinsed), and partially cured for 1 minute. The NOA-coated coverslip was then bonded to the NOA channels. The bonded chip was exposed to the same UV light for 10 minutes (for enhanced bonding and curing) and subsequently baked for 8 h at 85 °C on a hot plate.

3.5.2 Chemicals, buffers, lipids, and flows

To create the aqueous phase that we refer to as the HEPES solution, 10 mM 4-(2-hydroxyethyl)-1-piperazineethanesulfonic acid (HEPES) was adjusted to pH 7.4 using concentrated KOH, KCl (150 mM) and bovine serum albumin (0.5 mg/ml) were added, and the solution was filtered with a 0.2 μ m sterile filter. For the bead-containing experiments, after filtration, 2 μ m polystyrene beads (real diameter= 1.93 μ m, Polysciences Inc.) were dissolved in the buffer. Two identical ProSense NE-30 syringe pumps were used to infuse the flow into the chip via inlet 1 and inlet 2. To minimize the residual flow after stopping the pumps, tubing with short length was used (no longer than 5 cm). For membrane formation, flow rates in the range of 5 – 9 μ l/min usually gave several stable bilayers. However, for the (reversible) replacement of the media we advise to use a flow rate of 2.5 μ l/min. For the laser-induced fluorescent tests, Rhodamine B was dissolved in the HEPES solution. For the drug experiment, azithromycin (Sigma-Aldrich) was dissolved in 0.1 M HCl and then added to the HEPES solution to reach final azithromycin concentrations of 5 μ M or 250 μ M. For blocking outlet ports during the drug delivery phases, UV curing glass repair adhesive (Bison) was used.

3.5.3 Numerical simulations

All simulations were conducted using COMSOL Multiphysics 5.6. To model the fluid flow, two COMSOL modules were used: one to model the laminar flow and another

to model the transport of dilute species. The fluid flow was solved in steady-state, and a time-dependant study was implemented for the mass transport model. Free triangular mesh was used in the two-dimensional domain of the chip with the average skewness quality of 93%.

3.5.4 Video and image analysis

To track the beads for the observation of flow streamlines, the TrackMate module of ImageJ was used. To pre-process the images, all the stacks were subtracted by the average image of all the stacks to remove the chip structures and the background noises. Then, the intensity was reversed to have high intensity for the beads and a dark background. Laser-induced fluorescent tests were analysed in ImageJ without any pre/post-processing via measuring the average grey scale value.

3.6 Supplementary information

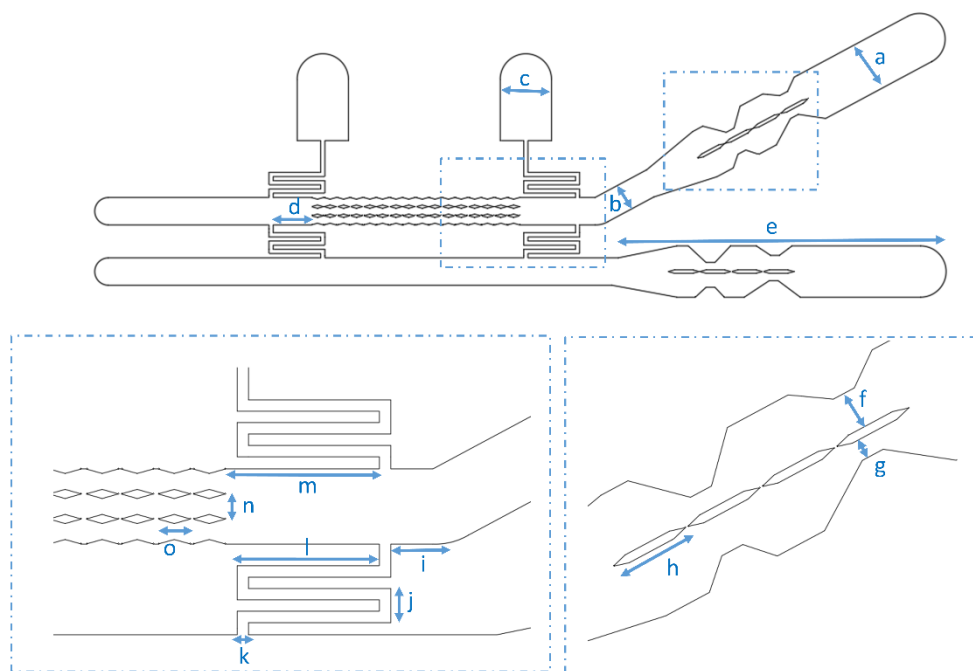


Figure S 3.1: Top: 2D drawing of the microchip with selected dimension parameters (summarized in table S 3.1)

Table S 3.1: Microchip dimensions (see Figure S 3.1).

Dimension parameter	Value (μm)
a	3093
b	1650
c	3093
d	2326
e	19783
f	880
g	450
h	1831
i	1082
j	750
k	250
l	3119
m	3384
n	550
o	693
Gap distance	75 and 120

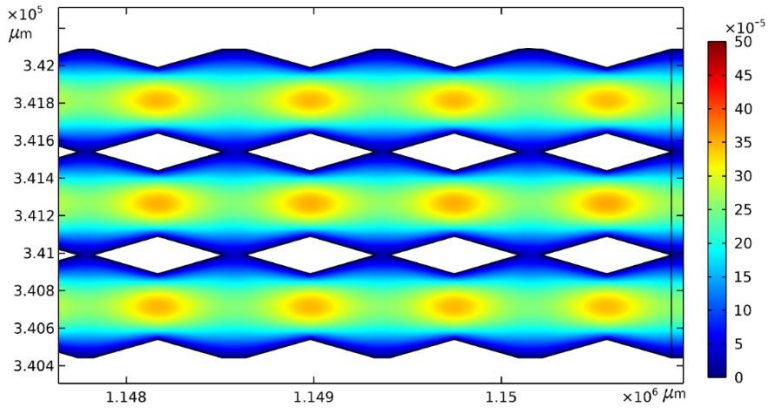


Figure S 3.2: COMSOL simulation results for velocity field (m/s) at the vicinity of the membranes during the delivery phase. The x and y axis shows the geometrical dimensions and the colorbar presents the velocity in m/s.

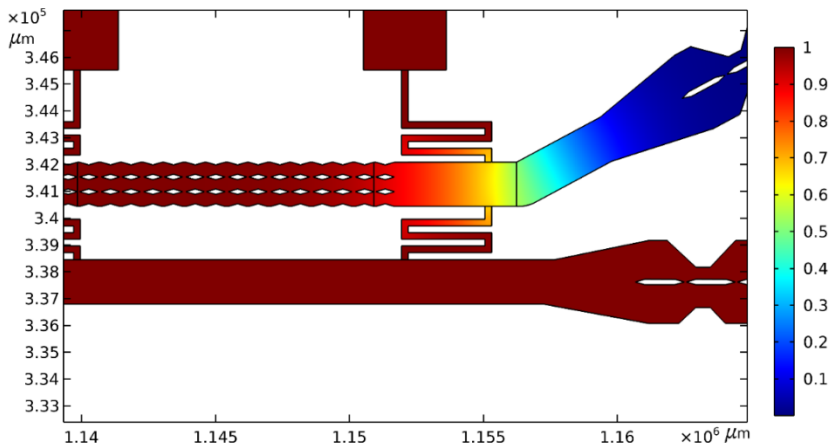


Figure S 3.3 – COMSOL simulation results for mass transport. Normalized concentration distribution of the drug in the chip 2 hours after stopping the flow. The x and y axis shows the geometrical dimensions and the colorbar presents the normalized drug concentration (normalized to the inlet concentration).

Chapter 4

A single-gap microfluidic chip for electrical characterization of lipid bilayers

Abstract

With the increasing popularity of freestanding lipid bilayers, we describe a robust microfluidic platform that enables transmembrane electrical recordings on freestanding lipid bilayers. For such experiments, the main challenge stems from fluid dynamics aspects where even minor disturbances in hydrodynamics, such as pressure imbalances and fluidic instabilities, can compromise the integrity of the flaccid lipid membranes. We therefore introduce a new design to overcome the challenge of online microfluidics pressure balancing of the thin films/interfaces, which greatly improves the versatility and success rate of bilayer-on-chip platforms. The design is based on the integration of bidirectional fluidic diodes into the chip contributing to the passive balancing of pressure at the location where the membrane is formed, resulting in the rapid and robust formation of freestanding lipid bilayers suitable for probing electrically and interfacing with optical biophysical techniques (microscopy, optical tweezers, ...). The proposed design conveniently functions using conventional syringe pumps without any need for off-

chip pressure balancing strategies. We first quantified the performance of the fluidic diodes in mitigating hydrodynamic instabilities and balancing the pressure at the membrane. Then, through an illustrative example, we validated the functioning of the chip via measuring the electrical capacitance of freestanding planar 1-palmitoyl-2-oleoyl-glycero-3-phosphocholine (POPC) bilayers. We believe that the present microfluidic design can potentially be used to form and characterize asymmetric lipid bilayers.

4.1 Introduction

Several *in vitro* systems have been developed for the formation and studying of lipid bilayers.^{22, 29, 33, 84, 106-112} Specifically, for the formation of vertically freestanding bilayers, various single-gap (a single membrane on one chip)^{22, 108} and multi-gap (arrays of membranes on one chip)^{21, 113-114} designs are currently in use. Multi-gap chips are more common in the literature since the single-gap systems fed by two pressure sources (two separate pumps) face the challenge of pressure balancing, which causes very low success rate of membrane formation.^{21, 113-114} In multi-gap chips, however, the system is typically controlled by one pressure source and, since all the structures are accommodated in a single channel fed by the same flow, the media on both sides of the membrane are directly connected and mixed. This eliminates the issue of pressure balancing across the membrane, and significantly increases the success rate and stability of bilayer formation.^{21, 114} However, due to this direct mixing, several biologically relevant experiments cannot be performed on multi-gap chips. For instance, transmembrane electrical recordings^{29, 115}, membrane permeability tests,¹¹¹ or the formation of membranes with asymmetric conditions (asymmetric buffer or leaflets with different lipid compositions)^{29, 108} all require single-gap systems with isolated buffers on each side of the membrane leaflets (no mixing or cross-contaminations).

To design a robust single-gap platform that does not suffer from hydrodynamic issues, it is necessary to first understand the nature of pressure imbalances in microfluidic

channels. Disturbances upstream the flow (pressure differences at the inlet and flow instabilities stemming from the pumping system) in microfluidic channels result in transient changes in flow rate or pressure downstream the chip.¹¹⁶ Managing and mitigating these instabilities to achieve a balanced fluidic pressure in microfluidic systems are then of utmost importance.¹¹⁷⁻¹¹⁹ These issues become more important especially in microchips featuring multiple inlets,^{62-63, 120-121} where even slightest flow instabilities between the two inlets may cause pressure imbalances that lead to a large crossflow and failure in the function.¹²² So, balancing pressure in a microfluidic chip involves adjusting and equalizing the pressure at specific points to ensure that parallel channels operate with minimum crossflows,¹²³ which is more demanding in multiphase microfluidics system concerning thin film/interface studies^{116, 124-127}. More specifically, balancing pressure at the location of microfluidic gaps where freestanding planar lipid bilayers are formed is a well-known challenge^{29, 108, 114}, since disruption or the creation of undesired curved membranes (warping) happens with the slightest unfavourable hydrodynamic disparity on flaccid lipid bilayers.^{58-59, 114} However, pressure imbalances are an unavoidable occurrence, even when meticulous efforts are made to optimize the chip, pumping system, and tubing.¹²⁸ Due to the hurdle of fluidic pressure balancing at micron-scale, pressure balancing as a necessity for the function of a chip, since it implies the utilization of off-chip pressure balancing strategies or on-chip technical difficulties, is often referred to as a downside in the design as it requires.¹²⁹

Both passive^{116, 122, 130-131} and active^{124, 127, 132} techniques are employed in the literature to achieve a balanced pressure in microfluidic systems. The conventional passive method for equalizing fluidic pressure in microfluidic systems with two inlets involves establishing a direct connection between the two flow streams, which unavoidably results in the mixing of these streams.¹³³⁻¹³⁴ To avoid mixing, indirect connection methods have been proposed which rely on a third phase media like an immiscible oil to mechanically connect the two flows at the outlet.¹³⁰ Such methods are suitable for concentration gradient generator chips, where an instantaneous and constant balancing of the pressure is not required and pressure balancing does not take place unless both streams reach the outlet and get in touch with the oil. However, for membrane or thin film studies, an online instantaneous balancing of the pressure is required at the moment of the interface formation and also after its formation.^{22, 108, 114, 124} Current platforms for membrane or thin-film studies rely on off-chip methods like pressure controllers, which introduce complexity to the system.¹²⁴ Alternatively, certain chips require off-chip hydrostatic pressure control¹⁰⁸ and pressure pumps²² to form membranes at extremely low flow rates. This imposes limitations on the choice of non-aqueous phase solutions. For example, in case of chloroform, it cannot remain in the channels for extended periods (since it is absorbed to much by the chip material and can lead to swelling or delamination), and higher flow rates are typically necessary for optimal operation.¹¹⁴

In this work, an integrated pressure-balancing microchip is developed that facilitates the arduous process of forming freestanding planar membranes on single-membrane chips while prohibiting cross-contamination between channels. This microchip enables rapid formation of a single bilayer without the solvent choice constraints customary in prior devices. The present chip is suitable for both transmembrane recordings and independent control over each membrane leaflet. The chip functions with two conventional syringe pumps. However, there is no need to use off-chip components like pressure regulators or flow stabilizers. This is achieved through the integration of passive fluidic-diodes into the chip that equilibrate the pressure and stabilize the flow in a valve-free manner. To prove the concept, we first experimentally validate the performance of the fluidic diodes in balancing pressure and mitigating fluidic fluctuations. Secondly, to demonstrate the applicability of the chip in transmembrane recordings, we measured the electrical capacitance of POPC bilayers under both symmetric and asymmetric conditions.

4.2 Microfluidics system description and working principles

The architecture of the proposed microfluidic chip design is illustrated in [Figure 4.1 A](#). The chip is made of Norland Optical Adhesive (NOA81) and comprises two inlet ports, each dedicated to one leaflet and its respective aqueous medium flow. To ensure both flows are bubble-free, previously reported passive bubble-traps of chapter 2 ¹¹⁴ are incorporated into the chip on both sides. To handle fluidic instabilities and balancing pressure, bidirectional fluidic diode balancers are used in the design, as illustrated in

Figure 4.1 A. A microfluidic diode is a fluidic component that becomes activated when a specific pressure differential is applied across its ends, allowing it to relieve the pressure in either a unidirectional or bidirectional manner.¹³⁵⁻¹³⁶ In one-directional diodes, pressure can only be relieved in one direction, while flow is blocked in the opposite direction. Fluid can pass through the diode only if the pressure in the permitted direction exceeds a certain threshold. In contrast, no flow occurs in the opposite direction, regardless of the pressure difference, because the diode's geometry and internal physical barriers are designed to open only in one direction.¹³⁷ However, in the bidirectional diodes the flow can work in either way to balance the pressure between its ends.¹³⁶ In the present design, our bidirectional diode-based pressure balancers are basically a series of X-shape slits confined within two cylindrical micropillars, one upstream, and eight downstream from the main gap, where the membrane is formed.

The pressure balancers enable connections between the two flows on either side (aqueous phases I and II), albeit in an indirect manner via a third phase (organic phase) that is trapped in the X-shaped slit as presented in **Figure 4.1 B**. In this way, the higher pressure on one side is equilibrated with the lower pressure on the opposite side through the connection, all while strictly preventing any mixing or cross-flows between the two sides. The balancer only plays a role when the difference in pressure between the channels is between thresholds: $P^- < \Delta P < P^+$, where ΔP is the pressure difference, while P^+ and P^- are the diode's thresholds (**Figure 4.1 C**). When there is no significant

potential difference between the two ends ($P^- < \Delta P < P^+$), there is no flow through the diode. However, a flow appears (with the diode becoming a shortcut) when the imbalance of potential is higher than the operational limits of the diodes ($|\Delta P| > |P_{break}^+|$ or $|P_{break}^-|$). The thresholds are essentially the penalty to overcome the surface tension of the four involved interfaces at the slit resisting against any surface area changes.¹³⁵ This resistance is enhanced with the presence of micropillars at the slit since they induce higher curvature to the involved interfaces. Although with curved interfaces the diode would be less sensitive to pressure imbalances, the capacity of the diode to handle larger pressure differences is increased (higher thresholds). All diode parameters such as P^+ , P^- , and P_{break} in [Figure 4.1 C](#) are dependent on the surface tension of the four involved interfaces and the geometry.¹³⁵ Clearly, the presence of lipids (here POPC was used) and other agents in the organic phase as well as the buffer composition (here, HEPES) affect the function of the system, hence the need to quantify balancers specifically in each application.

For better clarification, the chip structure can be explained also using a simplified electrical analogy where the flow rates from the pumps are equivalent to constant input electrical currents, hydraulic pressure drop is equivalent to electrical resistances,¹³⁸ and the pressure balancer is considered as a bidirectional diode that stabilizes the current and relieves any imbalance potentials^{136, 139-140} ([Figure 4.1 D](#)).

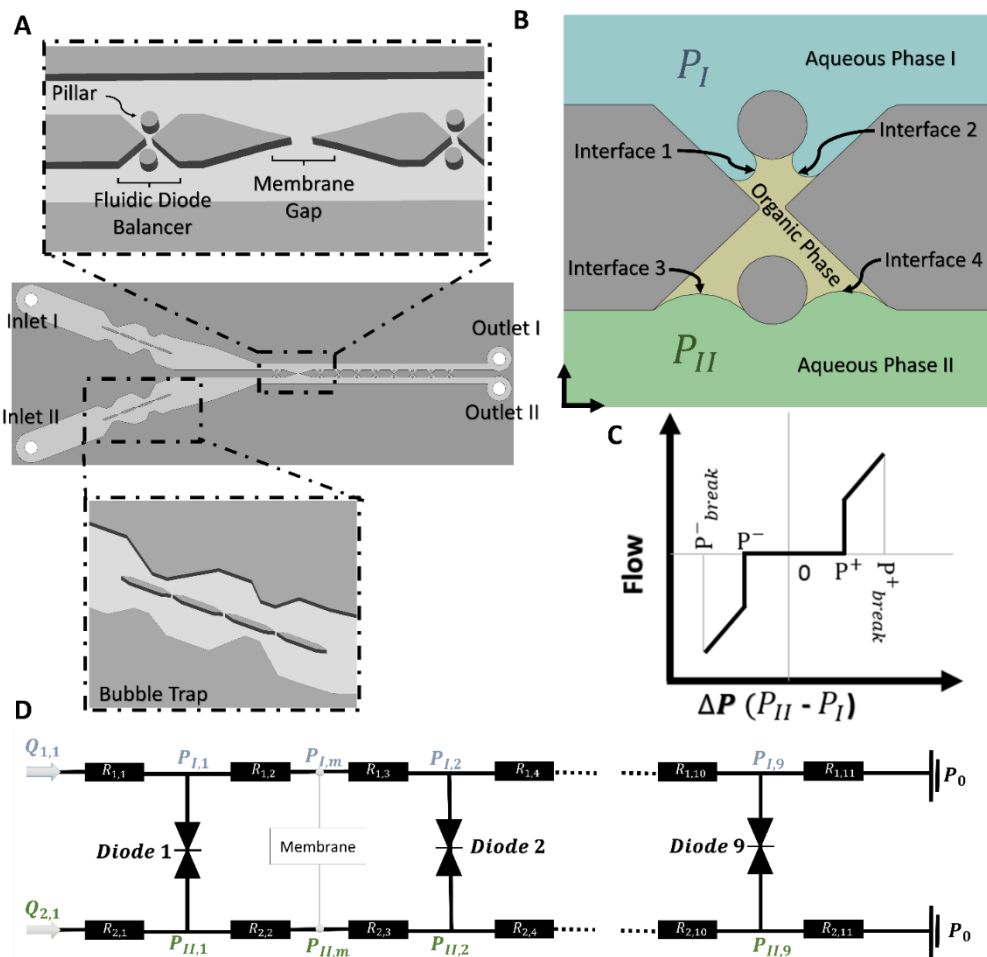


Figure 4.4: A) Microfluidic chip design and the structural details The chip contains bubble traps, balancers for pressure balancing, and a gap for membrane formation. B) Schematic representation of the fluidic diode (X-slit balancer) where the organic phase is isolated between the aqueous buffers. C) Schematic operational curve of the balancer behaviour as a function of the pressure difference, showing that the diode is activated only if the pressure difference between buffers equals

the threshold parameter D) Equivalent electrical circuit of the microfluidic chip where the balancers are considered as bi-directional diodes and the channels as electrical resistors.

For membrane formation, the organic phases (lipid dissolved in chloroform) followed by their corresponding aqueous media (HEPES buffer) are flown through each inlet independently via syringe pumps at equal flow rates (Figure 4.2 A). Unwanted bubbles at the HEPES-chloroform interfaces are trapped by the bubble traps and so the system is provided at both branches with bubble-free HEPES-chloroform interfaces (lipid monolayers)¹¹⁴ (Figure 4.2 B). As the flows proceed downstream the system, chloroform from both branches fills all the channels and also the X-shaped balancers (Figure 4.2 C). Consequently, a higher pressure in one branch, i.e., the blue-coloured stream in Figure 4.2 C, will directly affect the low-pressure (green-coloured) flow and push it backwards. At the next stage, when the HEPES streams are pushed downstream the channels, they both displace the organic phases on both sides but confine some chloroform between the micropillars at the X-shaped slits (Figure 4.1 D). Over time, some of the trapped chloroform may get absorbed by NOA81. However, a sufficient amount of chloroform will remain to prevent any cross-contamination between the two aqueous buffer streams. Now, the two parallel flows in the channels are connected indirectly via the chloroform in the balancer upstream the main gap and also directly via the sea of chloroform downstream the main gap. This synchronizes the instabilities and promotes a balanced pressure at the gap, which is crucial for lipid leaflets zipping.¹¹⁴ These synchronized flows

eventually converge at the main gap where the leaflets zip together, forming a membrane. At this stage, it is essential to continue operating the syringe pumps to push the chloroform away from the membrane and out of the system. Hence, a series of balancers are included after the gap until the outlet, ensuring an indirect flow-flow connection (Figure 4.2 E) everywhere throughout the chip. In this way, pressure differences (ΔP) are handled with balancers enhancing the flatness of the membranes (Figure 4.2 F). The maximum extent of pressure imbalance which can be handled by the balancers is up to the moment that the flow on the high-pressure branch fills the balancer slit and connects the flow on the other side (the inset of Figure 4.2 F, $P_I \gg P_{II}$).

To assess the role of the balancers (fluidic diodes), we compared the success of POPC lipid membrane formation in devices with versus without balancer structures (Figure 4.2 G). Without the balancers, membranes would either not form at all, or would be highly curved (Figure 4.2 G) and only last a few seconds at most. With the balancers, relatively long-lasting flat membranes (in the order of several minutes) could be formed (the inset of Figure 4.2 E).

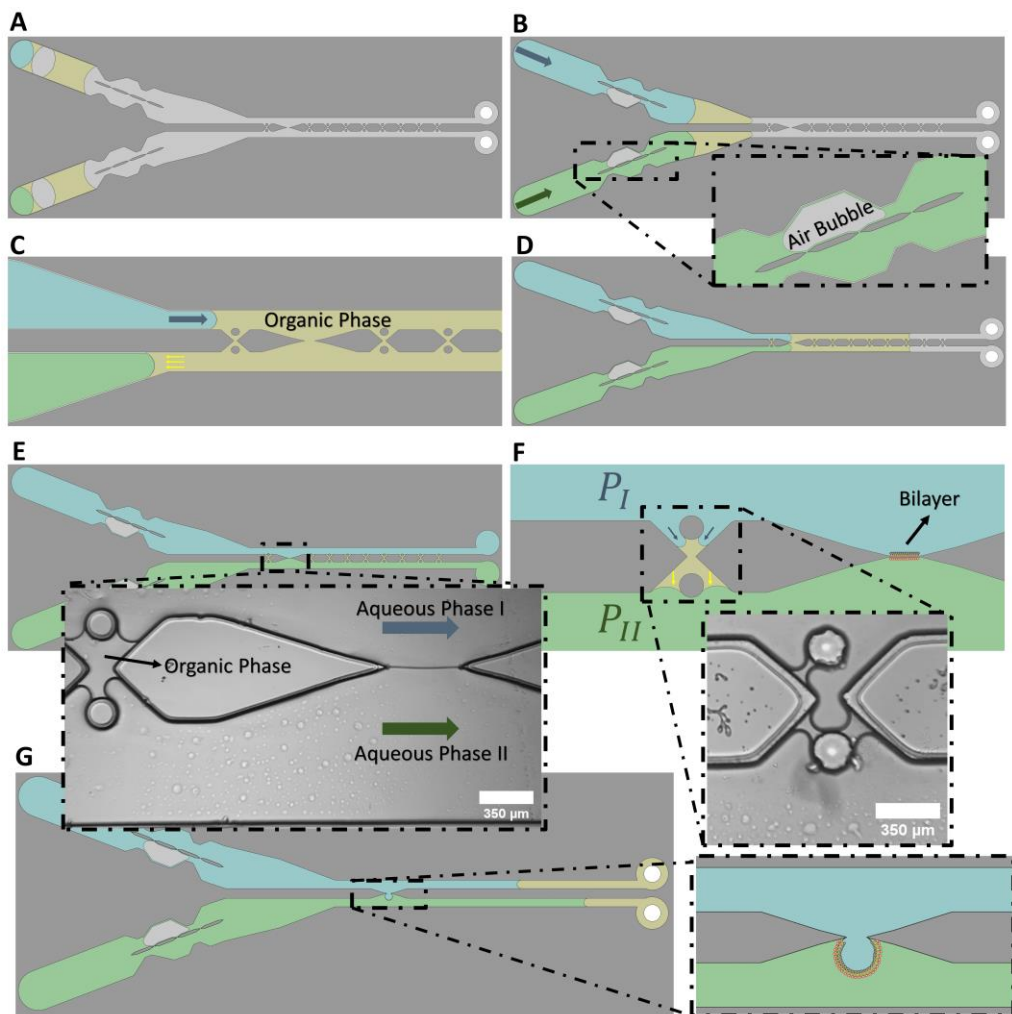


Figure 4.5: Schematics of the chip function and membrane formation process. A) The organic phase (chloroform with lipids, yellow) followed by the aqueous phase (aqueous phase I, blue-coloured medium) is flown from one inlet by a syringe pump. From the other inlet, using another syringe pump, organic phase followed by its corresponding aqueous medium (green) is flown into the system. B) The bubble-traps remove any potential bubble carrying by the flow specifically at the interface of the organic/aqueous phase. C) Chloroform fills the chip and the balancers initially. At this stage,

an indirect fluidic connection between aqueous phases is established. Pushing the flow on one side (higher pressure) will be transferred to the other side consequently and the blue/yellow interface retracts. D) Both flows are pushed at equal flow rates toward downstream the chip. Prior to the membrane gap, both parallel flows are indirectly connected via the organic phase trapped in the X-slit balancer. At the gap and downstream the gap, also a continuous chloroform phase is present and makes the connection. This full connection prior and after the gap guarantees the balance of pressure at the gap. E) Pushing further, the two lipid monolayer interfaces (leaflets) are zipped together and the bilayer is formed at the membrane gap. F) Any imbalances in pressure or fluidic disturbances will be balanced out via the X-slit balancers via relieving the higher pressure from one side to the other side. Clearly, the pressure difference is tolerated up to the extent where interfaces from either sides do not collide. G) Schematic of the control experiment on a similar chip without the X-slit balancers. Due to the absence of any fluidic connection, the pressures in the parallel channels remain independent of each other. The channel with lower pressure drop or higher pressure at the source disrupts the pressure balance resulting in the crossflow at the gap, which prohibits membrane formation or leads to the formation of unstable curved membranes.

4.3 Device characterization

To experimentally validate the device's performance from the fluid mechanics point of view, our initial step involved assessing pressure equilibrium within the gap and also to show how quickly the two streams are balancing each other. To do so, we utilized particle image velocimetry (PIV) analysis of $2\mu\text{m}$ polystyrene beads being flown at a constant flow rate via the pumps in the vicinity of the membrane gap and kymograph analysis of the four HEPES-chloroform interfaces at the balancer slits. The important consideration here

is that the constant flow rates from the pumps should meet the technical requirements of the microfluidic chip (high enough to limit the time chloroform stays inside channels which may cause swellings/delamination) while accommodating the preferable hydrodynamics for membrane formation (controlled in a way that the balanced pressure promotes membrane formation).

We first tested the flowing of chloroform containing POPC lipids, followed by bead-laden HEPES buffer at each inlet, using a relatively high flow rate ($5 \mu\text{l}/\text{min}$) (Figure 4.3 A-C). At such high flow rate, the bead tracking shows that beads can travel from one channel to the neighbouring one by crossing in the gap (Figure 4.3 A), because the balancers fail (Figure 4.3 -C). Then, we tested the same protocol at a reduced flow rate of $2.5 \mu\text{l}/\text{min}$. As the bead tracking demonstrates in Figure 4.3 D, symmetric streamlines are now observed about the midline of the gap. Hence, due to the balanced pressure, the flows from either sides are not crossing through the gap to the other side. This is the ideal condition for membrane formation that happens automatically in multigap systems being fed by one syringe pump^{21, 114}, which is achieved here thanks to the balancers despite the system is being fed with two independent pumps. So, any flow rates below $2.5 \mu\text{l}/\text{min}$ would be hydrodynamically favourable. However, a too low flow rate can sometimes also be problematic since it increases the time during which chloroform stays inside the channels, potentially leading to swelling and delamination of the chip¹⁴¹.

To observe how quickly the flow is balanced, we tracked (with bright field microscopy) the movements of the four interfaces present at the balancer slits just before the formed membrane while the flow was continuously running at $2.5 \mu\text{l}/\text{min}$. The kymographs of fluctuations for the four interfaces (depicted in [Figure 4.3E](#)) are plotted in [Figure 4.3F](#). As it can be seen in [Figure 4.3F](#), at $2.5 \mu\text{l}/\text{min}$ flow rate, the pressure at the membrane gap is balanced and the balancers instantly equilibrate any disturbances between the sides, providing ideal conditions for membrane formation. The upward and downward fluctuations in the kymograph plots of the interface 1 and 3 are synced, showing the rapid translation of any fluctuations from one side to the other side. The slopes in the kymographs are the translational movements in the interfaces due to the total increase/decrease of the pressure on one side.

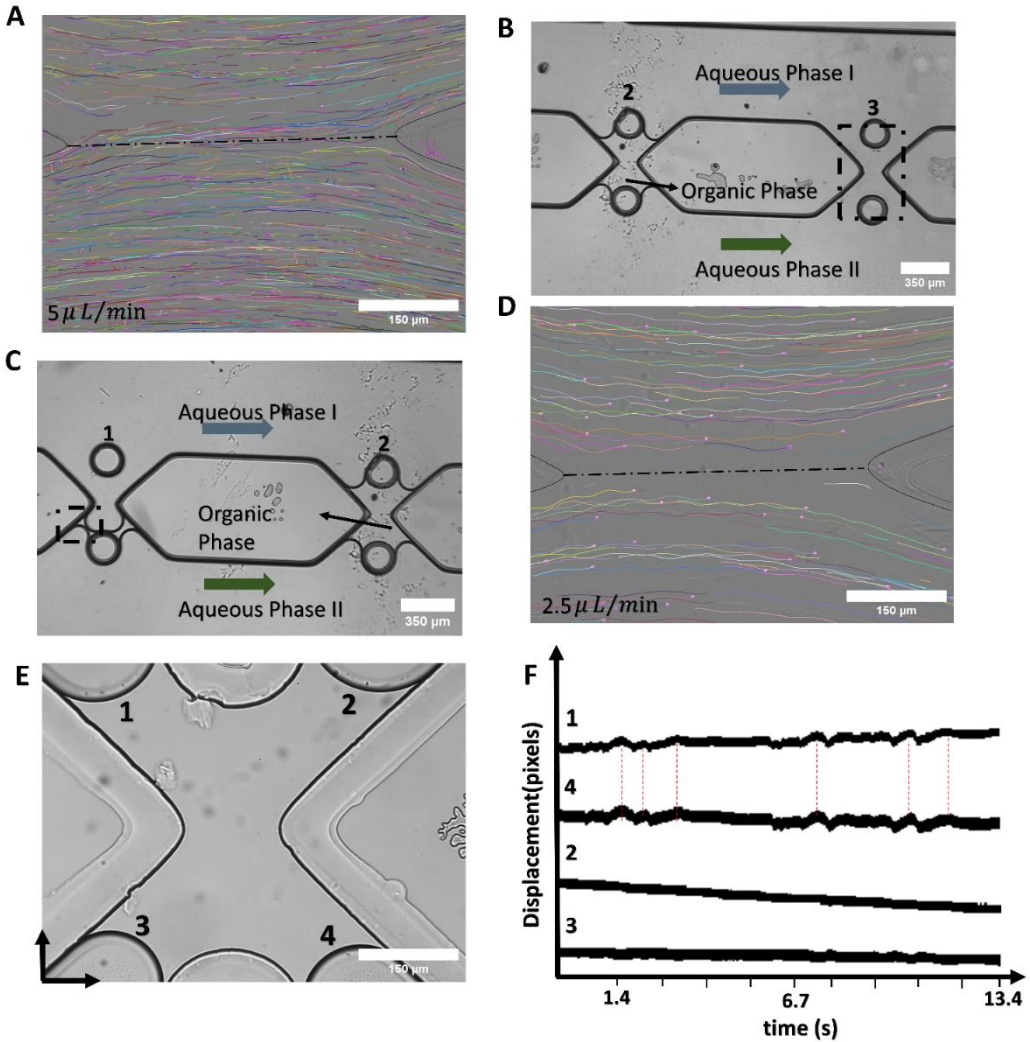


Figure 4.6: A) Flow streamlines at the gap when a flowrate of $5 \mu\text{L}/\text{min}$ is used. A clear crossflow can be seen at the gap (flow streamlines passing through the dashed line). B & C) Pictures of balancers when a flow rate of $5 \mu\text{L}/\text{min}$ is used. The fluid flow direction is shown with green and blue arrows. Some balancers (e.g. panel B balancer # 3 in the dashed square) fully fail, causing mixing between the sides, while in others (e.g. panel C balancer #1 in the dashed square), interfaces

have collided, which is unfavorable as it affects the measured electrophysiological measurements. D) Flow streamlines at the gap when a flow rate of $2.5 \mu\text{l}/\text{min}$ is used. A balanced pressure at the gap is obtained. E) Picture of balancer (with HEPES-chloroform interfaced numbered) prior to the gap for the flow rate of $2.5 \mu\text{l}/\text{min}$, where no mixing or collision is observed. F) The kymograph analysis of the four interfaces (numbered in E) shows an immediate effect of events on one side on the other side, making the pressure on both sides well synced to each other.

4.4 Lipid membrane formation and electrophysiology on chip

In electrical studies of lipid membranes, the bilayer is usually considered as a parallel capacitor-resistor system (non-ideal capacitor)¹⁴². Figure 4.4 A illustrate the experimental setup utilized for electrophysiological measurements. In this study, in contrast to the traditional way of inserting the electrodes into the chip²², electrodes were connected to the media via a 3D printed T-connector in the tubing. In this way, there is no need for incorporating the electrodes directly into the chip, which usually brings technical hurdles.

A representative curve of capacitance measured during the formation of a POPC membrane is shown in Figure 4.4B. Using the full cross-sectional area of the gap as the membrane's surface area (i.e., assuming that the annulus can be neglected), we estimated the specific capacitance to be $0.6 \pm 0.1 \mu\text{F}/\text{cm}^2$. This value falls within the range of previously reported values for bilayers composed of POPE:POPG or DPhPC:DOPC:DPPC^{22, 143}, suggesting that the annulus is so small that it can indeed be neglected. It is important to note that in the presence of solvent between the leaflets, the specific capacitance was

shown to be below $0.5 \mu F/cm^2$ in case of membranes composed of DOPC.¹⁴⁴ The extent of this decrease depends on the solvent composition and the quantity of solvent present in the bilayer.¹⁴⁴ On average, we found the formation time of the membranes (time between initial contact of the interfaces at gap until moment the capacitance value is stabilized) to be 2.7 ± 0.4 seconds based on three measurements.

We also tested very low flow rates ($0.5 \mu l/min$) to observe how it may influence the membrane formation process. As discussed earlier, at low flow rates a good control over the flow and a balanced pressure was observed. However, we found that the zipping of the leaflets was unsuccessful at this low flow rate and we observed immediate coalescence of the approaching interfaces. This suggests that the operating flow rate of the current platform should be high enough so that the membranes are formed robustly, but at the same time low enough so that the balancers do not fail (a range between 1- $2.5 \mu l/min$ is suggested).

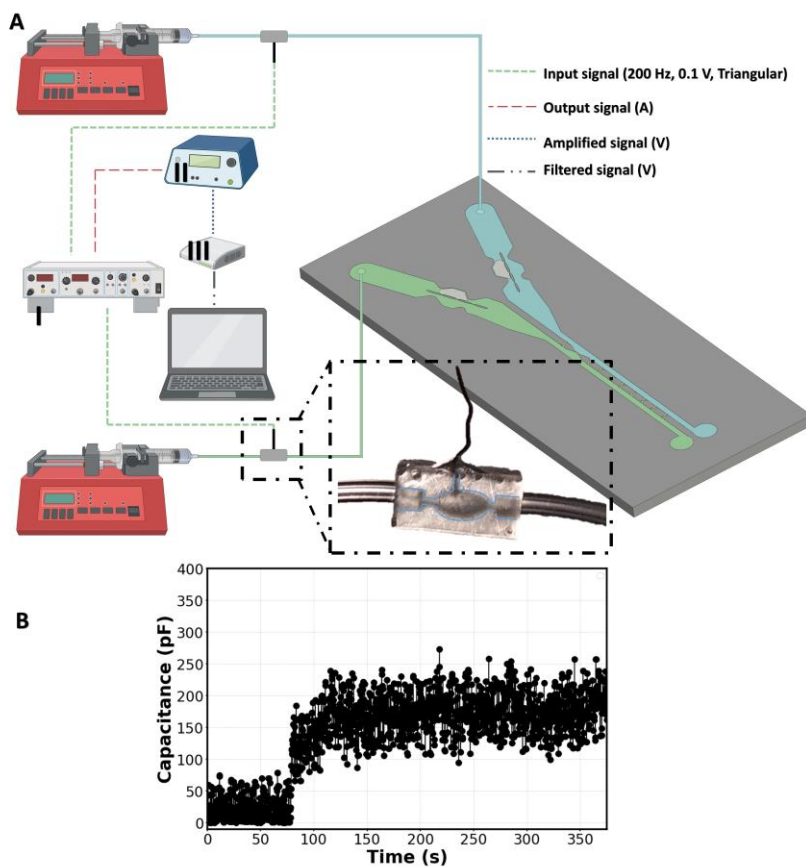


Figure 4.4: A) Schematic of the setup for on-chip electrophysiology measurements. As indicated in the inset indicated by the dashed box, the electrode is not directly inserted in the microchannels, but instead, a 3D-printed T-connector (framed in dashed lines) is used in the tubing. B) Example of lipid bilayer capacitance measured during membrane formation and stabilization (two more examples are plotted in Supplementary Figure S 4.1.). The signal was gathered throughout the process, starting when the green and blue parallel streams were pumped into the chip to form the membrane and continuing for several minutes afterward while the flow was maintained.

4.5 Conclusion

We introduced a new single-gap microfluidic chip integrated with bidirectional fluidic diodes capable of maintaining a balanced, controlled pressure at the gap for the formation of vertical, freestanding lipid bilayers. The presented microfluidic chip enables different sorts of experiments, such as transmembrane recordings and mechanical/hydrodynamic characterizations. This device can also be used for the formation of asymmetric membranes or membranes with asymmetric aqueous media, since the leaflets and their corresponding media are independently controllable. We showed the performance of the fluidic diodes experimentally. We also demonstrated that this chip enables electrophysiological tests on lipid bilayers in a straightforward manner. The designed fluidic diodes can also be implemented in other microfluidic chips for other applications requiring precise pressure balancing at interfaces like free-standing liquid films studies ¹²⁴.

4.6 Materials and Methods

4.6.1 Master mold fabrication

The master mold was created in a cleanroom environment using standard fabrication techniques. First, a positive photoresist (S1813) was spin-coated onto a 4-inch silicon wafer, achieving an approximate thickness of 3 μm . The chip design, initially drawn in AutoCAD, was converted into a dxf file using Klayout. A laser writer (μMLA , Heidelberg Instruments) was used to transfer the design onto the spin-coated wafer (with an exposure intensity of 300 mJ and a defocus setting of 6 μm , using pneumatic focusing).

The exposed pattern was then developed in MF322 solution for 80 seconds and rinsed thoroughly with deionized water. The mask was dried through centrifugation. Next, the developed mask underwent plasma descumming (100 Watts for 5 minutes), followed by etching using a PlasmaPro 100 Estrelas DRIE (Oxford Instruments) system, achieving a channel depth of approximately 75 μm (measured with stylus profilometer, Bruker). The etching process utilized the conventional Bosch method for silicon etching. To remove any residual photoresist, the mold was sonicated in Ar600-71 for 5 minutes and rinsed with isopropanol before being dried with nitrogen gas. Finally, plasma cleaning was performed (600 Watts for 5 minutes), and the mold underwent vapor deposition of Silane (tri-chloro (1H,1H,2H,2H-perfluorooctyl, Sigma-Aldrich) in a vacuum chamber overnight.

4.6.2 Minor mold fabrication

First, PDMS and its curing agent (SYLGARD®) were thoroughly mixed at a ratio of 10:1. The mixture was then degassed in a standard desiccator to remove any trapped air bubbles. Following this, PDMS was cast onto the master mold (silicon) and subjected to another round of degassing. The cast PDMS was then cured in an oven at 85°C for a duration of 8 hours. Subsequently, PDMS was carefully diced out from the master mold.

4.6.3 Microfluidic chip fabrication

NOA81 from Norland Products was cast onto the PDMS mold, creating the foundation for subsequent chip fabrication steps. A glass slide was carefully placed on the liquid NOA, allowing it to settle and form a uniform layer beneath the slide, which was then exposed

to UV light for 5 minutes using a Promed UVL-36 equipped with four UV-9W-L bulbs. Following UV exposure, the PDMS was delicately peeled off, revealing the intricately designed channels on the cured NOA. Ports were drilled into the chip with 1mm drilling tips. A clean coverslip was then spin-coated with NOA81 and partially cured for 1 minute before being bonded to the channels, forming a seamless seal. The assembled chip underwent an additional 10-minute UV exposure to solidify the bonding. Finally, the chip was baked at 85°C on a hot plate for 8 hours, ensuring thorough curing and structural integrity for subsequent applications.

4.6.4 Lipids and buffers

1-palmitoyl-2-oleoyl-glycero-3-phosphocholine (POPC) was purchased from Avanti in chloroform (25 mg/ml). To form membranes, two identical syringe pumps (ProSense NE-30) were used at the following flow rates: 1) Initially a $9 \mu\text{l}/\text{min}$ rate to bring the HEPES/chloroform interface to the balancing system. This is necessary to increase the speed of the whole process, mitigating the overall time chloroform is present in the channels. 2) Then it is important to reduce the flowrate to $2.5 \mu\text{l}/\text{min}$ until the interfaces pass the balancing part. 3) To zip leaflets, the rate is maintained at $2.5 \mu\text{l}/\text{min}$ until the chloroform is pushed far enough from the membrane to leave the system via outlets. To prepare the aqueous phase, a solution of 10 mM 4-(2-hydroxyethyl)-1-piperazineethanesulfonic acid (HEPES) was adjusted to a pH of 7.4 using concentrated

KOH. Following this, 150 mM KCl and 0.5 mg/ml bovine serum albumin (BSA) were added to the mixture. The final buffer solution was then filtered through a 0.2 μm sterile filter.

4.6.5 Electricals

To demonstrate that the chip is applicable for transmembrane recordings, i.e., electrophysiology, we utilized the capacitance-to-period conversion method^{22, 145} to measure the capacitance of the formed membranes on the chip at the flow rate of 2.5 $\mu\text{l}/\text{min}$. To prepare Ag/Cl electrodes, silver wires (0.5 mm diameter, Thermo-Scientific) were first cleaned with sand paper and then immersed in bleach solution (Dik Bleek) until they were completely black, indicating that the surface was coated with AgCl. Then the wires were washed with de-ionized water and inserted and sealed in the T-connectors. The inlet of each T-connector was fed with the tube connected to the syringe pump and the outlet was connected to the tube attached to the chip inlet. A triangular input signal (200 Hz, 0.1 V peak-to-peak) was generated with a signal generator (BK precision 4040A 20 MHz). A DLPCA 200 (Femto) was used for amplification and current–voltage conversion. Then, the signal was filtered through a 5 kHz low-pass filter. Data acquisition was done by a DAQ USB-6009 (National Instrument) at a 20 kHz rate. All computation was done directly from the signal with a custom-made LabVIEW program.

4.7 Supplementary information

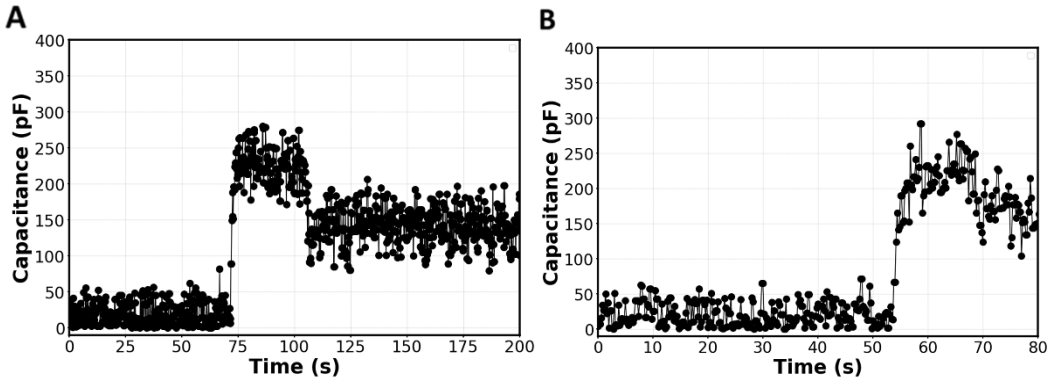


Figure S 4.1: A &B) Two other examples of membrane capacitance at the membrane formation phase. The high region plateau after the formation moment in (A) is due to the membrane being bent at the beginning due to pressure imbalances (a bent membrane would have a larger surface area and so a higher capacitance). But after 100 s, pressure stabilizes and the membrane equilibrated at the gap (not bent any more so the total surface area is lowered and so the capacitance). The noise in the signal can be reduced via performing the experiment in a vibration-free condition, using pumps with smooth step motors, and preventing any electromagnetic interferences with the measurement setup.

Section 2

Chapter 5

Mechanical characterization of freestanding lipid bilayers with temperature-controlled phase

Abstract:

Coexistence of lipid domains in cell membranes is associated with vital biological processes. Here, we investigate artificial *in vitro* membranes with two different compositions, i.e., a multi-component membrane composed of DOPC and DPPC lipids with gel and fluid separated domains, and a single component membrane composed of PMPC lipids forming ripples. We characterize their mechanical properties below their melting point, where ordered and disordered regions coexist, and above their melting point, where they are in a fluid phase. To conduct these inquiries, we create lipid bilayers in a microfluidic chip interfaced with a heating system and optical tweezers. The chip features a bubble trap and enables high-throughput formation of planar bilayers. Optical tweezers experiments reveal interfacial hydrodynamics (fluid-slip) and elastic properties (membrane tension and bending rigidity) at various temperatures. For PMPC bilayers, we demonstrate a higher fluid slip at the interface in the fluid-phase compared to the ripple phase, while for the DOPC:DPPC mixture, similar fluid slip is measured below and above the transition point. Membrane tension for both compositions increases after thermal fluidization.

Bending rigidity is also measured using the forces required to extend a lipid nanotube pushed out of the freestanding membranes and we found that bending rigidity for both lipid compositions is not temperature sensitive within the measured temperature range. This novel temperature-controlled microfluidic platform opens numerous possibilities for thermomechanical studies on freestanding planar membranes.

Part of this chapter contains published material from: Yahyazadeh Shourabi, Arash, et al. "Mechanical characterization of freestanding lipid bilayers with temperature-controlled phase." *Soft Matter* 20.42 (2024): 8524-8537.

5.1 Introduction

In both eukaryotic and prokaryotic plasma membranes, coexistence of ordered and disordered regions within the lipid bilayer impacts the membranes' properties and plays a role in several biological processes, such as protein transport, signal transduction, and the entry of viruses into cells¹⁴⁶⁻¹⁴⁸. Coexistence of lipid regions in the membrane depends on lipid composition and it can appear in the form of gel domains emergence in lipid mixtures, or ripple-state conformation in single component membranes¹⁴⁹⁻¹⁵⁰. In particular, binary lipid mixtures containing 1,2-dioleoyl-sn-glycero-3-phosphocholine (DOPC) and 1,2-dipalmitoyl-sn-glycero-3-phosphocholine (DPPC) promote phase separation resulting in the presence of in-plane gel phase and fluid phase domains. Coexistence of gel and fluid regions presents as patches enriched in highly-ordered saturated lipids with relatively high melting temperature (T_m), e.g. DPPC ($T_m = 41$ °C), which exist alongside fluid-phase lipid domains with lower melting temperature, e.g. DOPC ($T_m = -17$ °C)¹⁴⁹. Such DOPC:DPPC containing mixtures are often used as models for biological cell membranes¹⁵¹⁻¹⁵².

The ripple phase is another manifestation of ordered-disordered coexisting lipid regions^{27, 150}, more recently described as the coexistence of an ordered phase and a complex mixed phase¹⁵³. The ripple phase can occur in single lipid composition bilayers just below the T_m , i.e. in between a pre-transition temperature (T_{pre}) and T_m , and has been reported for both supported²⁷ and un-supported lipid bilayers¹⁵⁴⁻¹⁵⁵. Unlike the gel-fluid

separation in a DOPC-DPPC binary mixture, the ripple-state membrane presents a structure with corrugations with a periodicity of $\sim 10\text{-}30\text{ nm}$ ^{150, 156}, and long-range orientation correlation of its hexagonal lattice packed domains ¹⁵⁷. For instance, palmitoyl-myristoyl-PC (PMPC, 16:0-14:0 PC, $T_m = 27\text{ }^\circ\text{C}$, $T_{pre} = 17\text{ }^\circ\text{C}$) is a mixed-chain (sn-1 and sn-2 acyl chains of different lengths ¹⁵⁸) lipid that forms a ripple structure below its T_m ³. Although PMPC is abundant in the mammalian pulmonary system and is involved in COVID-19 infection prevention ¹⁵⁹, it is scarcely characterized mechanically especially below the T_m .

It has been shown that membranes with coexisting ordered-disordered regions exhibit complex thermomechanical properties different from what is observed in single-phase ones ¹⁶⁰. Yet, the overall literature on the contribution of such lipid domains to the bilayers' mechanical properties is still limited ¹⁶¹⁻¹⁶⁴. Such studies are needed because many biological functions depend on the mechanical properties of the membrane ¹⁶⁵⁻¹⁶⁷ determined by the spatial phase heterogeneity of bilayers ^{164, 168}. The hydrodynamics at the interface (interfacial fluid slip) and elastic properties (membrane tension and bending rigidity) are two subgroups of such mechanical properties, which influence numerous biological processes ¹⁶⁹⁻¹⁷⁰. Interfacial fluid slip is an indicator of the bilayer response to the surrounding flow ²⁰. *In vivo*, this response is dependent on the bilayer composition and its associated physical properties ¹⁷⁰ and influences a broad range of biological processes such as ion channel gating, signaling, molecular transport, protein activation,

and cell-drug interaction^{62-63, 171-173}. On the other hand, membrane tension influences cell polarity^{37, 174}, membrane fusion³⁶, and trafficking⁴⁰, while bending rigidity influences cell growth rate and division³⁵. Membrane tension and bending rigidity together also define geometrical and physical properties of lipid nanotubes (LNTs), which are structures also present in cells for molecular transport and intercellular communication¹⁷⁵.

Measuring the mechanical characteristics of a membrane *in vitro*, while altering the phase of the bilayer represents a technical challenge. Two conventional *in vitro* settings for the study of membrane properties are vesicles and supported bilayers. These systems present limitations for measurements of mechanical and phase-related properties¹⁷⁶⁻¹⁷⁷. In vesicles, controlling membrane curvature can be challenging and usually requires specific custom technology¹⁷⁸⁻¹⁷⁹. Membrane curvature is known to impact lipid ordering and to interfere with phase separation, and more specifically may shift the pre-transition temperature at which the ripple structure occurs^{154, 180}. In supported bilayers, the contact between one leaflet and the solid substrate impacts their phase behavior²⁵; this results in a strong dependency of the bilayer phase and the related mechanical properties on the substrate topography²⁶. For example, substrate contact was reported to affect ripple phase formation in supported bilayers²⁴.

The use of planar freestanding membranes formed in microchannels represents a reliable alternative for phase-related studies, as they have minimal curvature and do not contact

a surface. This configuration has been used for measurements of room-temperature mechanical properties of single-phase bilayers^{20-21, 108}, but phase-associated mechanical studies using this approach have not been reported. To enable this, an improved microfluidic system is required, to provide precise and controlled heating, while preventing thermal-related instabilities leading to the loss of the membrane, including: membrane instability below the melting point⁸³, and the management of air bubbles in microchannels for thermal experiments⁸¹. Additionally, the design should robustly handle the often low success rate of membrane formation in microchannels with non-fluid lipid compositions^{29, 83}, aiming for high-throughput and comprehensive characterization in each experiment. It should be noted that in all these artificial systems (freestanding bilayers, vesicles, supported bilayers), the membrane is at equilibrium, as opposed to cell membranes *in vivo*¹⁸¹.

Here, we study the thermomechanical properties of lipid membranes in a freestanding, planar configuration. We utilized the microfluidics setups discussed in Chapter 2 for this goal. Two distinct lipid bilayer compositions are used in this study: the gel-fluid domain-forming DOPC:DPPC (3:2 molar ratio) lipid mixture, and the ripple phase-forming PMPC lipid. For both compositions, phase change takes place approximately at the same temperature ($T_m \approx 27$ °C¹⁹). The chip is mounted on an optical tweezer setup with a coiled objective to heat it, inducing temperature-driven phase changes in the membranes. We study the temperature-related elastic properties (membrane tension and bending

rigidity) and interfacial hydrodynamics (fluid slip) for temperatures below and above their melting points (i.e. between 21 °C and 32 °C). We first perform a study on how the fluid-slip at the interface depends on the temperature of the bilayer by shearing the membranes with the optically trapped bead. Then, beads are pushed against these bilayers bidirectionally to extract biologically relevant mechanical properties, namely surface tension, membrane-to-tube and tube-to-membrane transition force-barriers, and bending rigidity at the aforementioned temperatures.

Other well-established techniques, such as cDICE¹⁸²⁻¹⁸³ and eDICE¹⁸⁴, also rely on the contact of two monolayers at an organic-aqueous interface for membrane formation. These techniques are increasingly used to synthesize GUVs that model minimal cells¹⁸⁴⁻¹⁸⁵. The present piece of work also relies on the contact of two monolayers for membrane formation and can be utilized as a side tool for better understanding the membranes formed in this way.

5.2 Hydrodynamics at the interface of membranes

We start characterizing our lipid membranes by investigating the hydrodynamics at their interface (fluid slip). Our group has previously shown that the fluid slip at the interface of freestanding planar membranes depends on lipid composition and lies in between a full-slip (equivalent to no wall) and a no-slip (solid wall) boundary condition²⁰. Here, we compare the flow behavior at the interface of gel-fluid and ripple membranes at 21 °C and show how fluidizing them by increasing the temperature to 32 °C affects fluid slip.

For this purpose, we use PMPC and DOPC:DPPC (3:2) bilayers, which were both reported to experience a phase transition at 27 °C¹⁸⁶⁻¹⁸⁷. It should be noted that T_m may deviate slightly depending on the solvent used, the membrane configuration, and the interactions between the membranes and the platform on which they are formed. For instance, freestanding planar DOPC:DPPC (3:2) membranes formed in microchannels by contacting monolayers followed by subsequent drainage of the solvent, showed a T_m that deviates ~ 0.4 °C on average (toward larger values) from the T_m observed on giant unilamellar vesicles (GUVs)¹⁹. We therefore do not rule out the possibility that our method of membrane formation and the presence of residual solvent may influence phase separation or shift slightly the transition point. For this reason, we probed a range of several degrees around 27 °C, i.e. from 21 °C to 32 °C. Also, one indication that we likely cross T_m is that when heating from 21°C to 32°C, membrane buds were occasionally observed ([Supplementary Figure S 5.1](#)), as reported for lipid vesicles when going through a phase transition¹⁸⁸. Note that our mechanical testing was not performed in the vicinity of such buds, but only on flat membranes.

We optically trap a polystyrene bead of diameter $2a=2$ μm at a specific distance d between the center of the bead and the freestanding lipid bilayer. The membrane is then moved parallel to its plane with the use of a piezo stage (inset of [Figure 5.1 A](#)). The drag force experienced by the bead (D) is measured with the optical trap and is normalized with the Stokes' drag ($F_D = 6\pi\mu Ua$, where μ is the dynamic viscosity, U is the bead's

velocity relative to the membrane). We call this force ratio C_δ and use it to describe the fluid slip at the interface of the aqueous medium with the membrane as previously described²⁰. C_δ can be described as follows:

$$C_\delta = \frac{D}{6\pi\mu Ua} \approx \left[1 - \frac{9}{16} \frac{a}{d+l_s}\right]^{-1} \quad (1)$$

where l_s defines the slip length. If the bilayers were to behave like a solid wall, the model would coincide with Faxén's law¹⁸⁹ corresponding to $l_s = 0$ in equation 1. When using equation 1 to calculate the slip length at the interface of the bilayers, we assume that the bilayers are non-deformable boundaries for the flow. Significant local deformations of lipid bilayers have been reported for traveling beads with larger diameters (3-8 μm)¹⁹⁰. To check for membrane deformations, we tracked DOPC:DPPC (3:2) membranes with a high-speed camera while a 2 μm optically trapped bead was translated at velocities U between 5 - 100 $\mu\text{m}/\text{s}$ in the plane of the membrane. This experiment was repeated with a distance d varying from 1.1 μm to 11.1 μm between the bead's center and the bilayer. Video analysis showed that no significant membrane deformation was obtained at any value of U or d tested (Supplementary [Figure S 5.2](#)).

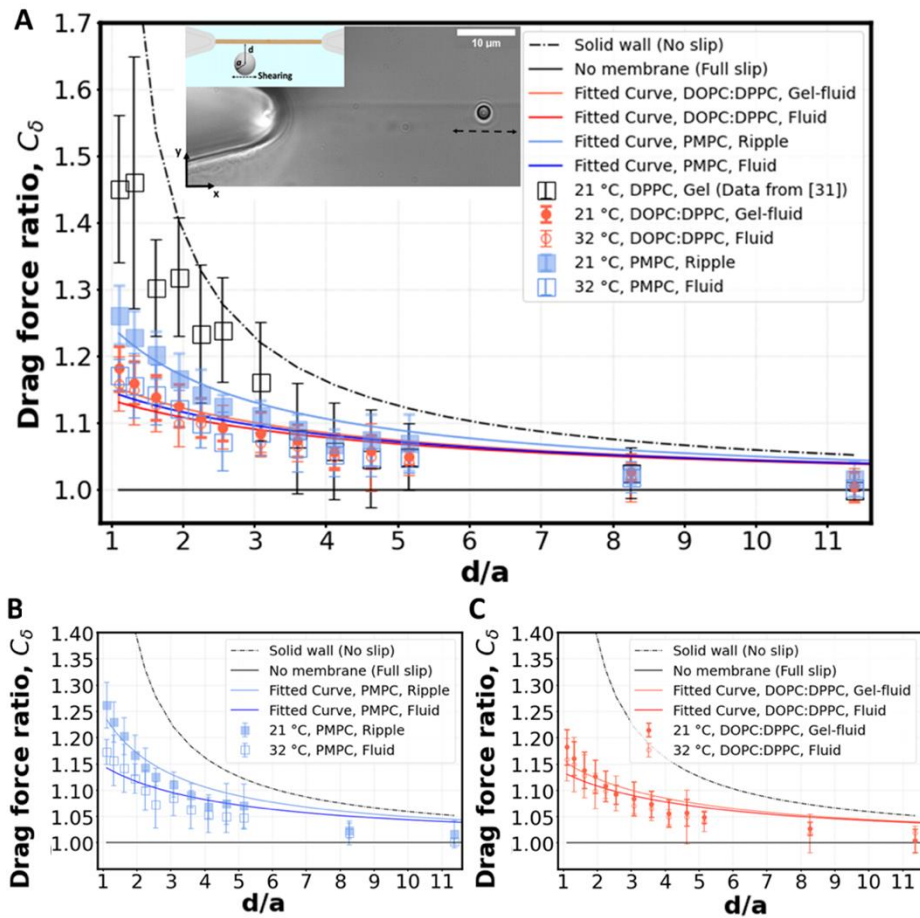


Figure 5.1: Shearing experiment. A) An optically trapped bead of radius a is used to shear lipid membranes of different compositions (see legends) at various distances d (as shown in inset). The graph shows the ratio of the experimentally measured drag force on a bead of diameter $2a=2\ \mu\text{m}$ to the Stokes' force at different bead-membrane distances d . Fitted curve of equation 1 is also plotted on the experimental data. R^2 values are 0.84, 0.80, 0.91, 0.78 for gel-fluid DOPC:DPPC, fluid DOPC:DPPC, ripple PMPC, and fluid PMPC, respectively. The dashed line represents the no-slip condition ($l_s = 0$) that happens at the

boundary of a solid wall based on Faxén's law¹⁸⁹. The solid line represents what we would expect for a free gap (no membrane), where full slip ($l_s = \infty$) happens. For the lipid membranes tested, the behaviour lies between a solid wall and a free gap (no membrane) condition depending on composition and temperature as indicated with red and blue data points. B and C) Drag ratio of PMPC and DOPC:DPPC (same data as (A), plotted separately for better visualization).

For our membranes, C_δ was deduced from our experimental measurements at varying distances d/a from the bilayer (Figure 5.1). For the rippled-phase PMPC membrane at 21 °C, we measure $C_\delta = 1.26 \pm 0.05$ at a distance $d = 1.1 \mu m$ between the bead's center and the bilayer, resulting in a fitted slip length $l_s = 1.9a$, higher than the previously reported value²⁰ for DPPC (16:0 PC) bilayers ($C_\delta = 1.46 \pm 0.15$ at $d = 1.1 \mu m$, and $l_s = 0.83a$) at 21 °C. Therefore, we find that the mixed-chain PMPC (16:0 14:0 PC) lipid allows for higher fluid slippage compared to its symmetric-chain counterpart DPPC (16:0 PC). When increasing the temperature to 32 °C, PMPC bilayers transition to the fluid phase and we find a significant reduction in the drag ratio at 32 °C ($C_\delta = 1.18 \pm 0.03$ at $d = 1.1 \mu m$, $l_s = 3.4a$). Our observation of a decrease in the drag force experienced by the bead at the interface upon heating is consistent with previous reports on the decrease of drag force experienced by a bead attached to a DMPC giant vesicle transitioning from the ripple to the liquid-disordered phase¹⁹¹. We performed the same experiment with DOPC:DPPC (3:2) membranes. Unlike PMPC, we find drag ratios that are not significantly

different below and above T_m , i.e. $C_\delta = 1.18 \pm 0.03$ ($l_s = 3.2a$) at 21 °C and $C_\delta = 1.16 \pm 0.04$ ($l_s = 3.8a$) at 32 °C.

The values measured for C_δ at intermediate temperatures between 21 °C and 32 °C are also provided in [supplementary Figure S5.3](#) for both lipid compositions. We observe a continuous decrease of C_δ with temperature for PMPC. For DOPC:DPPC, the drag ratio remains almost constant at all the temperatures. Similarly, previous FRAP experiments on DOPC:DPPC (1:1) lipid bilayers showed no correlation of lipid diffusion coefficient with temperature when the temperature was increased from 22 °C to 38 °C¹¹.

When comparing PMPC and DOPC:DPPC bilayers, we find that both bilayers exhibit a behavior at the water interface which is far from a solid boundary (no-slip), with ripple-phase PMPC showing a lower slip-length at the interface in comparison to the two-phase DOPC:DPPC membrane. We attribute this lower drag ratio obtained for the two-phase DOPC:DPPC membranes to the presence of kinks in the unsaturated lipid DOPC.

The interfacial drag ratios enable us to estimate membrane viscosity (η_b in $Pa.s.m$) and its variation with temperature. For this purpose, we assume an intermonolayer friction coefficient b in the range of $0.3 \times 10^3 \leq b \leq 1.7 \times 10^3 Pa.s.m^{-1}$ ²⁰ (which was reported experimentally for DOPC:DPPC (2:1) bilayers using a similar microfluidic setup). With the methodology provided by Amador *et. al.*²⁰ we estimate a membrane viscosity of $3.4 \times 10^{-9} Pa.s.m \leq \eta_b \leq 9.8 \times 10^{-9} Pa.s.m$ for PMPC at 21 °C, $1.3 \times 10^{-9} Pa.s.m \leq$

$\eta_b \leq 5.5 \times 10^{-9} Pa.s.m$ for PMPC at 32 °C, $1.0 \times 10^{-9} Pa.s.m \leq \eta_b \leq 5.6 \times 10^{-9} Pa.s.m$ for DOPC:DPPC at 21 °C, and $0.46 \times 10^{-9} Pa.s.m \leq \eta_b \leq 5.1 \times 10^{-9} Pa.s.m$ for DOPC:DPPC 32 °C. For comparison, a membrane viscosity of 3 nPa.s.m was reported for SOPC (18:0 18:1 PC) GUVs measured using falling ball viscometry¹⁹², 13 nPa.s.m for SOPC GUVs measured using a probe diffusion method¹⁹³, and 0.15 nPa.s.m for DOPC LUVs measured via the fluorescence lifetime of a dye¹⁹⁴.

5.3 Surface tension and bending rigidity of membranes

We proceed by performing measurements of membrane tension (σ) and bending rigidity (κ) on bilayers at temperatures between and including 21 °C and 32 °C. To this end, we used the optical trap to push a 2 μm bead against a planar, freestanding bilayer. The force-displacement curve of the trapped bead provides a direct measurement of the surface tension and the subsequent calculation of the tube radius and bending rigidity²¹. First, the bead is pushed 'forward' and enters in contact with the membrane, the force increases as the membrane deforms and gradually wraps around the bead (panel I of [Figure 5.2 A](#) corresponding to the linear region of the solid lines in [Figure 5.2 B](#)). After reaching a maximum force, the force drops abruptly, corresponding to the complete wrapping of the membrane around the bead and the formation of a lipid nanotube ([Figure 5.2 A](#), panel II). The lipid nanotube can then be extended at constant force while the bead is moved further away from the freestanding bilayer. After being displaced to a distance of 9 μm from the lipid bilayer, the direction of motion of the optical trap relative to the

bilayer is reversed and the bead moves 'backward' towards the lipid bilayer (the dashed lines in [Figure 5.2 B](#)). The lipid tube first retracts, and eventually disappears, resulting in an abrupt increase of the measured force. At this stage, the bilayer is partially wrapped around the bead. As the bead continues to move backward, the force decreases linearly with the same slope as for the forward motion ([Figure 5.2 B,C](#)) until the force goes back to zero when the bead is fully released from the membrane.

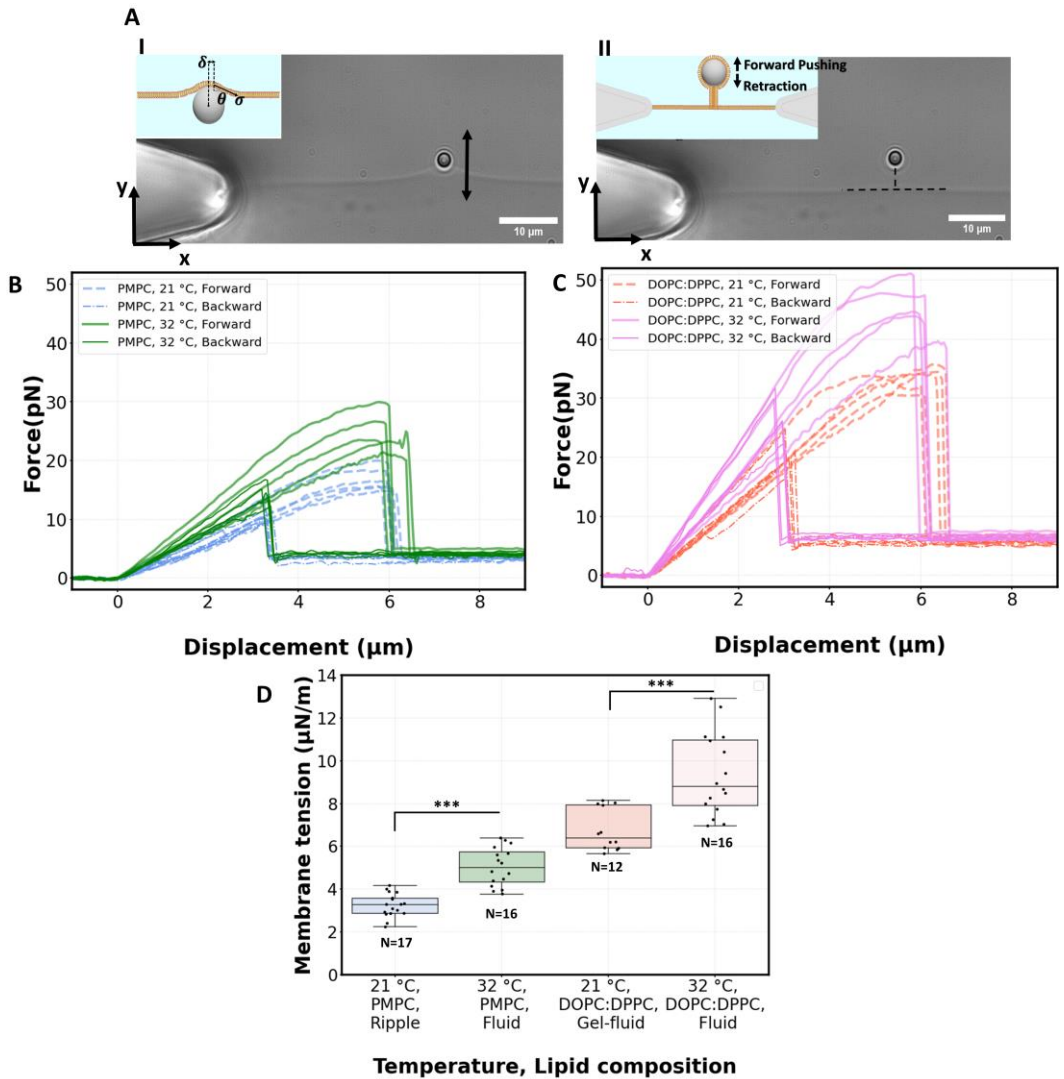


Figure 5.2: Pushing experiment. A) Procedure of pushing bilayers (in forward and backward motion) with an optically trapped bead. B-C) Force displacement curves for a 2 μm optically trapped bead pushing forward against a membrane, or backward (retraction), for PMPC (B) and DOPC:DPPC(3:2) (C) membranes at 21 $^{\circ}\text{C}$ and 32 $^{\circ}\text{C}$. D) Membrane tension measured at 21 $^{\circ}\text{C}$ and 32 $^{\circ}\text{C}$ for PMPC and DOPC:DPPC(3:2) membranes. P-

values on the graphs are represented via * for $p < 0.05$, ** for $p < 0.01$ and *** for $p < 0.001$ calculated with Kruskal-Wallis one-way statistical analysis.

5.3.1 Membrane tension

The membrane tension (σ) is directly extracted from the force-displacement curves and the membrane deformations (Figure 5.2 B,C), by using the following force balance on a bead pushing the membrane ²¹ (Supplementary Figure S 5.4):

$$\sigma = \frac{F}{2\pi\delta \cos\theta} \quad (2)$$

where δ is the distance from the bead centre at which the angle θ of the membrane is measured, and F is the force applied by the optical trap which is derived from the linear region of the force-displacement curves. A custom-made image-processing code was developed to track the bead position and membrane geometry while the membrane is being pushed, to extract θ (inset of panel I of Figure 5.2 A, and Supplementary Figure S5.4).

For PMPC, we find membrane tensions of $3.3 \pm 0.6 \mu\text{N/m}$ and $5.04 \pm 0.9 \mu\text{N/m}$, at 21 °C and 32 °C, respectively. For the binary DOPC:DPPC (3:2) mixture, we find the tensions to be $6.75 \pm 1 \mu\text{N/m}$ and $9.35 \pm 1.9 \mu\text{N/m}$, at 21 °C and 32 °C, respectively. The membrane tensions at temperatures in between 21 °C and 32 °C are presented in Supplementary Figure S 5.3. For both lipid compositions, a significant increase in tension takes place when heating membranes over 27 °C.

The values of tension that we obtained are similar to tensions measured *via* laser-induced surface deformation for other planar, freestanding membranes composed of PC/PE lipid mixtures (i.e. 1.3 to 68.1 $\mu\text{N}/\text{m}$ for bilayers with cholesterol molar fractions varying from 0 to 33%)⁴⁶.

As a control, we did the same experiment on 16:0 18:1 PC (POPC, $T_m = -2^\circ\text{C}$) bilayers. The measured membrane tensions ($5.93 \pm 2.07 \mu\text{N}/\text{m}$ at 21°C) show good temperature stability in the range from 21°C to 32°C , where POPC is expected to remain in the fluid phase (Supplementary Figure 5.5 A). When comparing PMPC, DOPC:DPPC, and POPC, the measured surface tension is the lowest for the mixed-chain lipid PMPC.

It should be noted that the tension depends on several factors including the experimental platform, the lipid composition, the interactions of the lipid monolayers/bilayers with the surface of the chip, and the diffusion of lipids from the annulus into the membrane to compensate for the increase in surface area caused by pushing the membrane. Although tension is not an intrinsic property of a membrane, calculating it remains important for two key reasons. First, there is a current interest in obtaining membrane tension values in freestanding planar bilayers¹⁹⁵, in particular for protein-embedded membrane experiments¹⁹⁶. Second, it serves as an essential intermediate step in determining the bending rigidity when using the lipid tube (or tether) pulling approach.

5.3.2 Lipid nanotube formation

The force-barrier to form lipid nanotubes is biologically relevant as it is also experienced by motor proteins that mechanically exert force on the membrane to form LNTs¹⁹⁷. The force required for membrane-to-tube and tube-to-membrane transition is shown in [Figure 5.3 A,B](#). For both PMPC and DOPC:DPPC mixture, the force barrier increases on average after fluidization (at high temperature) in both the forward and backward (retraction) motion. The force barrier, at both temperatures and pushing directions, is lower for PMPC than for the DOPC:DPPC mixture as bilayers made up of PMPC possess a lower surface tension. The amount of pushing force required for a $2\ \mu\text{m}$ bead to push out a nanotube through a PMPC membrane increases from $17.4 \pm 1.9\ \text{pN}$ to $26.8 \pm 4.1\ \text{pN}$ when the membrane is heated from $21\ ^\circ\text{C}$ to $32\ ^\circ\text{C}$. For the DOPC:DPPC mixture, it increases from $34.4 \pm 2.8\ \text{pN}$ to $47.7 \pm 6.9\ \text{pN}$. In each single experiment, the force barrier in backward (retraction) motion is smaller than the forward motion from an hysteresis effect accompanying the transition of the membrane to the tube⁴⁸.

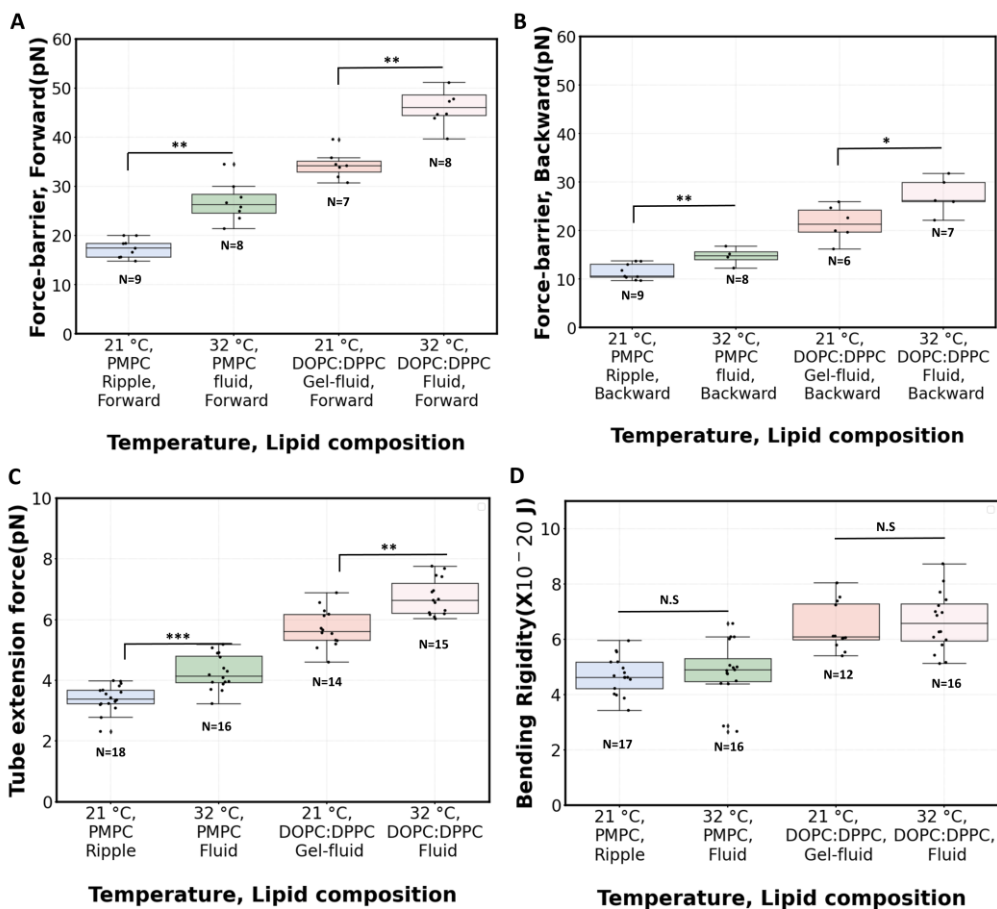


Figure 5.3: Tube pulling experiment. Overshoot (force-barrier) of the A) membrane-to-tube and B) tube-to-membrane transition for either PMPC or DOPC:DPPC mixtures, at 21°C and 32°C. C) Force applied with the optical tweezers to extend the tube for either PMPC or DOPC:DPPC mixtures, at 21°C and 32°C. D) Bending rigidity below and above the transition temperature. Note that for the phase-separated DOPC:DPPC mixture at 21°C, the values are possibly measured for one of two phases, if the lipids close to the tube junction are of one specific phase. P-values on the graphs are represented via * for $p < 0.05$, ** for $p < 0.01$ and *** for $p < 0.001$ calculated with Kruskal-Wallis one-way statistical analysis.

Figure 5.3 C shows the measured tube extension forces (F_t). For PMPC, the average tube extension force (forward and backward) increased by about 25% when going from ripple phase to the fluid phase. For the binary mixture, this increase is about 18% after fluidization. The magnitude of tube extension forces that we obtained is similar to the values reported when pushing optically trapped beads on planar DOPC:DPPC membranes (3.8 pN)²¹ or on DOPC:DOPG vesicles (5.7 pN)⁴⁷.

The radius of the lipid nanotubes (R_t) pushed out of membranes at both temperatures can be deduced from the measured membrane tension and tube extension force *via* the formula $R_t = \frac{F_t}{4\pi\sigma}$ ¹⁹⁸. Tube radii were previously reported to be in the range of 10-100 nm when tubes were pulled from DOPC or DOPC:DPPC bilayers with either optical tweezers^{21, 48}, an atomic force microscope¹⁹⁹ or by the action of actomyosin filaments²⁰⁰. For PMPC membranes, the formed nanotube was calculated to have a radius of 84 ± 9 nm in ripple phase and a smaller radius of 70 ± 12 nm in the fluid phase. For the binary mixture, we calculated the radius to be 71 ± 4 nm in its two-phase state and 60 ± 8 nm in the single fluid phase. In summary, for both membrane compositions, we measured a decrease in the LNT average radius in the fluid phase compared to their phase below the melting point.

5.3.3 Bending rigidity

Next, we estimate the bending rigidity (κ) of the bilayers with a tether pulling approach, by using both the measurements of membrane tension and tube extension force, using equation (4):

$$\kappa = \frac{F_t^2}{8\pi^2\sigma} \quad (4)$$

The bending rigidities for both lipid compositions at both temperatures are reported in [Figure 5.3 D](#). Our value of κ measured from DOPC:DPPC bilayer ($6.4 \pm 0.9 \times 10^{-20}\text{J}$) is similar to that measured on oriented stacks of DOPC bilayers with X-ray scattering method, i.e., $7.3 \times 10^{-20}\text{J}$ ²⁰¹. For PMPC, we find a κ value of $4.7 \pm 0.7 \times 10^{-20}\text{J}$, which is in the range previously reported for DPPC and DMPC when measured experimentally utilizing flicker noise spectroscopy ²⁰².

Interestingly, the measured values of bending rigidities remain constant in the range between 21 °C to 32 °C ([Supplementary Figures S5.3](#)). Previous work has reported a lowering of κ when lipid bilayers transition from gel to liquid phase ^{23, 191, 203}. In our experiments with PMPC, we probe the transition from ripple to fluid phase (as opposed to gel to fluid), which possibly explain our temperature-stable values of κ , also consistent with a previous observation that the decrease in κ appears to be sharper around T_{pre} than T_m ²³. Also, PMPC is a saturated mixed-chain lipid, and molecular dynamics simulations have shown less variation of κ around T_m for a mixed-chain lipid compared to its

symmetric-chain counterpart²⁰⁴. Interestingly, a sizeable fraction of PC lipids constituting biological membranes are saturated mixed-chain lipids²⁰⁵⁻²⁰⁶, just like PMPC; and they are shown to provide temperature stability to membranes^{9, 207}.

In addition to the tether pulling approach²⁰⁸, several other methods have been used to measure bending stiffness (e.g. fluctuation spectroscopy, optical dynamometry) using different assumptions and leading to different values for the measured κ . An inherent limitation of the tether pulling approach is that the phase and composition of the lipid bilayer is uncertain at the junction between the flat membrane and the newly formed tube. In PMPC bilayers, ripples possibly do not form in the vicinity of the tube. As for the phase-separated DOPC:DPPC mixture (below T_m), the area where the tube is being pulled from the freestanding membrane is possibly always in a specific phase due to lipid sorting^{49, 209}, and therefore the bending rigidity value calculated below T_m could represent only one specific phase within the phase-separated DOPC:DPPC bilayer.

5.4 Conclusion

We used optical tweezers to investigate the mechanical properties of two types of planar, vertical, freestanding, membranes with coexisting ordered-disordered lipid regions: (i) domain-forming DOPC:DPPC and (ii) ripple PMPC. For this purpose, we used the thermally controlled microchip of chapter 2 that enables robust and highly reproducible bilayer

formation in a high-throughput manner due to its integration with a bubble trapping system and its fluidic design.

Utilizing optical tweezers on the chip, we characterized how the fluid slip at the interface of ripple PMPC lipid bilayers increases after they undergo a fluid transition. Additionally, we showed that the mixed-chain counterpart of DPPC, i.e. PMPC, possesses a higher degree of fluid slip. We also studied the force barrier for membrane-to-nanotube and nanotube-to-membrane transition in freestanding planar bilayers. We showed in both membrane compositions, that the membrane-to-tube force barrier is higher in the fluid phase compared to the phase below the melting point. Further, we demonstrate that for both lipid compositions, the membrane tension increases upon heating.

PMPC membranes show a temperature stable rigidity, while being mechanically more flexible (lower tension and rigidity) and also less susceptible to oxidations due their saturated structure²¹⁰, making them good candidates for various drug-carrier applications

²¹⁰⁻²¹².

The novel tools developed here are well suited for the systematic mechanical characterization of diverse lipid compositions during a phase transition, which could elucidate other uncharted aspects of cell membrane biophysics.

5.5 Methods and Experimental

5.5.1 Thermal chip and temperature control

Details of the chip fabrication and the integrated heating system are discussed in Chapter 2. For thermal stabilization, the chip was kept at each test temperature for 120 minutes and then the optical tweezers experiments were started. We set the heat flux at $0.3\text{ }^{\circ}\text{C}/\text{min}$ when assigning any specific temperatures to the membrane.

5.5.2 Lipids and membrane formation

1,2-dioleoyl-sn-glycero-3-phosphocholine (DOPC), 1,2-dipalmitoyl-sn-glycero-3-phosphocholine (DPPC), and palmitoyl-myristoyl-PC (PMPC) in chloroform (10 mg/ml) and 1-palmitoyl-2-oleoyl-glycero-3-phosphocholine (POPC) in chloroform (25 mg/ml) were all purchased from Avanti (Sigma-Aldrich), stored at $-20\text{ }^{\circ}\text{C}$, and used directly without further purification. For the mixture, a 3:2 molar ratio of DOPC:DPPC was prepared at 10 mg/ml . To prepare the aqueous phase, a 10 mM 4-(2-hydroxyethyl)-1-piperazineethanesulfonic acid (HEPES) solution was adjusted to pH 7.4 with concentrated KOH, and KCl (150 mM) and bovine serum albumin (BSA, 0.5 mg/ml) were added, and the aqueous buffer was filtered with a $0.2\text{ }\mu\text{m}$ sterile filter. Afterwards, $2\text{ }\mu\text{m}$ beads (real diameter = $1.93\text{ }\mu\text{m}$, Polysciences Inc.) were diluted 25000 times in the aqueous buffer. A ProSense NE-30 syringe pump was used to infuse the flow into the chip. To do so, a syringe connected to tubing is filled with the buffer and mounted on the syringe pump. Using another syringe, lipid containing chloroform is injected at the tip of the tube, which is later connected to the chip inlet. Immediately after the membrane formation, the interface

appeared optically as a thick dark-bright film. In the first few minutes, the solvent was absorbed rapidly until only a thin, nearly invisible interface remains. While membranes were formed, the pump was running at high-flow rates ($5\mu\text{l}/\text{min}$) until all the chloroform has been pushed out of the chip. During this time, the membranes were vibrating slightly due to the instabilities caused by the pulsatile nature of the syringe pump's flow. After the chloroform had been pushed out completely, the pump was stopped. Experiments were conducted on membranes between 2 to 8 hours old.

5.5.3 Optical tweezers experiments

The optical tweezers (OT) methods for both the shearing and pushing experiments are described previously²⁰⁻²¹. All experiments were performed at $30\mu\text{m}$ above the surface of the flow cell. For the shearing experiment, the traveling distance was $25\mu\text{m}$ with a rate of $100\mu\text{m}/\text{s}$. A 1.2 NA water immersion objective (FI Plan Apo VC 60x, Nikon) was used to optically trap a bead inside microchannels mounted on a piezostage (NANO-LPS100, Mad City Labs) with a 1064 nm trapping laser (YLR-10-LP-Y12, IPG Laser) and a 830 nm detection laser (LDT830-30GC, TOPAG). Anti-aliasing filtering and pre-amplification (10 dB) was performed with a KROHN-HITE 3364 on the voltage signals from a position sensitive detector (PSD, DL100-7-PCBA3, First Sensor). In the pushing experiment, fine positioning of the bead relative to the membrane was controlled with the piezo stage. The stage was moved sequentially in steps from $0.03\mu\text{m}$ to $0.08\mu\text{m}$, and at each position, the data collection was done in a quasi-static manner by recording the PSD signal during

0.5 second, at a sampling rate of 1 kHz with a cut-off frequency of 500 Hz. For setup calibration, trap stiffness calculation, bubble trap quantification (flow measurement through the gap), and shearing experiments, signals were sampled at 50 kHz with a cut-off frequency of 24.5 kHz. All the signals from the PSD were processed and converted to nm and pN with a custom-made python code.

5.5.4 Image processing for surface tension measurements

To track the membrane and the bead, a CMOS camera (DCC1545M, Thorlabs GmbH) with 11.5 px/ μm resolution was used to record videos of pushing experiments at 14 fps. Videos were converted to tiff format, cropped, and filtered with a FFT band pass filter for contrast enhancement in ImageJ. Modified tiff files were then analysed with a custom Matlab script to obtain the deformation angle (Figure S5.4). To track membrane deformation while being sheared, a high-speed sCMOS camera (LaVision PCO.edge, 75 fps) was used.

5.5.5 Statistical analysis

Results shown on Figures 5.1, 5.2, and 5.3 were obtained from experiments repeated on at least 4 membranes from at least 3 different chips. For each experiment, a new bead was trapped. A Kruskal-Wallis one-way statistical analysis was executed, utilizing a significance criterion of $p = 0.05$ to ascertain significance. Calculated P-values are tabulated in the supporting information (Tables S5.1-S5.2 of Supplementary). P-values on the graphs are represented via * for $p < 0.05$, ** for $p < 0.01$ and *** for $p < 0.001$. Error bars in all figures represent the standard deviation of the data. In the box plots in all

figures, the box shows the quartiles, the horizontal line is the median, and the whiskers are extending to the most extreme data points.

5.6 Supplementary information

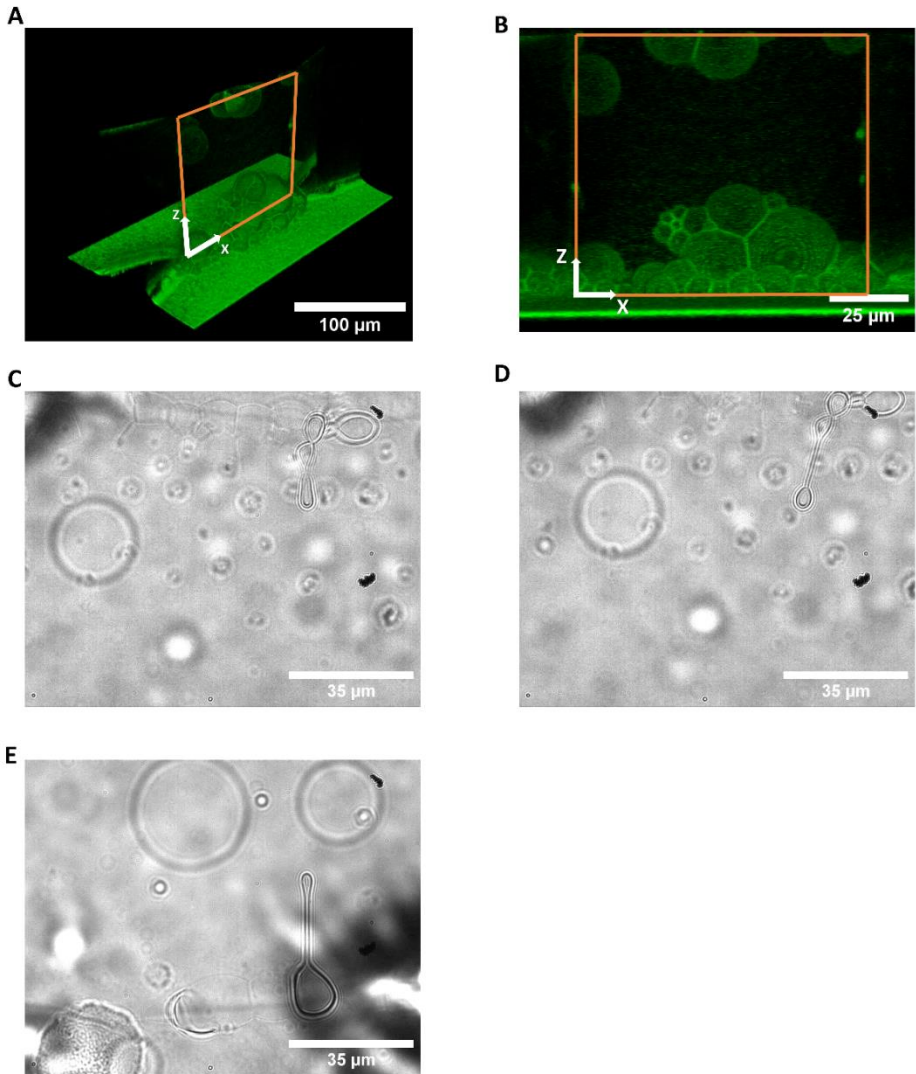


Figure S5.1: Pearl-shaped structures budding from membranes upon heating. A-B) Confocal fluorescent image of budding in DOPC:DPPC at 32 °C. In this image, the bottom surface coated with lipids is visible. A front view of the membrane at the gap is observable with the buds coming out from the membranes upon heating. For the confocal fluorescent imaging, 1% V/V of 1,2-dioleoyl-*sn*-glycero-3-phosphoethanolamine-*N*-(carboxyfluorescein) (18:1 PE CF) was mixed with the DOPC:DPPC mixture. Z-stack images were collected in 0.4 μm steps (Z axis is considered along the vertical edge of the gap edge). Imaging is performed using a Nikon AIR confocal microscope. A 3D reconstruction is then created from the image stack using ImageJ. All images are taken at 32 °C. C-E) Budding in PMPC bilayers. D-E) It is possible to pull the buds with the optical tweezers and make a long stable nanotube from these structures.

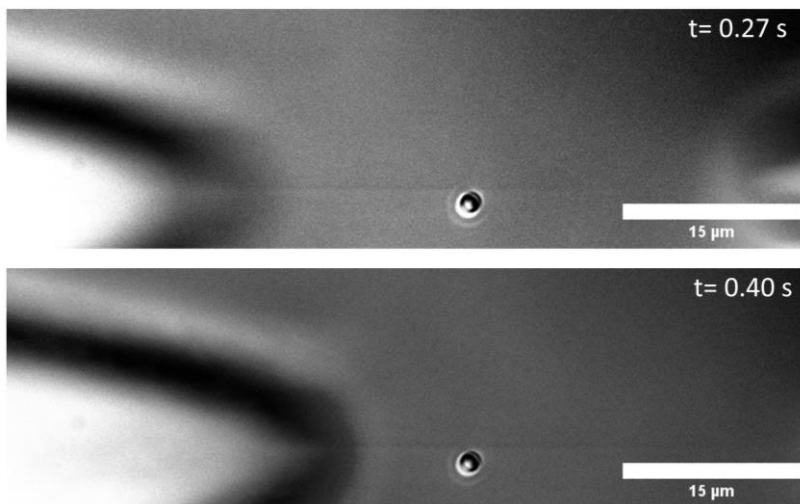


Figure S5.2: High-speed tracking of membrane shearing. High-speed tracking of a DOPC:DPPC (3:2) membrane while being sheared by an optically trapped bead at 100 $\mu\text{m}/\text{s}$ at a distance of

1.1 μm between the bead's center and the bilayer. The images show two snapshots taken at $t=0.27$ s and $t=0.40$ s after shearing is started.

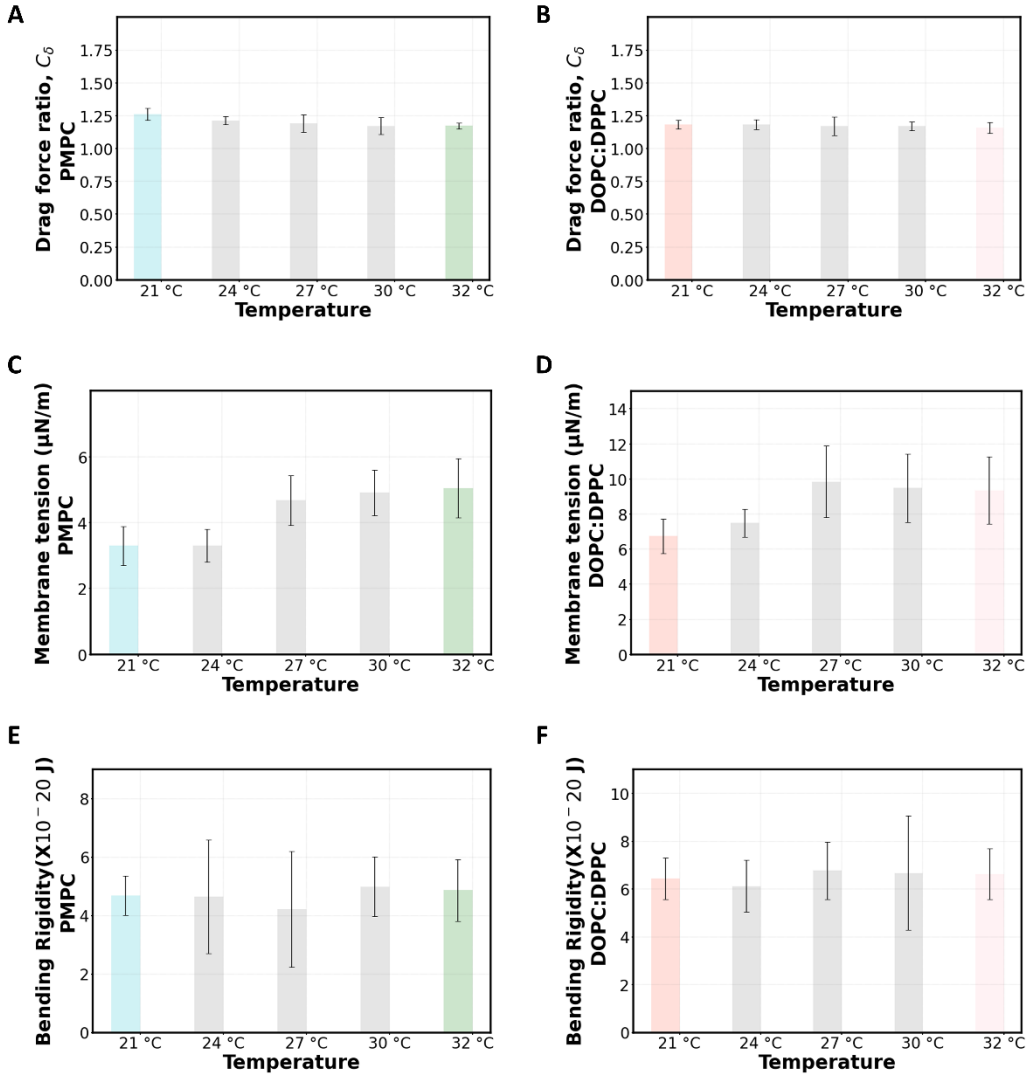


Figure S5.3: Values of the interfacial drag coefficient (A and B), membrane tension (C and D), and bending rigidity (E and F) for PMPC and DOPC:DPPC at temperatures between 21 °C and

32 °C. For the middle temperatures (24 °C, 27 °C, 30 °C), 3 separate membranes were used in the measurements. Note that for the phase-separated DOPC:DPPC mixture (at 21°C and 24°C), the values are possibly measured for one of two phases, if the lipids close to the tube junction are of one specific phase.

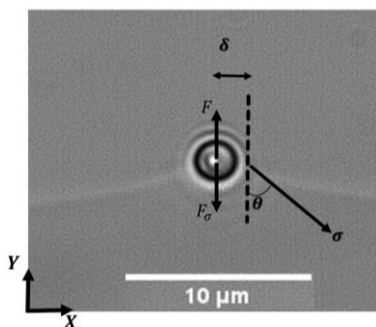


Figure S5.4: The procedure to calculate the membrane tension. The angle of the force vector is measured via image processing using a custom-made Matlab program. The custom script performs the following steps for each frame: First, it determines the bead's center coordinates (via finding the edge of the bead through its intensity value, fitting a circle to it, and finding the center of the fitted circle). Next, it identifies the coordinates of the maximum intensity positions along the membrane on the right side of the bead. A third-order polynomial is fitted to these membrane coordinates, enabling us to achieve subpixel resolution and calculate the angle between the deformed membrane and its original position, 32 pixels horizontally away from the bead's center. The angles obtained are then averaged over at least 28 frames, and used to calculate the surface tensions when the piezo stage was moved 2 and 4 μm from its original position.

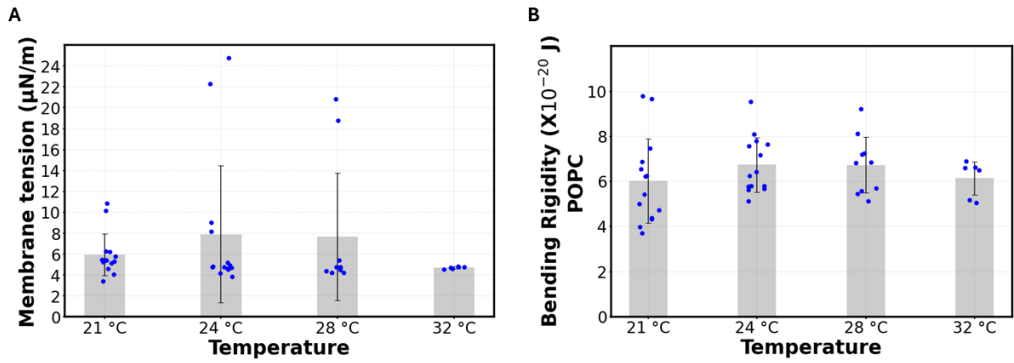


Figure S5.5: Mechanical characterization of POPC bilayers. A) Membrane tension. B) Bending rigidity. Number of datapoints: 14, 14, 10, and 6 for 21°C, 24 °C, 28 °C, and 32 °C, respectively.

Table S5.1: Kruskal-Wallis p-values for detecting the significance effect of temperature on the hydrodynamics at the interface at each distance from the membrane. This corresponds to the data presented in Figure 3B.

d/a	DOPC:DPPC, Kruskal-Wallis p-value	PMPC, Kruskal-Wallis p-value
1.1	0.223	0.0009
1.31	0.34	0.02
1.62	0.31	0.03
1.93	0.1	0.02
2.24	0.26	0.05
2.55	0.44	0.05

3.07	0.22	0.11
3.59	0.29	0.12
4.63	0.31	0.21
5.15	0.18	0.23
8.25	0.31	0.19
11.36	0.12	0.45

Table S5.2: Kruskal-Wallis p-values for detecting the significance effect of temperature on the mechanical properties. This corresponds to the data presented in Figures 4 and 5.

Parameter	Kruskal-Wallis p-value
Tube Extension Force, DOPC:DPPC	0.0005
Tube Extension Force, PMPC	0.0001
Force-barrier, Forward, DOPC:DPPC	0.001
Force-barrier, Backward, DOPC:DPPC	0.01
Force-barrier, Forward, PMPC	0.003
Force-barrier, Backward, PMPC	0.003
Membrane Tension, DOPC:DPPC	0.0004
Membrane Tension, PMPC	0.00001
Tube radius, PMPC	0.03
Tube radius, DOPC:DPPC	0.02
Bending Rigidity, DOPC:DPPC	0.64
Bending Rigidity, PMPC	0.37

Chapter 6

Effect of lipid tail-asymmetry and cholesterol on the mechanical properties of lipid bilayers

Abstract

Cell membranes are composed of phospholipids consisting of hydrophilic head groups and hydrophobic tails. The molecular arrangement of the hydrocarbon tail is a key parameter defining membrane properties. Tail-asymmetry is one such arrangement that manifests in two possible forms of asymmetry in length (in saturated mixed-chain lipids) and of asymmetry in degree of saturation (in hybrid lipids) between sn-1 and sn-2. While previous works have primarily focused on the correlation of tail-asymmetry with thermodynamic characteristics, here we systematically study the mechanical properties of tail-asymmetric bilayers alongside their corresponding tail-symmetric counterparts, specifically 1,2-dipentadecanoyl-sn-glycero-3-phosphocholine (PC15) and 1,2-dioleoyl-sn-glycero-3-phosphocholine (DOPC), respectively. Our measurements show that freestanding vertical planar bilayers of saturated mixed-chain compositions formed inside microchannels exhibit fluidic behavior with low tension and bending rigidity, even when

below their melting point, unlike the solid structure of tail-symmetric PC15 bilayers. Moreover, we find that while hybrid counterparts of DOPC show a similar interfacial fluid slippage and bending rigidity, they show a reduced membrane tension. Additionally, we observed that tail-asymmetry may alleviate the effect of cholesterol on interfacial fluid slip (which can be reducing or increasing the slip length depending on the lipid composition). Our findings highlight the influence of lipid tail structure and cholesterol on vertical planar lipid bilayers in microchannels. We also suggest using saturated mixed-chain phosphocholine for applications requiring membrane fluidity, flexibility, and oxidation resistance.

6.1 Introduction

Cell membranes, primarily composed of phospholipids, are the fundamental barriers separating cellular compartments from the external environment.¹ In the realm of eukaryotic cell membranes, two types of asymmetry underlie their structure: first, the asymmetry in the lipid composition of the inner and the outer leaflet, and second, the asymmetry in the hydrocarbon tail structure within individual lipid molecules.^{7, 213} The latter aspect is the focal point of our investigation here. Previous studies have highlighted the prevalence of asymmetric lipid hydrocarbon chain structures in biological cell membranes,¹⁵⁸ such as in *S. japonicas* where approximately 60% of lipids were found to be chain(tail)-asymmetric phosphatidylcholines.²¹⁴⁻²¹⁵ Tail-asymmetric lipids, in contrast to tail-symmetric ones, have received comparatively less attention in current literature. Specifically, limited knowledge is available regarding the impact of saturated tail-asymmetric lipids on membrane mechanics and biophysics.^{4, 213} What is known is that dissimilarity in the length or saturation of hydrocarbon tails at the sn-1 and sn-2 positions influences intrabilayer lipid molecule interactions^{31, 204, 216} and phospholipid-cholesterol interplay^{8, 210}, resulting in potentially distinct mechanical features.^{3-4, 210, 217-218}

Tail-asymmetric lipids can be divided into two subgroups based on their saturation characteristics. The first subgroup pertains to saturated lipids, where tail asymmetry stems from variations in chain lengths (called saturated mixed-chain lipids)²¹⁹. Physical properties of saturated mixed-chain lipids are dependent on how mismatched tails are

accommodated into the bilayer, i.e., how the two leaflets are zipped together. Two leading models are proposed for the accommodation of the unequally sized chains into the membrane: an interdigitating structure where the longer tail penetrates partly into the opposing leaflet⁹ and a folding structure where the longer tail fold back towards its own leaflet¹⁰. Regardless of the means for accommodation of unequal chains, length-mismatch is believed to make the membrane mechanically softer in comparison to bilayers formed from analogous tail-symmetric lipids.²²⁰

The second subgroup of tail-asymmetric lipids concerns hybrid lipids, featuring a saturated tail at the sn-1 position and a tail containing unsaturated cis-double bonds at the sn-2 position.^{32, 163, 221} While the unsaturated tail influences membrane properties, it is not the exclusive determinant; the position of the unsaturated bonds along the hydrocarbon chain and the degree of unsaturation also contribute to altering the magnitude of these effects.²²²⁻²²³ Biologically speaking, many lipids in cell membranes exhibit a hybrid configuration while their function is not fully discovered yet.^{1, 224} From a physics point of view, it is known that the degree of interdigitation in hybrid lipids is not significant even under high pressures,²²⁵ and that these lipids reduce line tension and regulate domain size in multi-component membranes.^{32, 226}

The objective of this study is to explore how tail asymmetry affects the properties of bilayers in a freestanding planar configuration. Although freestanding lipid membranes

are becoming more widespread,^{6, 20-21, 28, 102, 195} not all the details regarding these membranes are well-explored, and delving into the composition-dependent mechanics of such membranes is important.¹⁹⁵ The focus here is to examine the influence of membrane composition and more specifically lipid tail-asymmetry, in both saturated mixed-chain and hybrid structures, on the bulk mechanical characteristics of phospholipid membranes. The effect of cholesterol on these membranes is also investigated. To this goal, a microfluidic method is implemented and optical tweezers are used to mechanically probe the lipid bilayers (Figure 6.1). Single-component bilayers of various lipid compositions (Figure 6.2) are formed and tested on-chip to better distinguish the unique features of each individual lipid. As for lipid compositions selection, we maintained a consistent phosphatidylcholine (PC) head while systematically altering the length and saturation of sn-1/sn-2 positions throughout our experiments. The PC lipid family is exceedingly prevalent in the plasma membrane and subcellular organelles of mammalian cells.²²⁷ Our measurements encompass membrane tension, bending rigidity, and interfacial fluid slip (with/without cholesterol), providing a multifaceted perspective on the mechanical behavior of the membranes. For the saturated group, 1,2-dipentadecanoyl-sn-glycero-3-phosphocholine (called here PC15) (15:0 15:0 PC) and its mixed-chain category counterparts, i.e. PMPC (16:0 14:0 PC) and MPPC (14:0 16:0 PC), were chosen. For the unsaturated group, we used di-monosaturated tail-symmetric DOPC (18:1 18:1 PC), its monosaturated counterpart SOPC (18:0 18:1 PC), and the tail-asymmetric POPC (16:0 18:1

PC) and PLPC (16:0 18:2 PC). Our lipid composition selection covers several possible states of length/saturation mismatch in phospholipids. This systematic assessment of mechanical properties of various lipid compositions can help with designing artificial model cell membranes with specific properties.

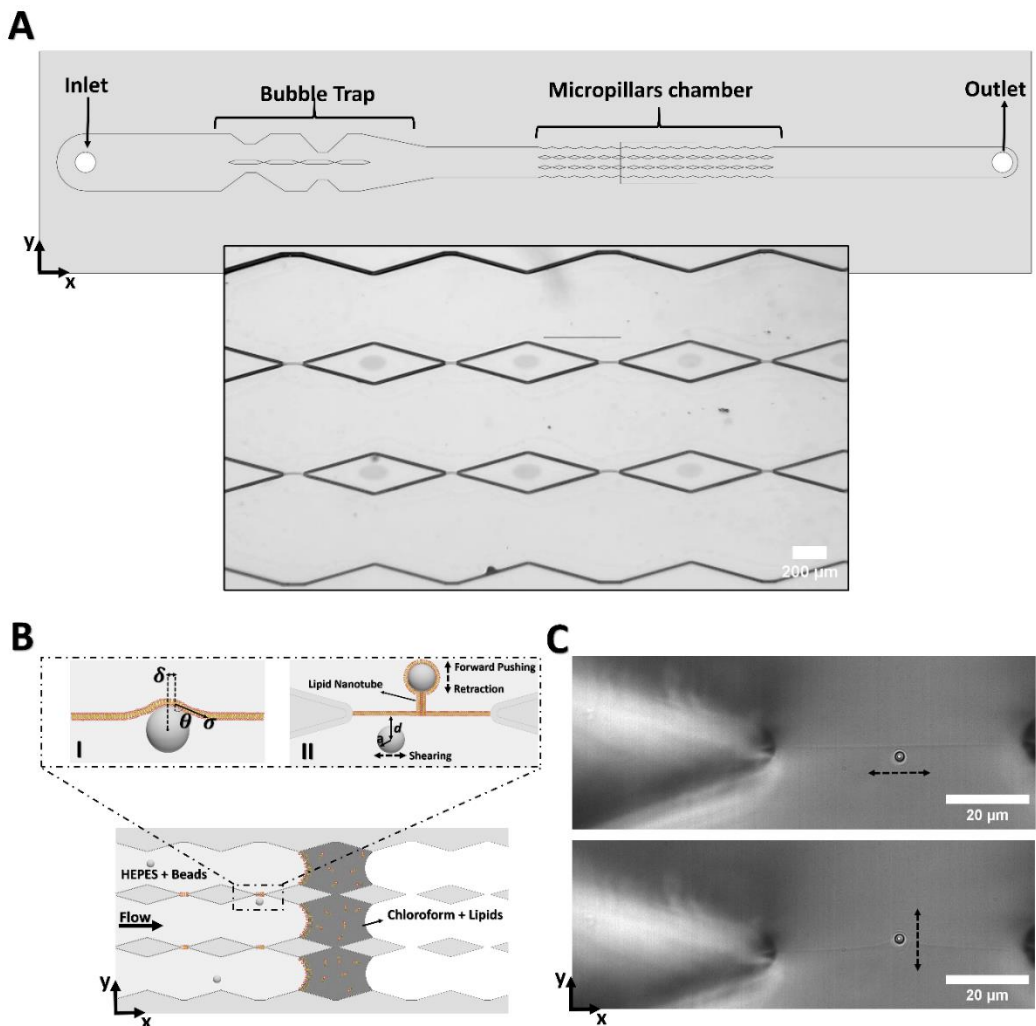


Figure 6.1: Top view illustration of the microfluidic chip's layout, process of membrane formation, and membrane characterization. A) Diagram showing distinct sections of the microfluidic chip, including the bubble trap chamber and the micropillar region. B) Lipid monolayer interfaces, fractionated into three segments by two rows of micropillars, coalesce pairwise at the gaps to form planar bilayers. Inset (I): Deformation of the membrane when a bead is pushed against it.

Geometrical parameters (δ and θ) are later used in the calculation of membrane tension. Inset (II): Bi-directional pushing of the membrane using the trapped bead until lipid nanotubes are formed, for elastic measurements. Also, shearing the membrane with an optically trapped bead of radius a at distance d from the membrane. C) Pictures from shearing (top) and pushing (bottom) experiments. The black vertical arrow in panel B shows the direction of the flow, while the dashed arrows in panel C is the direction of the bead - membrane relative movement.

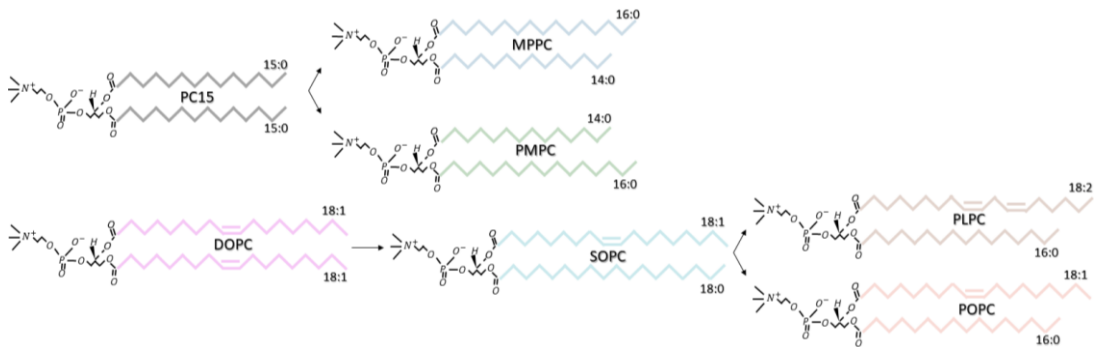


Figure 6.2: Lipids investigated in this study. A range of saturated mixed-chain lipids (MPPC and PMPC) and hybrid lipids (SOPC, PLPC and POPC), differing in both chain length and saturation, are studied along with their tail-symmetric counterparts (PC15 and DOPC).

6.2 Combining optical tweezers and microfluidics

High-throughput formation of lipid bilayers on NOA81 microchips and interfacing them with optical tweezers was shown to enable membrane mechanics studies.^{20-21, 102} We followed the same approach here to form freestanding, planar lipid bilayers on an integrated microfluidic chip developed previously¹¹⁴ and discussed in chapter 2. The chip

encompasses a bubble trap that enhances membrane stability by removing unwanted bubbles from the flow, coupled with an array of micropillars designed for increased throughput (Figure 6.1 A). This microfluidic architecture facilitates the efficient and rapid creation of freestanding, single-component bilayers with varying compositions, ensuring their resilience and stability without the need for any sterols or stabilizers. Freestanding lipid bilayers present advantages over supported lipid bilayers, as they do not interact with a support that risks to affect membrane mechanics.²²⁸ Lipid compositions used in this study vary in tail structure and asymmetry (Figure 6.2).

The on-chip process of bilayer formation follows four stages: 1) the chip is mounted and fixed on piezo-stage of an optical tweezer setup, 2) lipid molecules dissolved in chloroform are flown into the chip with a syringe pump, followed by the bead-laden aqueous phase (HEPES), 3) bubbles are captured at the bubble trap to provide the system with a bubble-free flow¹⁰², 4) the two leaflets (lipid monolayer interfaces) join and zip at the gaps to form membranes. After membranes are formed, the trapping laser was used to trap a $2\mu\text{m}$ polystyrene bead near the membranes to measure mechanical (tension, bending rigidity, and interfacial fluid slip) properties of the membrane. To measure interfacial fluid slip, the trapped bead and the membrane are displaced relative to each other in a direction parallel to the membrane's length at a known velocity to characterize the hydrodynamics at the interface (Figure 6.1 B-C). To do the elastic characterization

(tension, bending rigidity), the piezo stage is translated in a direction perpendicular to the membrane so the bead is pushed against the membrane (Figure 6.1 B-C).

6.3 Mechanics of bilayers of lipid molecules varying in tail-asymmetry

We first investigated the membrane mechanical properties by pushing a $2\mu\text{m}$ optically trapped bead against a freestanding bilayer. We were unable to deform PC15 bilayers when pushing with the optical tweezers. All other lipid compositions tested (Figures 6.2 and 6.3 A) followed the classic force-displacement behavior observed when pushing optically trapped beads against lipid vesicles.⁴⁷

As shown in Figure 6.3 A, when the bead is pushed against the membrane, the force first increased with an approximately linear upward slope as the membrane deformed. Eventually, the force reached a peak, signifying the force-barrier to form the nanotube, followed by an abrupt decrease in the force when the membrane completely wrapped around the bead and a lipid nanotube was formed. The subsequent section shows a plateau, wherein a constant force was required to extend the nanotube. Afterwards, the bead was moved in the opposite direction (back towards to freestanding bilayer) and the tube retracted until it vanished, marked by a sudden force increase. Finally, the force decreased, displaying a linear pattern akin to the observed trend during the initial stages of the forward pushing, until the beads was fully released from the membrane and the force goes to zero.

6.3.1 Membrane tension

Membrane tension was calculated from the force-displacement curves using equation (1), which is a simple force balance on the bead while it is being pushed against the membrane:^{21, 102}

$$\sigma = F/2\pi\delta \cos\theta$$

(1)

In this quasi-static situation, the force acting upon the bead from the membrane that resist its deformation is equal to the force applied by the optical trap. In equation (1), δ is the distance from the center of the bead where the angle θ (inset of [Figure 6.3 B](#)) is measured, and F is the force exerted by the optical trap. The measured tensions are presented in [Figure 6.3 B](#). Membranes with the mixed-chain compositions (PMPC and MPPC) were easily deformable in contrast to their tail-symmetric counterpart, PC15, which could not be deformed in our setup. PMPC and MPPC possess tension values of $3.52 \pm 0.56 \mu\text{N}/\text{m}$ and $4.17 \pm 0.75 \mu\text{N}/\text{m}$, respectively, which is lower compared to the unsaturated compositions ([Figure 6.3 B](#)).

Comparing the membrane tension of DOPC ($\sigma_{DOPC} = 15.82 \pm 4.75 \mu\text{N}/\text{m}$) with its hybrid variations, we discover intriguing findings. [Figure 6.3 B](#) shows that among the studied unsaturated group, hybrid counterparts display notably diminished membrane tension. Specifically, POPC shows the lowest tension amongst all unsaturated compositions

($\sigma_{POPC} = 5.87 \pm 1.14 \mu\text{N}/\text{m}$). The two other hybrid compositions other than POPC, namely PLPC ($\sigma_{PLPC} = 9.57 \pm 4.03 \mu\text{N}/\text{m}$) and SOPC ($\sigma_{SOPC} = 8.32 \pm 3.21 \mu\text{N}/\text{m}$), both generate higher tension values compared to POPC.

It should be noted that the membrane tension depends not only on the nature of the lipids, but also on how the freestanding bilayer interacts with the platform on which it is formed and on the effectiveness of the lipid reservoir in compensating for the area increase while pushing.²²⁹

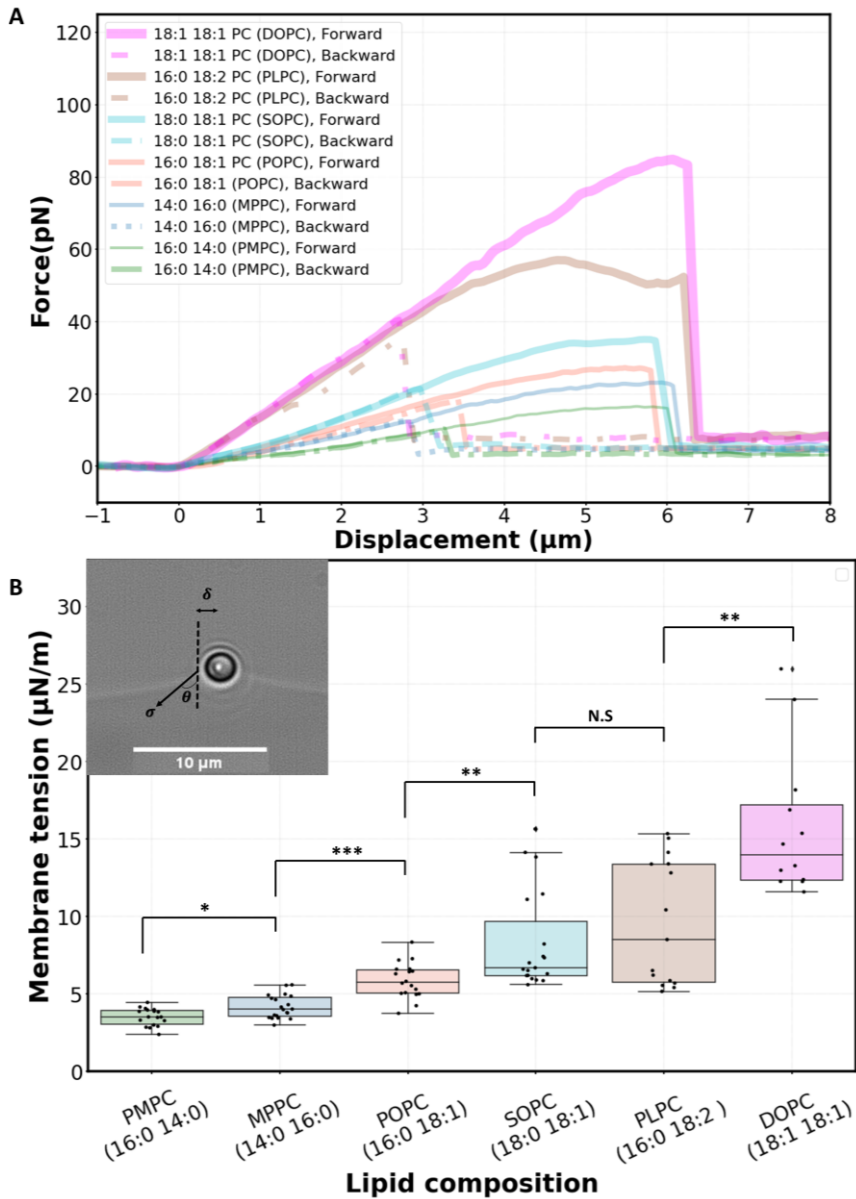


Figure 6.3: Pushing experiment. A) Force-displacement curves for pushing forward and backward (retraction) of membranes of different compositions. Not all data is shown but only one sample curve for each composition to avoid overpopulating the figure. B) Values calculated for membrane tension.

6.3.2 Bead entry into tail-asymmetric bilayers

As previously stated, when we continue pushing the bead against the membrane, a maximum force level (force-barrier) is reached and a nanotube is formed. This process is relevant to various applications such as virus entry, drug delivery, and the assessment of toxicity related to microparticle pollutants where particles enter and become enveloped by cell membranes.²²⁹⁻²³³

Results for the force-barrier of membranes with different lipid compositions being pushed against the trapped $2\mu\text{m}$ bead show that the force required for the membrane-to-tube transition (tube formation upon forward pushing) is greater than that for tube-to-membrane transition (tube retraction upon backward pushing) (Figures 6.4 A-B). This hysteresis effect⁴⁸ was previously observed on both planar¹⁰² and vesicle⁴⁷ configurations. More into details, Figure 6.4 A illustrates that in stark contrast to PC15, which exhibits no tendency to wrap, PMPC and MPPC both display a diminished force-barrier. Among all studied compositions, DOPC registers the highest force barrier while PMPC registers the lowest. POPC demonstrates the smallest force-barrier within the realm of unsaturated lipids. Regarding the retraction force-barrier, PMPC once again exhibits the lowest force, while DOPC possesses the highest. SOPC and PLPC behave somewhere between DOPC and POPC in both the forward and retraction experiments. The outcomes highlight a potential distinction within the realm of lipids studied in this Chapter: membranes characterized by tail-asymmetry exhibit substantially lower force-

barriers for particle entry/release compared to their tail-symmetric analogues. This finding can specifically be crucial in designing drug-delivery systems²³⁴⁻²³⁵ and characterizing spontaneous microparticle wrapping within membranes in the absence of binding agents.^{229, 236}

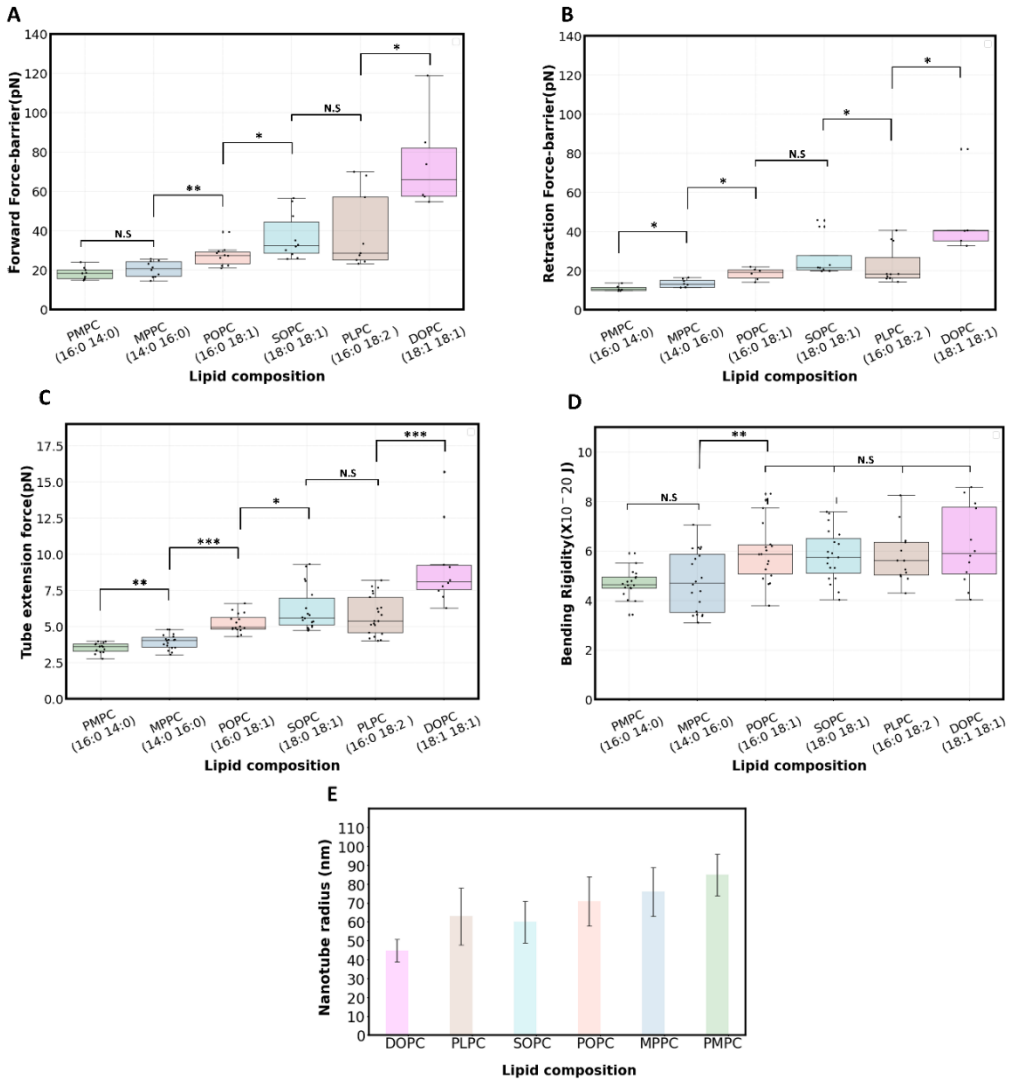


Figure 6.4: Results for tube formation and membrane rigidity. A & B) Force barrier values for forward pushing (membrane-to-tube transition) and retraction (tube-to-membrane) experiments. C) Values of tube extension force. D) Calculated bending rigidity values for membranes of different compositions. E) Calculated nanotube radius values.

6.3.3 Bending rigidity of tail-asymmetric lipid bilayers

As stated earlier, overcoming the force barrier leads to the formation of the lipid nanotubes. We measured the force (F_t) required for tube extension for different lipid compositions (Figure 6.4 C). This force is then used, together with the measured membrane tension, to calculate the nanotube radius and membrane bending rigidity (Figure 6.4 D-E). Bending rigidity, as an inherent membrane property, is linked to a large number of biological processes, for instance it affects growth rate and cell division in *E.coli* bacteria.³⁵

Nanotubes composed of PMPC require the lowest force to be extended, whereas the highest extension force was obtained for DOPC. Both saturated compositions exhibit lower tube extension forces when compared to the unsaturated compositions. Among unsaturated compositions, hybrid lipids show lower tube extension forces compared to DOPC. The forces we found for tube extension is within the range of forces reported in both pushing^{21, 47, 102} and pulling⁴⁸ experiments.

We calculated the radius of nanotubes (R_t) pushed from membranes of different compositions using $R_t = F_t / 4\pi\sigma$.¹⁹⁸ The radius of lipid nanotubes pulled from membranes were previously found to be in the range of 10-100 nm.²³⁷ On average, we computed larger nanotube radii for the saturated tail-asymmetric compositions compared to unsaturated ones (Figure 6.4 E). However, both PMPC and MPPC formed tubes of similar

diameters. Interestingly, hybrid counterparts of DOPC (i.e. SOPC, PLPC and POPC) formed larger tube radii than the tail-symmetric DOPC itself.

Tube extension forces can also be used to calculate bending rigidity using this relation:

$\kappa = F_t^2 / 8\pi^2 \sigma$.¹⁹⁸ Bending rigidity values can be categorized into two distinct clusters: saturated and unsaturated lipids. PMPC and MPPC, saturated mixed-chain compositions, exhibit comparable bending rigidities ($\kappa_{PMPC} = 4.68 \pm 0.57 \times 10^{-20} J$, $\kappa_{MPPC} = 4.79 \pm 1.21 \times 10^{-20} J$), which are slightly lower than those of the unsaturated lipids ($\kappa_{DOPC} = 6.23 \pm 1.58 \times 10^{-20} J$, $\kappa_{POPC} = 5.95 \pm 1.22 \times 10^{-20} J$, $\kappa_{SOPC} = 5.83 \pm 1.04 \times 10^{-20} J$, and $\kappa_{PLPC} = 5.79 \pm 1.1 \times 10^{-20} J$) (Figure 6.4 D).

Table 6.1: Results of the pushing experiments for various lipid compositions.

Composition	Membrane	Bending	Tube	Forward	Retraction	Nanotube
	Tension ($\mu\text{N}/\text{m}$)	rigidity ($\times 10^{-20}\text{J}$)	extension force (pN)	force barrier (pN)	force barrier (pN)	radius (nm)
PMPC	3.5 ± 0.6	4.7 ± 0.6	3.5 ± 0.4	18.3 ± 3.0	11.0 ± 31.5	85 ± 11
MPPC	4.2 ± 0.8	4.8 ± 1.2	4.0 ± 0.5	20.5 ± 4.0	13.45 ± 2.0	76 ± 13
POPC	5.9 ± 1.1	6.0 ± 1.2	5.2 ± 0.7	27.4 ± 5.3	18.45 ± 3.0	71 ± 13
SOPC	8.3 ± 3.2	5.8 ± 1.0	6.2 ± 1.5	36.9 ± 11.7	26.89 ± 10.8	60 ± 11
PLPC	9.6 ± 4.0	5.8 ± 1.1	5.8 ± 1.4	39.7 ± 19.5	22.4 ± 9.7	63 ± 15
DOPC	15.8 ± 4.8	6.2 ± 1.6	9.2 ± 2.9	74.7 ± 24.6	46.3 ± 20.4	45 ± 6

6.4 Hydrodynamics of lipid bilayers

6.4.1 Fluid slip at the interface of tail-asymmetric membranes

Cell membranes often experience fluid flow in their vicinity, which was shown to affect the proteins in the membrane (for instance integrins activation in endothelial cells by shear stress from the flow).²³⁸⁻²³⁹ At the interface of liposomes also, liquid flow influences the interaction of drug-carrier liposomes with target cancerous cells.²⁴⁰

Hydrodynamics at the interface of lipid membranes can be investigated by measuring the fluid-slip boundary condition at their interface with surrounding aqueous media.²⁰ Here,

characterizing interfacial fluid-slip is accomplished by measuring the drag force experienced by an optically trapped spherical bead as it is translated parallel to the membrane at a known velocity and at known distances from the membrane. A greater drag force denotes diminished fluid-slip at the interface, signifying an intensified boundary effect.²⁴¹ According to Faxén's law,¹⁸⁹ the presence of a rigid wall (no-slip boundary) leads to an approximately 140% enhancement in the drag force (D) acting upon the sphere at distance $d = 1.1a$ from the bead centre to the membrane compared to Stokes' drag force ($F_D = 6\pi\mu Ua$, where μ is medium viscosity, U is bead's relative velocity, and a is the bead's radius).¹⁸⁹

When there is fluid slip at the boundary or interface, a modified version of Faxén's law can be implemented as presented in equation 1. C_δ in equation 1 is the drag ratio defined as the value of experimentally measured drag force (D) normalized with Stokes' drag force and l_s is the fluid slip length. On lipid bilayer interfaces, it has been observed that not only membrane fluidity²⁰ but also the temperature of the membrane¹⁰² influence interfacial fluid-slip.

$$C_\delta = D/6\pi\mu Ua = [1 - (9/16)(a/d + l_s) + [O^3]]^{-1} \quad (2)$$

Utilizing equation 1 requires considering the membrane as a non-deforming boundary, meaning it does not undergo significant deformation while the bead moves and displaces the surrounding media, which has been demonstrated (also in chapter 5) with

freestanding planar bilayers mechanically sheared similarly as in the current study.¹⁰²

Figure 6.5 presents the measured drag ratio obtained at the interface of lipid bilayers made up of lipid compositions depicted in Figure 6.2. PC15 membranes, the fully saturated, tail-symmetric, subgel-phase²¹⁷ lipid composition, behave remarkably similarly to a rigid wall (no-slip boundary condition) as predicted by Faxén's law, implying minimal fluid slip at its interface ($C_\delta = 2.5 \pm 0.65$, $l_s \approx 0a$, $R^2 = 0.97$). However, a markedly distinct behavior is evident in PMPC and MPPC, the mixed-chain counterparts of PC15 (Figure 6.5 B). For PMPC, our investigation yielded a drag ratio of $C_\delta = 1.26 \pm 0.05$ at the interface corresponding to the fitted fluid-slip length of $l_s \approx 1.85a$, $R^2 = 0.91$. Similarly, for MPPC a drag ratio of $C_\delta = 1.25 \pm 0.03$ and $l_s \approx 1.8a$, $R^2 = 0.92$ were obtained. Although both PMPC (ripple phase²¹⁷) and MPPC (gel phase²¹⁷) are studied below their melting point and are saturated, they display a more fluidic behavior. The mismatched-length arrangement of the tails is one potential explanation to this, as the model put forth by Hui *et al* indicates that gel-phase, saturated, mixed-chain bilayers can create a loosely packed, fluidic hydrophobic core.⁹ This arrangement possibly promotes heightened chain disorder and fluidity within the system resulting in a reduced interfacial drag ratio.^{9, 242}

Regarding the unsaturated group, DOPC, the tail-symmetric and di-monosaturated composition, behaves similarly to PMPC heated above its melting point and to the DOPC:DPPC(3:2) mixture, both previously studied in chapter 5 with the same method.¹⁰²

A drag ratio of $C_\delta = 1.16 \pm 0.02$ is obtained for DOPC, corresponding to a fluid slip (l_s) of

$l_s \approx 4.4a$, $R^2=0.65$. SOPC, which is DOPC's hybrid counterpart with similar lengths of tails and just a mismatch in the unsaturation of chains, exhibits a similar behavior with $C_\delta=1.18 \pm 0.01$ and $l_s \approx 3.3a$, $R^2 = 0.77$. Similarly, PLPC, the other DOPC's hybrid counterpart with an equivalent degree of unsaturation but a shorter sn-1 tail, demonstrates a drag ratio of $C_\delta=1.17 \pm 0.03$ and $l_s \approx 3.6a$, $R^2 = 0.81$. Therefore, within this lipid family, a mismatch in either length or degree of saturation does not affect the fluid slip at the interface of the bilayer. On the other hand, POPC (possessing a mismatch in both the length and the unsaturation degree), exhibits reduced slip behavior compared to DOPC and the two hybrid compositions, with $C_\delta=1.20 \pm 0.03$ and $l_s \approx 2.7a$ ($R^2 = 0.87$). POPC positions itself between the saturated mixed-chain compositions and DOPC.

In our study, a reduced fluid-slip is observed in the saturated mixed-chain lipids compared with the unsaturated compositions ([Figure 6.5 E](#), [Table 6.2](#)). This can be explained by the denser packing of saturated mixed-chain lipids, resulting in hindered lateral lipid diffusion compared to their unsaturated counterparts.²¹⁰

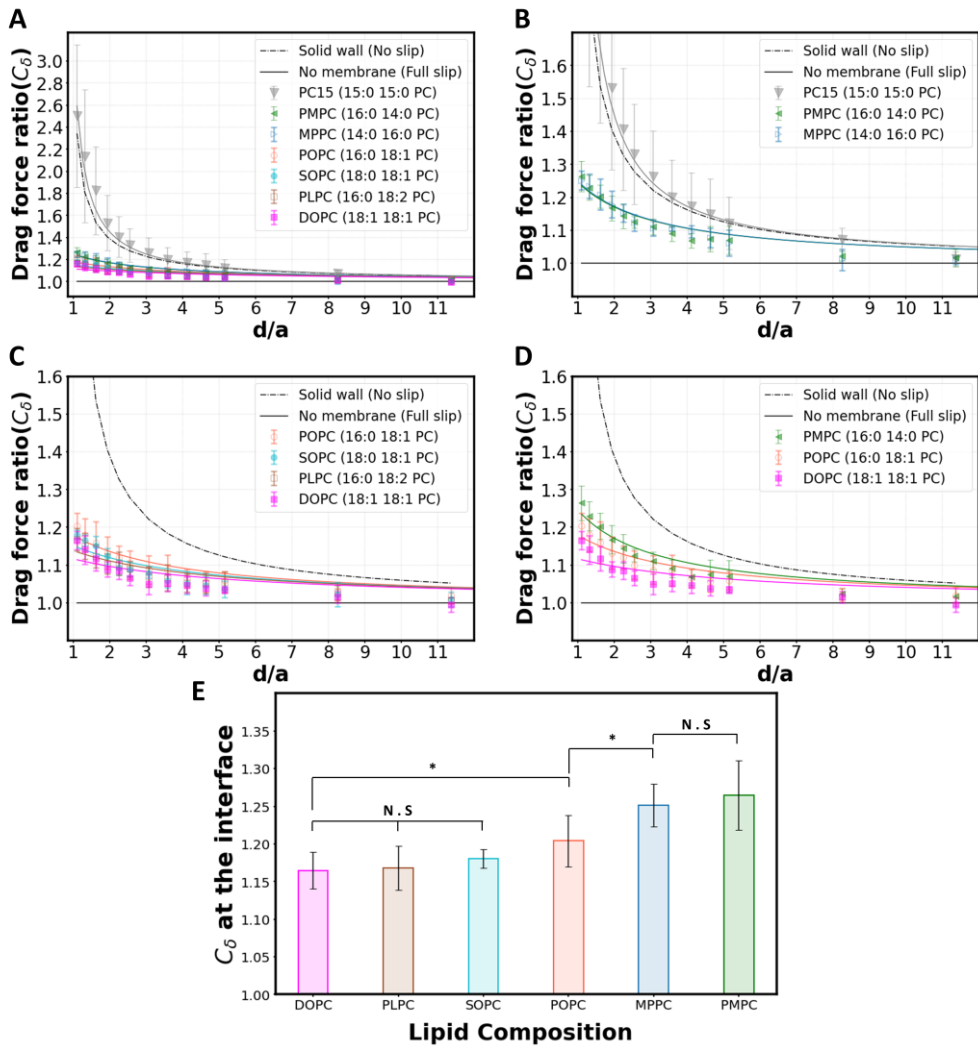


Figure 6.5: Drag ratio at the interface of various lipid compositions. A) Drag ratio at different distances from the membranes. B) Drag ratio at the interface of membranes with saturated lipid compositions. C) Drag ratio at the interface of membranes with unsaturated lipid compositions. D) A comparison of the drag ratio of PMPC, POPC, and DOPC. E) Value of drag ratio at $d = 1.1a$ for all compositions except PC15.

Table 6.2: Summary of outcomes from hydrodynamic experiments for different lipid compositions.

The slip length is determined by fitting the experimental drag ratio data to the modified Faxén formula (equation 1).

Composition	Interfacial drag ratio (C_δ)	Interfacial fluid slip (l_s) / a	R^2
PC15	2.5 ± 0.65	0	0.97
PC15 + 15% Cholesterol	1.98 ± 0.23	0	0.95
PC15 + 50% Cholesterol	1.66 ± 0.24	0.4	0.86
PMPC	1.26 ± 0.05	1.85	0.91
PMPC + 15% Cholesterol	1.28 ± 0.06	1.6	0.94
PMPC + 50% Cholesterol	1.41 ± 0.10	0.96	0.96
MPPC	1.25 ± 0.03	1.8	0.92
POPC	1.20 ± 0.03	2.7	0.87
POPC + 15% Cholesterol	1.21 ± 0.04	2.7	0.86
POPC + 50% Cholesterol	1.24 ± 0.05	2.1	0.94
SOPC	1.18 ± 0.01	3.3	0.77
PLPC	1.17 ± 0.03	3.6	0.81
DOPC	1.16 ± 0.02	4.4	0.65
DOPC + 15% Cholesterol	1.2 ± 0.03	3.3	0.73
DOPC + 50% Cholesterol	1.23 ± 0.06	2.1	0.88

6.4.2 Effect of cholesterol on hydrodynamics at the interface of bilayers of tail-asymmetric lipids

We then looked at the effect of cholesterol in the membranes, which is relevant since cholesterol makes up to ~50% (molar) of total lipids in biological membranes,²⁴³⁻²⁴⁴ and is known to affect hydrodynamic interactions at the cell membrane interface.²⁴⁵⁻²⁴⁷ However, the effect of cholesterol on the interfacial hydrodynamics of bilayers made specifically of tail-asymmetric lipids is yet to be explored.

Here, membranes were created using a mixture of the desired lipid composition (PC15, PMPC, DOPC, or POPC) and cholesterol (0%, 15% or 50% molar ratio) in the chloroform infused into the device. It is important to note that these cholesterol molar ratios correspond to the amount of cholesterol present in the chloroform solution introduced into the chip for membrane formation. This cholesterol-to-lipid ratio may not translate directly to the ultimate composition of the membrane.

As already shown in the previous section, sterol-free PC15 exhibits a solid-wall behavior, but the addition of cholesterol (50%) leads to a notable alteration in the pattern of fluid slip ($C_{\delta,50\%}=1.66 \pm 0.15$ and $l_{s,50\%} \approx 0.4a$, $R^2 = 0.86$), see [Figure 6.6 A](#). This more fluidic behaviour is likely caused by cholesterol disrupting the tightly-packed membrane.²⁴⁸⁻²⁴⁹ At 15% level cholesterol, however, this fluidizing effect is less significant. The mixed-chain counterpart of PC15, PMPC, shows the opposite behaviour. It shows reduced slippage when cholesterol is added at 50% concentration ($C_{\delta,50\%}=1.41 \pm 0.1$ and

$l_{s,50\%} \approx 0.96a$, $R^2 = 0.96$). However, it still retains a fluid-like behavior that remains distinct from a solid wall.

Now focussing on unsaturated lipids ([Figure 6.6 C-D](#)), for DOPC the drag ratio increased with higher cholesterol content ($C_{\delta,50\%}=1.23 \pm 0.05$ and $l_{s,50\%} \approx 2.1a$, $R^2 = 0.88$) and is unaffected by the low cholesterol content. Similarly, the drag ratio at the interface of POPC ($C_{\delta} = 1.20 \pm 0.03$ and $l_s \approx 2.7a$) demonstrates no significant effect at 15% cholesterol and experiences only a slight rise at 50% level ($C_{\delta,50\%}=1.24 \pm 0.05$ and $l_{s,50\%} \approx 2.1a$, $R^2 = 0.94$). This decrease in the fluid slip at the interface of unsaturated membranes in the presence of cholesterol is not surprising. The introduction of cholesterol strengthens van der Waals contact among the PC-chains;²⁵⁰ this decreases the lateral lipid diffusion²⁵¹⁻²⁵³, likely to lead to a higher drag ratio at the interface. For better comparison, all the results for the cholesterol section can be found in [Figure 6.6 E](#) and [Table 6.2](#).

A close look at the drag ratio values we measured in the presence of cholesterol reveals a crucial observation: the drag ratio at the interface of unsaturated lipid compositions (i.e. DOPC and POPC) displays reduced sensitivity to cholesterol in comparison to saturated compositions (i.e. PC15 and PMPC). Additionally, among the studied lipid compositions, asymmetry in the tails is correlated to a lower cholesterol sensitivity; with both PMPC and

POPC demonstrating lower cholesterol sensitivity than their respective tail-symmetric analogues.

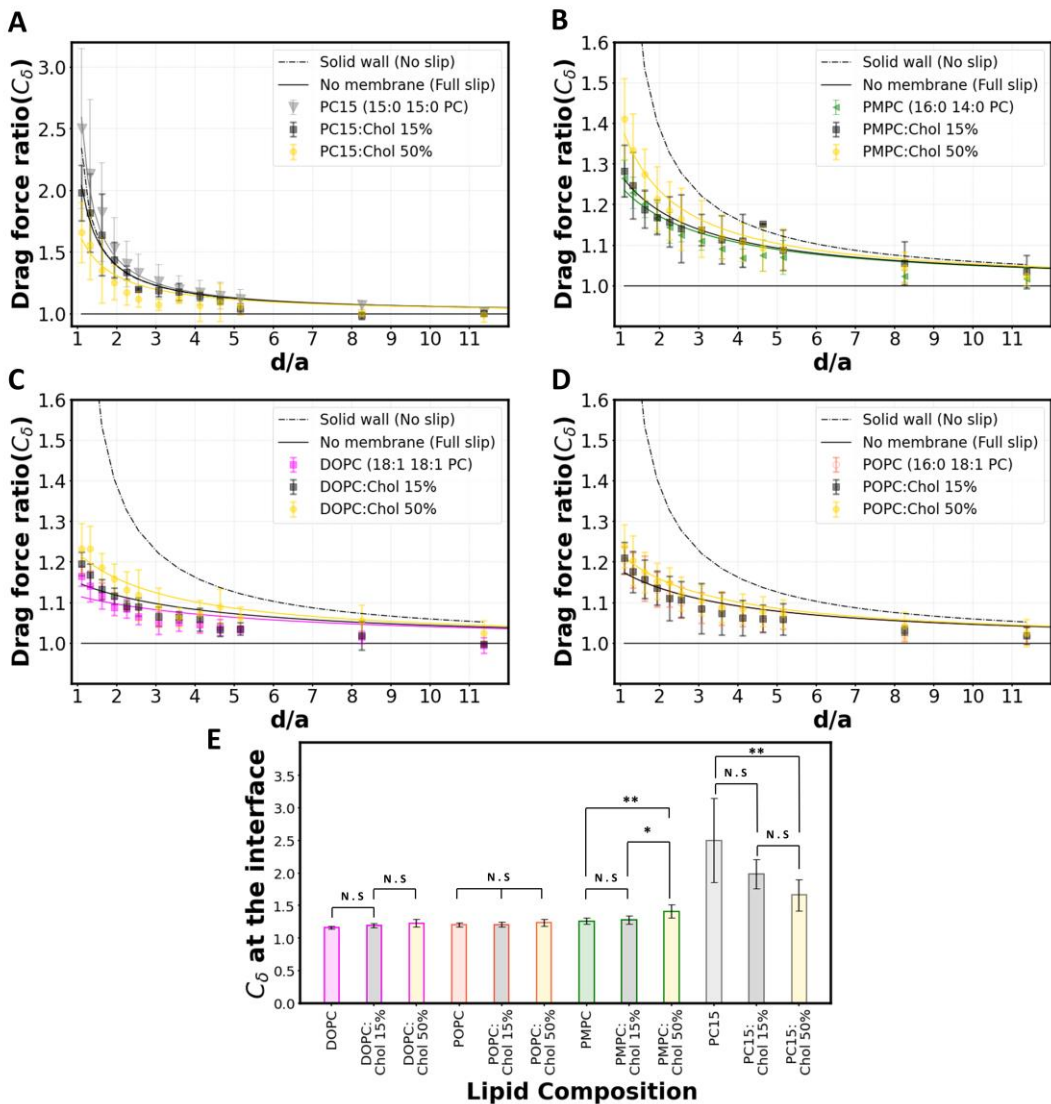


Figure 6.6: Cholesterol effect on the drag ratio at the interface of membranes with various lipid compositions. A to D) Cholesterol effect on the drag ratio at interface of selected lipid compositions. E) Interfacial drag ratio of the selected lipid bilayers.

6.5 Conclusion

We systematically studied the mechanical characteristics of freestanding planar vertical lipid bilayers made of chain-asymmetric phospholipids formed inside microchannels. We showed that PC15's mixed-chain analogues, in contrast to PC15, show a more fluid-like behaviour when considering the fluid slip at their interface. We noted a lower membrane tension and bending rigidity for saturated mixed-chain compositions compared to the unsaturated ones. Furthermore, we demonstrated that hybrid counterparts of tail-symmetric DOPC possess lower tension values in comparison to DOPC, while having similar bending rigidity. Additionally, we demonstrated that regardless of saturation status, tail-asymmetry reduces the force-barrier required for microparticles entry/release within the studied lipid bilayers. By introducing cholesterol, our findings reveal a consistent pattern in both the saturated and unsaturated lipid compositions: tail-asymmetry mitigates the sensitivity of interfacial fluid-slip to cholesterol. Additionally, in response to cholesterol, we observed a striking contrast in the behaviour of saturated mixed-chain PMPC (rigidifying with cholesterol) compared to its tail-symmetric counterpart, PC15 (fluidizing with cholesterol).

In conclusion, our findings reveal that tail-asymmetry alters membrane properties and membrane-cholesterol interaction even to the extent of opposing the behavior of the tail-symmetric analogous. Secondly, they suggest that saturated mixed-chain lipids may serve as effective substitutes for unsaturated lipids, providing comparable membrane fluidity

and flexibility without the oxidative susceptibility of unsaturated lipids.²⁵⁴ Additionally, hybrid counterparts of DOPC exhibit fluidic membranes with low membrane tension, making them promising candidates for flexible drug carrier design.^{211, 255}

6.6 Materials and Methods

In our experiments, we used the microfluidic chip developed in chapter 2.

6.6.1 Lipids and membrane formation

1,2-dioleoyl-sn-glycero-3-phosphocholine (DOPC), Palmitoyl-myristoyl-PC (PMPC), 1,2-dipentadecanoyl-sn-glycero-3-phosphocholine (PC15), 1-myristoyl-2-palmitoyl-sn-glycero-3-phosphocholine (MPPC), 1-palmitoyl-2-linoleoyl-sn-glycero-3-phosphocholine (PLPC), 1-palmitoyl-2-oleoyl-glycero-3-phosphocholine (POPC), 1-stearoyl-2-oleoyl-sn-glycero-3-phosphocholine (SOPC), and cholesterol were purchased from Avanti in chloroform at a concentration of 10 mg/ml. They were stored at -20 °C and used directly without additional purification. The aqueous phase was prepared by adjusting a 10 mM 4-(2-hydroxyethyl)-1-piperazineethanesulfonic acid (HEPES) solution to pH 7.4 with concentrated KOH. Subsequently, KCl and bovine serum albumin (BSA) were added to reach final concentrations of 150 mM and 0.5 mg/ml, respectively, and the aqueous buffer was filtered using a 0.2µm sterile filter. Then, 2 µm beads (actual diameter = 1.93µm, Polysciences Inc.) were diluted 25000 times in this aqueous buffer. The flow into the chip was infused using a ProSense NE-30 syringe pump. During membrane formation, the pump operated at high flow rates (5µl/min) until all the chloroform was expelled from

the chip. Once the complete removal of chloroform was confirmed, the pump was stopped. Experiments were conducted on membranes aged between 2 to 8 hours.

6.6.2 Optical tweezers experiments

The optical tweezers (OT) methods for both shearing and pushing the membrane were previously well-documented^{20-21, 102} and is also discussed in chapters 2 and 5 of the present thesis. A 1.2 NA water immersion objective (FI Plan Apo VC 60×, Nikon) was employed to optically trap the bead within microchannels. This setup was mounted on a piezo stage (NANO-LPS100, Mad City Labs) and utilized a 1064 nm trapping laser (YLR-10-LP-Y12, IPG Laser) and an 830 nm detection laser (LDT830-30GC, TOPAG). Signal processing involved anti-aliasing filtering and pre-amplification (10 dB) via a KROHN-HITE 3364 for the voltage signals from a position-sensitive detector (PSD, DL100-7-PCBA3, First Senso). All experiments were conducted with the trapped bead at 30 μm above the flow cell's surface. In the shearing experiments, a travel distance of 25 μm was used at a rate of 100 μm/s. For pushing experiments, fine positioning of the trapped bead relative to the membrane was done using the piezo stage. The stage progressed incrementally in step sizes from 0.03 μm to 0.08 μm, with data collection performed at each position in a quasi-static manner. The PSD signal was recorded for 0.5 seconds at a sampling rate of 1 kHz, with a cut-off frequency of 500 Hz. For calibration of the setup, trap stiffness determination, quantification of bubble traps (flow measurement through the gap), and shearing experiments, signals were sampled at 50 kHz with a cut-off frequency of 24.5

kHz. All signals from the OT were subjected to processing and conversion into units of nm and pN using a custom Python code.

6.6.3 Image processing for surface tension measurements

To monitor both the membrane and the bead, a CMOS camera (DCC1545M, Thorlabs GmbH) with a resolution of 11.5 px/ μm was employed for recording videos during the pushing experiments, capturing at a rate of 14 fps. The recorded videos were converted into tiff format, followed by cropping and filtering with an FFT band pass filter in ImageJ to enhance contrast. The processed tiff files were then subjected to analysis using a customized Matlab to extract the membrane deformation angle. The custom script undertakes the following steps for each frame: First, it determines the center coordinates of the bead as described in chapter 5. Next, it identifies the positions of maximum intensity along the membrane on the right side of the bead. Subsequently, a third-order polynomial is fitted to these membrane coordinates, allowing for subpixel resolution. This process facilitates the calculation of the angle between the deformed membrane and its original position, situated 32 pixels horizontally away from the bead's center. The obtained angles are then averaged across a minimum of 28 frames to calculate the surface tensions when the piezo stage was displaced by 2 and 4 μm from its initial position.

6.6.4 Statistical analysis

To assess the significance among the data, Kruskal-Wallis p-value calculations were performed with a significance threshold set at 0.05. The obtained p-values are

comprehensively listed in [Table S 6.1](#). P-values depicted on the graphs are denoted by symbols: * indicates significance at $p < 0.05$, ** at $p < 0.01$, and *** at $p < 0.001$. Error bars in all figures represent standard deviations of the data. Box plots in all figures illustrate quartiles with the box, the median with a horizontal line, and whiskers extending to the most extreme data points. Number of independent membranes tested for this chapter are as follows: 5 for DOPC, 10 for SOPC, 9 for PMPC, 10 for MPPC, 9 for PLPC, and 10 for POPC.

6.5 Supplementary Information

Table S6.1: Kruskal-Wallis p-value of different experiments on various lipid compositions

Composition	Tension	Bending rigidity	Tube extension force	Forward force barrier	Retraction force barrier	Interfacial drag ratio (C_δ at $d/a=1.1$)	Nanotube radius
PMPC & MPPC	0.02	0.93	0.01	0.22	0.04	0.88	0.3
MPPC & POPC	0	0.01	0	0.005	0.014	0.03	0.22
POPC & SOPC	0.004	0.88	0.045	0.04	0.053	0.15	0.05
SOPC & PLPC	0.9	0.74	0.4	0.74	0.031	0.2	0.57
PLPC & DOPC	0.008	0.51	0	0.018	0.015	0.93	0.03
POPC & PLPC	-	-	-	-	-	0.08	0.57
POPC & DOPC	-	-	-	-	-	0.011	0.002
PMPC & DOPC	-	-	-	-	-	-	0.002
PC15 & PC15: 15% Chol	-	-	-	-	-	0.1	

PC15: 15% Chol & PC15: 50% Chol	-	-	-	-	-	0.11
PC15 & PC15: 50% Chol	-	-	-	-	-	0.01
PMPC & PMPC: 15% Chol	-	-	-	-	-	0.4
PMPC: 15% Chol & PMPC: 50% Chol	-	-	-	-	-	0.013
PMPC & PMPC: 50% Chol	-	-	-	-	-	0.002
POPC & POPC: 15% Chol	-	-	-	-	-	0.68
POPC: 15% Chol & POPC: 50% Chol	-	-	-	-	-	0.29
POPC & POPC: 50% Chol	-	-	-	-	-	0.28
DOPC & DOPC: 15% Chol	-	-	-	-	-	0.07
DOPC: 15% Chol & DOPC: 50% Chol	-	-	-	-	-	0.1
DOPC & DOPC: 50% Chol	-	-	-	-	-	0.002

Chapter 7

Effect of azithromycin on the mechanical properties of POPC membranes

Abstract

As a proof of concept for the developed chip in Chapter 3, we successfully formed 1-palmitoyl-2-oleoyl-glycero-3-phosphocholine (POPC) bilayers on the chip and delivered the antibiotic azithromycin at low (5 μM) and high (250 μM) doses. Using optical tweezers, we characterized how azithromycin at these two concentrations influenced the elastic properties of the membrane, including tension and bending rigidity. This microfluidic device is a versatile tool that can deliver various buffers, molecules or nano-/microparticles to freestanding membranes in order to study the resulting impact on the membrane properties.

Part of this chapter is included in a paper: Yahyazadeh Shourabi, Arash, Martina Iacona, and Marie-Eve Aubin-Tam. "Microfluidic system for efficient molecular delivery to artificial cell membranes." *Lab on a Chip* 25.7 (2025): 1842-1853.

7.1 Introduction

Azithromycin, chemically known as 9-Deoxy-9a-aza-9a-methyl-9a-homoerythromycin (Figure 7.1), is an azalide—a subclass of macrolides—first synthesized in 1980²⁵⁶⁻²⁵⁷. Azithromycin possesses notable immunomodulatory properties, making it effective for treating conditions beyond infections. Recently, it has been utilized as an adjunctive therapy for various periodontal diseases, including acute and chronic periodontitis, as well as drug-induced gingival overgrowth²⁵⁸. The most common dosage regimen for azithromycin is 500 mg taken orally once daily for three days, one hour before meals. This regimen ensures good patient compliance due to its short duration and the low incidence of side effects²⁵⁹. Interestingly, azithromycin has been used internationally off-label as a treatment for patients with COVID-19²⁶⁰. Due to its conventional use and also its known interaction with the cell membrane²⁶¹, this drug was chosen for the biophysical study of this thesis chapter.

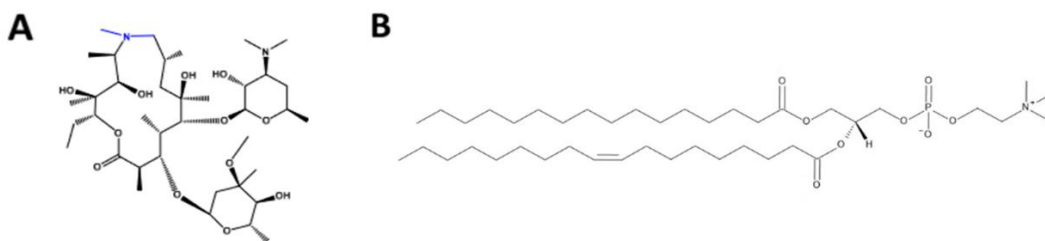


Figure 7.1: A) Chemical structure of azithromycin (This image is adapted from ref²⁶²). B) Chemical structure of POPC (This image is adapted from ref²⁶³).

As for the model membrane, POPC (1-palmitoyl-2-oleoyl-sn-glycero-3-phosphocholine, Figure 7.1 B) lipids were chosen for this study due to their abundance in biological membranes²⁶⁴⁻²⁶⁵. This lipid is also a popular composition for scientific studies, both experimentally²⁶⁶ and numerically²⁶⁷.

In this chapter, utilizing the new drug delivery chip developed in Chapter 3, the effect of azithromycin at low and high dosages is investigated on POPC model membranes on chip. Obviously, the procedure described here can be followed to study any other bilayer interaction with other desired molecules/drugs of interest on the chip.

7.2 On-chip delivery of azithromycin to POPC lipid bilayers

We proceeded with a proof-of-concept study to deliver an antibiotic drug, azithromycin, to POPC bilayers on the chip. In this study, we investigated the drug's effects on the membranes through mechanical characterization before and after drug delivery. The mechanical characterization of the bilayers focused on particle entry/release force barriers, membrane tension, and bending rigidity, and was performed using optical tweezers interfaced with the membranes on the chip as previously described in chapters 2, 5, and 6 of the present thesis and also in the literature.^{21, 102}

POPC lipid dissolved in chloroform was flown into the chip via the membrane channel inlet, followed by a solution of 2 μm polystyrene beads diluted 25000 times in HEPES solution. After membranes were formed at the gaps, they were left for 2 hours to rest, and mechanical characterizations were performed using optical tweezers. Representative force-displacement curves for both forward and backward pushing with the optical tweezers are depicted in [Figure 7.2 A](#). The behaviour follows the classic force-displacement curves observed in pushing⁴⁷ or pulling⁴⁸ vesicles using optically trapped microbeads. In short, upon bead-membrane contact, the membrane deformed and began to wrap around the bead. As the pushing continued, this deformation progressed linearly until reaching a maximum force (force barrier for particle entry), after which a nanotube was

formed. Extending the nanotube required a constant force. Upon reaching a few microns of extension, the direction of movement was reversed towards retraction, leading to the disappearance of the tube. Subsequently, the bead transitioned from a partially wrapped state back to its original unwrapped state in a linear force manner, mirroring the forward pushing process, until returning to the zero-force state when the bead is fully released from the membrane.

Using the force values extracted from these force-displacement curves, we calculated membrane tension and bending rigidity values. [Figures 7.2, 7.3, and 7.4](#) present the results of these experiments on the POPC bilayer (prior to any flow replacement), illustrating tension ($\sigma = 6.1 \pm 2.5 \mu\text{N}/\text{m}$), forward ($32.1 \pm 12.2 \text{ pN}$) and retraction ($18.3 \pm 6.5 \text{ pN}$) force barriers, tube extension force ($5.9 \pm 2.1 \text{ pN}$), and bending rigidity ($\kappa = 7.7 \pm 4.4 \times 10^{-20} \text{ J}$). These measurements are comparable to those obtained using a similar method on POPC bilayers in the present thesis.¹⁰²

Afterwards, we investigated how azithromycin affects the elastic properties of the lipid bilayers. For this purpose, azithromycin (at a concentration of either $0 \mu\text{M}$, $5 \mu\text{M}$, or $250 \mu\text{M}$) and $2 \mu\text{m}$ polystyrene beads were added to the HEPES solution and introduced from the replacement channel to replace the initial HEPES solution surrounding the membranes (following the procedure described earlier in Chapter 3). The membranes were then incubated in the new media for one hour, after which the optical experiments were repeated. The control with $0 \mu\text{M}$ azithromycin aimed to assess any potential effects of the flow replacement procedure on the bilayers.

Representative force-displacement curves for the drug-free, low-dose, and high-dose drug tests are all shown in [Fig. 7.2 A](#). After replacing the media with the drug-

free solution, we find that the membrane tension showed a slight decrease (Figure 7.2 B), leading to a decrease in the force barriers (Figure 7.3) and tube extension force (Figure 7.4).

However, bending rigidity remained unchanged (Figure 7.4). The sole process of replacing the media affects the membrane tension. The buffer replacement possibly affects the annulus size/composition and/or washes away some lipid molecules out of the system, which can affect the membrane tension, showing the importance of performing this control at 0 μM azithromycin.

When the lipid bilayers were exposed to azithromycin, a significant decrease in membrane tension was observed, particularly at the higher dose. We report an average membrane tension of $\sigma = 2.9 \pm 0.4 \mu\text{N}/\text{m}$ for the low-dose and $\sigma = 2.0 \pm 0.7 \mu\text{N}/\text{m}$ for the high-dose treatment (Figure 7.2 B).

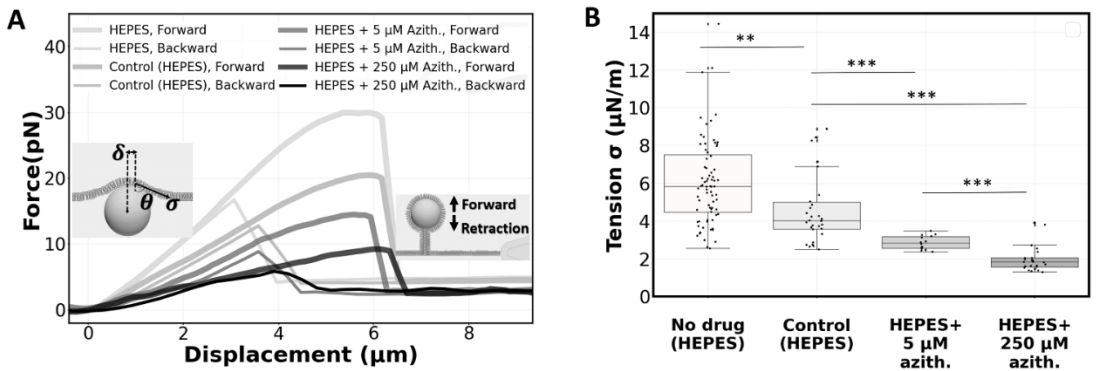


Figure 7.2: Force displacement curves and membrane tension values of POPC lipid bilayers with/without azithromycin.

A comparison of the force barrier for particle entry before and after drug treatment indicates that azithromycin facilitates particle entry into POPC membranes ($15.1 \pm$

2.2 pN for low-dose and 11.5 ± 3.6 pN for high-dose, [Figure 7.3 A](#)). Similarly, [Figure 7.3 B](#) shows a decrease in the force barrier for particle release from membranes treated with azithromycin (9.0 ± 0.9 pN for low-dose and 7.5 ± 2.1 pN for high-dose).

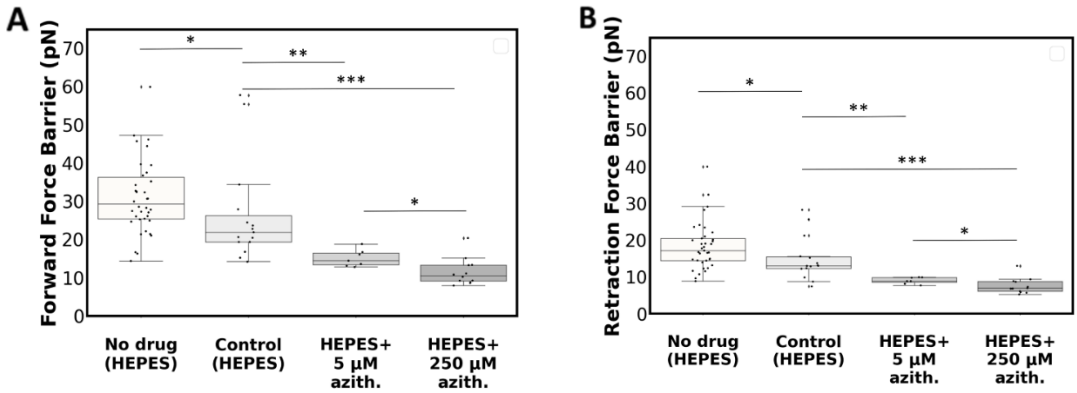


Figure 7.3: Forward and retraction force barriers for POPC bilayers with/without Azithromycin.

[Figure 7.4 A](#) demonstrates that the tube extension force from POPC bilayers is also significantly reduced after drug treatment. It drops to 3.7 ± 1.1 pN and 3.7 ± 1.3 pN for low-dose and high-dose experiments respectively. Bending rigidity is unaffected by the drug at low doses, but shows a slight increase to $\kappa = 9.0 \pm 3.9 \times 10^{-20}$ J at the 250 μ M concentration ([Figure 7.4 B](#)).

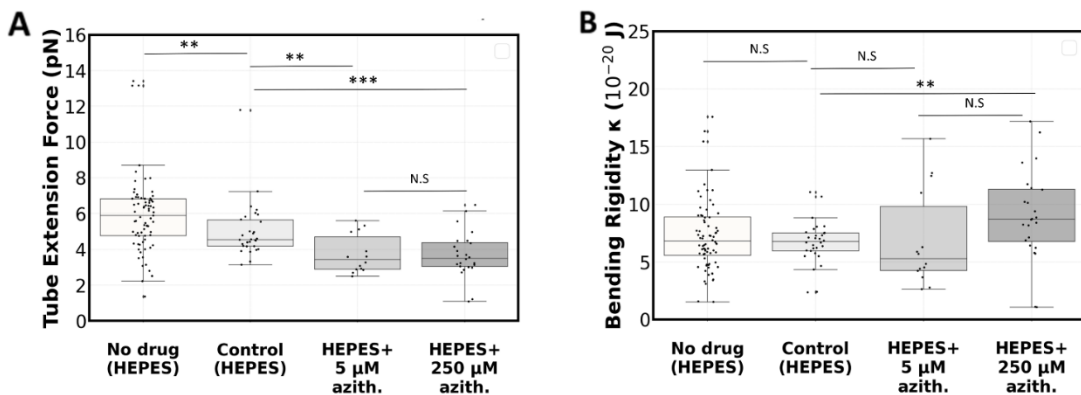


Figure 7.4: Tube extension force and bending rigidity values of POPC bilayers and the effect of azithromycin on them.

Our findings on the effect of azithromycin on bending rigidity of POPC freestanding bilayers differ from the ones reported for DOPC vesicles having their outer leaflet treated with azithromycin.⁴⁴ This can be due to differences in lipid composition, in drug/lipid ratio, and/or in drug distribution across the bilayer, since membrane asymmetry is known to affect bending rigidity.²⁶⁸⁻²⁷⁰ Azithromycin was previously shown to have different effects on membrane fluidity depending on the lipid composition.²⁷¹ Also noteworthy, the mentioned drug dosage corresponds to the input concentration into the system. It is possible that not all drug molecules end up in the membrane, because some molecules might adhere to the channels. However, the use of NOA81 channels is likely an advantage here, since the absorption of some small molecules (e.g., ATP analog 3-MBPP1) was found to be reduced on NOA81 in comparison to PDMS.²⁷²

In summary, membranes exposed to azithromycin exhibited softer characteristics, requiring significantly lower forces for deformation, particle entry/release, and nanotube formation/extension, particularly at higher drug concentrations. Azithromycin is expected to interact electrostatically with the negative charged

group in the polar head of PCs, as demonstrated by ^{31}P NMR spectroscopy.²⁷³ Also, given its amphipathic nature,²⁷⁴ azithromycin can insert into membranes. Specifically, it was found that azithromycin insertion within the polar heads of 1,2-dioleoyl-sn-glycero-3-phosphocholine (DOPC) induces an expansion in the area occupied by each lipid molecule, increasing it from 68.6 \AA^2 in its pure form to 75.9 \AA^2 . This interaction decreases the lipid-lipid interaction energy, making the membranes more easily deformable.⁴⁴ A similar effect might be at the origin of the decrease in membrane tension and in force barrier values after drug treatment.

7.3 Conclusion

As a proof of concept of the developed microfluidic system in Chapter 3, we investigated the impact of azithromycin on the mechanical properties of POPC bilayers formed on the chip. Our findings revealed a reduction in membrane tension, in force barriers for particle entry and release, and in nanotube extension forces in drug-affected membranes, particularly at higher drug concentrations.

7.4 Materials and Methods:

7.4.1 Chemicals, buffers, lipids, and flows

POPC (1-palmitoyl-2-oleoyl-glycero-3-phosphocholine) was purchased from Avanti in chloroform with 25 *mg/ml* concentration, stored at -20 °C, and was directly used for experiments. To create the aqueous phase that we refer to as the HEPES solution, 10 mM 4-(2-hydroxyethyl)-1-piperazineethanesulfonic acid (HEPES) was adjusted to pH 7.4 using concentrated KOH, KCl (150 mM) and bovine serum albumin (0.5 mg/ml) were added, and the solution was filtered with a 0.2 μ m sterile filter. For the bead-containing experiments, after filtration, 2 μ m polystyrene beads (real diameter= 1.93 μ m, Polysciences Inc.) were dissolved in the buffer. Two identical ProSense NE-30 syringe pumps were used to infuse the flow into the chip via inlet 1 and inlet 2. For membrane formation the flow rate of 5 – 9 μ l/min would usually give several stable bilayers. However, for the replacement or the reversible

replacement of the media we advise to use $2.5 \text{ ul}/\text{min}$. To minimize the residual flow after stopping the pumps, tubing with short length was used (no longer than 5 cm). For the laser-induced fluorescent tests, Rhodamine B was dissolved in the HEPES solution. For the drug experiment, azithromycin (Sigma-Aldrich) was dissolved in 0.1 M HCl and then added to the HEPES solution to reach final azithromycin concentrations of $5 \text{ }\mu\text{M}$ or $250 \text{ }\mu\text{M}$. For blocking outlet ports during the drug delivery phases, UV curing glass repair adhesive (Bison) was used.

7.4.2 Optical tweezers experiments

The optical tweezers (OT) methods for both the shearing and pushing experiments were previously described in chapters 2, 5, and 6 of the present thesis and also in the literature.^{20-21, 102} All experiments were conducted at a height of $30 \text{ }\mu\text{m}$ above the surface of the flow cell. A 1.2 NA water immersion objective (FI Plan Apo VC 60x, Nikon) was used to optically trap a bead inside microchannels mounted on a piezostage (NANO-LPS100, Mad City Labs) with a 1064 nm trapping laser (YLR-10-LP-Y12, IPG Laser) and an 830 nm detection laser (LDT830-30GC, TOPAG). Anti-aliasing filtering and pre-amplification (10 dB) was done (KROHN-HITE 3364) on the voltage signals coming from a position-sensitive detector (PSD, DL100-7-PCBA3, First Sensor).

In the pushing experiments, fine positioning of the bead relative to the membrane was controlled using the piezo stage. The stage was moved sequentially in steps from 120-240 nm, and at each position, data collection

was performed by recording the PSD signal for 0.5 seconds at a sampling rate of 1 kHz with a cut-off frequency of 500 Hz. For setup calibration and trap stiffness calculation, signals were sampled at 50 kHz with a cut-off frequency of 24.5 kHz. All signals from the PSD were processed and converted to nm and pN using a custom-made Python code. The trap stiffness used for pushing membranes was in the range of 0.10-0.13 pN/nm. Prior to pushing each membrane, calibration of the trap was performed with the bead center at a distance of 3 μm from the membrane.

To calculate tension, the force values (F) from the linear region of the force-displacement curves were used in the formula $\sigma = \frac{F}{2\pi\delta \cos\theta}$; where δ is the distance between the bead center and the point where the angle θ of the membrane is measured. To calculate θ , a previously published method was used¹⁰² which is described in chapter 5. Bending rigidity was calculated via formula $\kappa = \frac{F_t^2}{8\pi^2 \sigma}$; where F_t is the tube extension force and σ is the membrane tension.

7.4.3 Statistical analysis

A Kruskal-Wallis one-way statistical analysis was conducted using a significance threshold of $p = 0.05$ to determine significance. P-values on the graphs are indicated as follows: * for $p < 0.05$, ** for $p < 0.01$, and *** for $p < 0.001$. Error bars in all figures denote the standard deviation. In all box plots, the box represents the quartiles, the horizontal line indicates the median, and the whiskers extend to the most extreme data points. The

number of independent optical tweezers experiments performed is as follow: 38 experiments for tests done before the replacement, 15 experiments for the HEPES solution control, 7 experiments of the low-dose, 12 experiments for the high-dose drug exposure. Each experiment was performed on a different membrane using a different bead on at least four different microfluidic chips.

Chapter 8

Conclusions and Outlook

*“Do not weep. Do not wax
indignant. Understand.”*

Baruch Spinoza

8.1 Conclusion and Outlook

Lipid bilayers are among the most widespread yet complex biomaterials¹⁵¹. It is not only interesting to learn more about the bilayers themselves as components of complex, dynamic, and heterogenous cell membranes²⁷⁵, but also crucial due to their significance in cell-drug interactions¹³. Developing *in vitro* systems for the formation and characterization of artificial cell membranes is a promising approach to contribute to a deeper understanding of the biological phenomena occurring at the plasma membrane level *in vivo*^{13, 177}.

Although a vast literature, both experimental^{31, 229} and numerical^{202, 276}, exists on the preparation and physical characterization of cell membrane models, many critical challenges in the field remain unaddressed. Developing a platform for the robust formation^{29, 83} and drug treatment¹³ of artificial cell membranes that also enables accurate measurements of their physical properties²⁶ is in its infancy. The present thesis was an effort in taking a step forward toward developing a new generation of lipid bilayer-based microfluidic platforms and revealing biophysical properties of artificial cell membranes on chip.

The three key questions explored in this thesis are summarized as follows:

1. “How to fabricate robust artificial cell membranes on microfluidic chips?”

Lipid bilayers are inherently soft, flaccid materials because they are very thin and composed of lipids held together by weak noncovalent interactions. This makes forming and handling them *in vitro* quite challenging. This is especially true when forming lipid bilayers with with single-component compositions that lack a solid support specifically if it's not in fluid phase.

In the context of *in vitro* microfluidic formation of lipid bilayers, the hydrodynamics of the flow inside the channels is a limiting factor for their stability. The situation can worsen when unwanted bubbles, a well-known microfluidic challenge, are present in the system, adding more uncertainty and complexity to the hydrodynamic conditions inside the channels. We thus need a device that ensures a bubble-free balanced fluidic pressure on both leaflets of the membrane. Even the slightest unfavorable hydrodynamic condition can lead to the warping and destruction of the lipid bilayer due to its flaccid nature.

An important goal of this thesis was to develop various microfluidic platforms for different types of measurements while addressing the pervasive challenges of low stability of the membranes and low throughput rate of their formation on a chip. This was achieved by developing a fluidic design for the chips capable of providing balanced fluidic conditions for the membranes through: 1- special geometric designs like walls with stream-lined shapes for the multi membrane-on-chip systems, 2- accommodating several island-structure micropillars in the channels for high-throughput membrane formation on multi membrane-on-chip systems, 3- introducing a novel bubble trap integrated into the chips to tackle the long-standing microfluidic bubbles problem, and the 4- development of bi-directional fluidic-based diodes integrated into the single membrane-on-chip systems.

We demonstrated that our optimized designs pave the way for the robust and high-throughput formation of lipid bilayers of various compositions and their subsequent treatment and mechanical or electrophysiological characterization.

2. “How do temperature, cholesterol content, and lipid tail asymmetry affect the mechanical properties of freestanding planar bilayers?”

A robust microfluidic platform allows for in-depth exploration of the properties of freestanding planar lipid bilayers on a chip. This is particularly important because this membrane configuration provides multiple benefits: the membrane can be characterized in an unsupported condition, the device can be interfaced with optical tweezers, and each leaflet is independently accessible. So far there have been very few studies that fulfilled all those conditions.

We characterized unsupported lipid bilayer membranes under various conditions. First, we investigated the effect of temperature on their mechanical properties. We selected PMPC and DOPC:DPPC (3:2) compositions, both with a melting point of 27 °C and expected to be in a ripple and gel-fluid phase respectively at room temperature. Both compositions showed an increase in membrane tension upon heating, particularly at temperatures above 27 °C. Other mechanical properties, such as tube extension force and forward/backward force barriers, also followed this trend. However, the bending rigidity of both compositions remained stable with temperature changes. We also measured the effect of temperature on interfacial fluid slip. Although temperature did not significantly affect this parameter in DOPC:DPPC membranes, PMPC exhibited a significant drop in

interfacial fluid slip upon fluidization. As for a control, we also measured tension and rigidity changes with temperature of POPC bilayers, that do not go through a phase transition in the temperature range of our experiments. Indeed, both tension and rigidity were temperature-stable in this case.

Next, we examined the impact of lipid composition on the mechanical properties of freestanding planar bilayers, focusing on lipid tail-asymmetry and cholesterol content. We studied two categories of lipids: saturated and unsaturated. Within each category, we measured the properties of tail-symmetric lipids alongside their tail-asymmetric counterparts. Our measurements showed that the tail-asymmetric counterparts of DOPC (i.e., POPC, SOPC, and PLPC) generated membranes with lower tension and similar bending rigidity to DOPC. These lipids exhibited fluidic behavior with high interfacial fluid slippage, indicating the bilayers are softer than DOPC bilayers. Among the unsaturated lipids, POPC, the tail-asymmetric analog of DOPC with asymmetry in both chain length and degree of saturation, had the lowest membrane tension and interfacial fluid slippage.

In the saturated lipid group, we studied PC15 (gel-phase) and its tail-asymmetric analogs PMPC (ripple-phase) and MPPC (gel-phase). Despite all three compositions being below their melting points, they exhibited contrasting behaviors. PC15 showed solid behavior, while tail-asymmetry induced a high degree of fluidity in both PMPC and MPPC, though less fluidity than in the unsaturated compositions. Interestingly, PMPC and MPPC produced very soft membranes with lower tension and bending rigidities than even the unsaturated compositions. This suggests that tail-asymmetric membranes with a saturated structure could substitute unsaturated lipid compositions in applications where lipid oxidation is a concern, while still providing fluidity and softness. This is particularly significant for designing lipid-based systems like drug carriers, where soft, flexible membranes with reduced susceptibility to oxidation are required.

We also tested the effect of cholesterol content on our membrane systems, focusing on the combinatorial effect of tail-asymmetry and cholesterol on lipid bilayer properties. We found that cholesterol fluidizes PC15 membranes but stiffens the tail-asymmetric counterpart PMPC. In the unsaturated group, cholesterol stiffened both the tail-symmetric and tail-asymmetric compositions.

Additionally, our study indicated that tail-asymmetry alleviates the effect of cholesterol on the interfacial fluid slip of the membranes. This can be useful to consider when designing lipid-based drug carriers targeted to be less sensitive to cholesterol content variations.

3. “Can we develop an on-chip lipid bilayer-based drug-screening platform?”

Forming stable lipid bilayers on chip is a challenge in itself. But, when it comes to on-chip drug delivery to the bilayers post-formation, there is a new challenge, namely to achieve reversible buffer change around lipid bilayers⁵⁸. As discussed earlier, the flaccid nature of the membranes makes them vulnerable to even slightest unfavorable hydrodynamic condition. This makes it very difficult to deliver molecules to the membranes post their formation. Although there is a heavy demand for drug screening chips based on artificial cell membranes, there are few reports on the development of such platforms.

One major achievement of the present thesis was to solve this issue by developing an integrated microfluidic chip capable of high-throughput formation of lipid bilayers and changing the buffers around them in a reversible manner. This was

only possible by introducing a complex interconnected network of various microfluidic channels having different roles (membrane channel, drug channel, resistance channels, bubble traps, side exits, *etc.*).

We implemented the developed drug-screening system to investigate how the candidate antibiotic azithromycin affects lipid bilayer membranes. In this study, we screened the influence of a low and high drug dosage on the mechanical properties of POPC model membranes. We observed that the drug reduced the membrane tension, tube extension force, and also forward/backward force-barriers in a dose-dependent manner. However, the bending rigidity was unaffected at low dose but slightly increased at high dose.

All in all, the developed platform holds potential as a reliable drug-screening tool for the high-throughput formation of membranes and characterization of the impact of drugs.

8.2 Recommendations for future work

Although the devices developed in this thesis provide a major step forwards in the field, they still have a couple of limitations that should be addressed in future work:

1. Above all, despite all the benefits of a planar membrane in vertical configuration with respect to the focal plane of a typical optical microscope, being planar makes membrane visualization technically very challenging. This becomes problematic, for instance, when direct observation of the full membrane is necessary like for membrane domain tracking or determination of the phase transition temperature.
2. Membrane tension depends on several parameters, and the cause(s) behind the measured changes in tension can be difficult to interpret in our system. Changes in tension are the result of various dynamic interconnected factors like changes in membrane area per lipid, the effectiveness of the lipid reservoir, lipid tail interactions with the channel surface, and many more. A more detailed study on the contribution and significance of each factor would help to better interpret and understand the calculated tension values on our setup.
3. One major limitation of the current work is the limited range of temperatures that can be applied to the samples in experiments involving optical tweezers. At the moment, the maximum possible temperature was 32 °C, to prevent thermal damage of the microscope objective. A better heating system should be designed

that can bring the membrane temperature to more relevant temperatures, ideally 37 °C to mimic body temperature.

4. Another uncertainty regarding the temperature control is that we do not know the exact temperature at the focal point of the optical trap when the trapped bead is being pushed against the membrane because the temperature is currently monitored via a thermocouple that is a few hundred microns away from the focal point. More precise characterizations are required to locally detect the exact temperature.

5. A setup combining optical tweezers with fluorescence microscope is required to check two critical points in the pushing experiment. First, to check if the curvature caused by the bead-membrane interaction causes any phase separation or lipid ordering at the contact point specifically for two-phase membranes and multi-lipid compositions. Secondly, to understand the lipid composition in the extended tube. One solution is to combine optical tweezers with fluorescence microscopy and use fluorescently-labeled lipids to form the bilayer. At the moment, we are not sure

about the lipid composition and its phase in the tubes that we pushed with the beads for membranes specifically with DOPC:DPPC lipid composition.

6. Some MD simulations on the lipid compositions we worked with in this thesis would give more insights in analyzing the experimental measurements specially for the tail-asymmetric lipid studies. There are some works in the literature ^{210, 220, 277} focusing on tail-asymmetric lipids but not with the exact same lipid compositions used in the present piece of work.

7. Various other experiments can be performed on the single gap design of Chapter 4. For instance, bilayers with asymmetric lipid compositions could be formed, or bilayers with asymmetric aqueous media as the *in vivo* condition is asymmetric regarding both the lipid composition and the inner/outer cell media. Also, since the single-gap design is compatible with chloroform, electrical measurements can be combined with optical tweezers-based experiments like membrane pushing to track physiological properties while the membranes are deformed and pushed with the optically trapped beads.

8. One classic challenge in the field of artificial cell membranes is the fact that we are not sure if the final composition of the fabricated membranes exactly follows the initial composition introduced into the chip dissolved in chloroform. Using labeled lipids and fluorescent microscopy might be a way to check for this.

9. On the multi-membrane-on-chip platform introduced in this thesis it is possible to form simultaneously two parallel membranes. It would be interesting to devise a strategy to connect the two membranes with open-ended lipid nanotubes. In this way, molecular transport through the lipid nanotube can be monitored which is biologically relevant to cell-cell communication.

In summary, the present thesis introduces designs and concepts that can pave the way for more complex lipid bilayer studies that were formerly not technically feasible. Such studies not only can help us better understand planar bilayers but, in general, artificial cell membranes.

References

1. Manni, M. M.; Tiberti, M. L.; Pagnotta, S.; Barelli, H.; Gautier, R.; Antonny, B., Acyl chain asymmetry and polyunsaturation of brain phospholipids facilitate membrane vesiculation without leakage. *Elife* **2018**, *7*, e34394.
2. Alberts, B.; Bray, D.; Hopkin, K.; Johnson, A. D.; Lewis, J.; Raff, M.; Roberts, K.; Walter, P., *Essential cell biology*. Garland Science: 2015.
3. Serrallach, E.; De Haas, G.; Shipley, G., Structure and thermotropic properties of mixed-chain phosphatidylcholine bilayer membranes. *Biochemistry* **1984**, *23* (4), 713-720.
4. Kelley, E. G.; Frewein, M. P.; Czakkel, O.; Nagao, M., Nanoscale bending dynamics in mixed-chain lipid membranes. *Symmetry* **2023**, *15* (1), 191.
5. Abraham, S.; Heckenthaler, T.; Morgenstern, Y.; Kaufman, Y., Effect of temperature on the structure, electrical resistivity, and charge capacitance of supported lipid bilayers. *Langmuir* **2019**, *35* (26), 8709-8715.
6. Fleury, J.-B.; Baulin, V. A., Microplastics destabilize lipid membranes by mechanical stretching. *Proceedings of the National Academy of Sciences* **2021**, *118* (31), e2104610118.
7. Panconi, L.; Lorenz, C. D.; May, R. C.; Owen, D. M.; Makarova, M., Phospholipid tail asymmetry allows cellular adaptation to anoxic environments. *Journal of Biological Chemistry* **2023**, *299* (9).
8. Cannon, B.; Heath, G.; Huang, J.; Somerharju, P.; Virtanen, J. A.; Cheng, K. H., Time-resolved fluorescence and fourier transform infrared spectroscopic investigations of lateral packing defects and superlattice domains in compositionally uniform cholesterol/phosphatidylcholine bilayers. *Biophysical journal* **2003**, *84* (6), 3777-3791.
9. Hui, S.; Mason, J.; Huang, C., Acyl chain interdigitation in saturated mixed-chain phosphatidylcholine bilayer dispersions. *Biochemistry* **1984**, *23* (23), 5570-5577.
10. Frewein, M. P.; Doktorova, M.; Heberle, F. A.; Scott, H. L.; Semeraro, E. F.; Porcar, L.; Pabst, G., Structure and interdigitation of chain-asymmetric phosphatidylcholines and milk sphingomyelin in the fluid phase. *Symmetry* **2021**, *13* (8), 1441.

11. Kure, J. L.; Andersen, C. B.; Rasmussen, T. E.; Lagerholm, B. C.; Arnspang, E. C., Defining the diffusion in model membranes using line fluorescence recovery after photobleaching. *Membranes* **2020**, *10* (12), 434.
12. Xu, C.; Hu, S.; Chen, X., Artificial cells: from basic science to applications. *Materials Today* **2016**, *19* (9), 516-532.
13. Fernandes, E.; Cardoso, V. F.; Lanceros-Méndez, S.; Lúcio, M., Lipid Microfluidic Biomimetic Models for Drug Screening: A Comprehensive Review. *Advanced Functional Materials* **2024**, 2315166.
14. Overeem, N. J.; Hamming, P. H.; Huskens, J., Time-Dependent Binding of Molecules and Nanoparticles at Receptor-Modified Supported Lipid Bilayer Gradients in a Microfluidic Device. *ChemistrySelect* **2020**, *5* (31), 9799-9805.
15. Griffo, A.; Sparn, C.; Lolicato, F.; Nolle, F.; Khangholi, N.; Seemann, R.; Fleury, J.-B.; Brinkmann, M.; Nickel, W.; Hahl, H., Mechanics of biomimetic free-standing lipid membranes: Insights on lipid chemistry and bilayer elasticity. *bioRxiv* **2023**, 2023.08. 21.554126.
16. Chien, P.-J.; Shih, Y.-L.; Cheng, C.-T.; Tu, H.-L., Chip assisted formation of phase-separated liposomes for reconstituting spatial protein–lipid interactions. *Lab on a Chip* **2022**, *22* (13), 2540-2548.
17. Fujiwara, S.; Shoji, K.; Watanabe, C.; Kawano, R.; Yanagisawa, M., Microfluidic formation of honeycomb-patterned droplets bounded by interface bilayers via bimodal molecular adsorption. *Micromachines* **2020**, *11* (7), 701.
18. Jönsson, P.; Jonsson, M. P.; Höök, F., Sealing of submicrometer wells by a shear-driven lipid bilayer. *Nano letters* **2010**, *10* (5), 1900-1906.
19. Beltramo, P. J.; Van Hooghten, R.; Vermant, J., Millimeter-area, free standing, phospholipid bilayers. *Soft Matter* **2016**, *12* (19), 4324-4331.
20. Amador, G. J.; Van Dijk, D.; Kieffer, R.; Aubin-Tam, M.-E.; Tam, D., Hydrodynamic shear dissipation and transmission in lipid bilayers. *Proceedings of the National Academy of Sciences* **2021**, *118* (21), e2100156118.
21. Dols-Perez, A.; Marin, V.; Amador, G. J.; Kieffer, R.; Tam, D.; Aubin-Tam, M.-E., Artificial cell membranes interfaced with optical tweezers: A versatile microfluidics platform for nanomanipulation and mechanical characterization. *ACS applied materials & interfaces* **2019**, *11* (37), 33620-33627.

22. Marin, V.; Kieffer, R.; Padmos, R.; Aubin-Tam, M.-E., Stable free-standing lipid bilayer membranes in Norland optical adhesive 81 microchannels. *Analytical chemistry* **2016**, *88* (15), 7466-7470.
23. Daillant, J.; Bellet-Amalric, E.; Braslau, A.; Charitat, T.; Fragneto, G.; Graner, F.; Mora, S.; Rieutord, F.; Stidder, B., Structure and fluctuations of a single floating lipid bilayer. *Proceedings of the National Academy of Sciences* **2005**, *102* (33), 11639-11644.
24. Connell, S. D.; Smith, D. A., The atomic force microscope as a tool for studying phase separation in lipid membranes. *Molecular membrane biology* **2006**, *23* (1), 17-28.
25. Mangiarotti, A.; Wilke, N., Energetics of the phase transition in free-standing versus supported lipid membranes. *The Journal of Physical Chemistry B* **2015**, *119* (28), 8718-8724.
26. Ogunyankin, M. O.; Torres, A.; Yaghmaie, F.; Longo, M. L., Lipid domain pixelation patterns imposed by e-beam fabricated substrates. *Langmuir* **2012**, *28* (18), 7107-7113.
27. Kaasgaard, T.; Leidy, C.; Crowe, J. H.; Mouritsen, O. G.; Jørgensen, K., Temperature-controlled structure and kinetics of ripple phases in one-and two-component supported lipid bilayers. *Biophysical journal* **2003**, *85* (1), 350-360.
28. Khangholi, N.; Seemann, R.; Fleury, J.-B., Simultaneous measurement of surface and bilayer tension in a microfluidic chip. *Biomicrofluidics* **2020**, *14* (2).
29. Heo, P.; Ramakrishnan, S.; Coleman, J.; Rothman, J. E.; Fleury, J. B.; Pincet, F., Highly Reproducible Physiological Asymmetric Membrane with Freely Diffusing Embedded Proteins in a 3D-Printed Microfluidic Setup. *Small* **2019**, *15* (21), 1900725.
30. Zabala-Ferrera, O.; Beltramo, P. J., Effects of Ion Concentration and Headgroup Chemistry on Thin Lipid Film Drainage. *Langmuir* **2023**, *39* (46), 16294-16302.
31. Zabala-Ferrera, O.; Liu, P.; Beltramo, P. J., Determining the Bending Rigidity of Free-Standing Planar Phospholipid Bilayers. *Membranes* **2023**, *13* (2), 129.
32. Scheidegger, L.; Stricker, L.; Beltramo, P. J.; Vermant, J., Domain Size Regulation in Phospholipid Model Membranes Using Oil Molecules and Hybrid Lipids. *The Journal of Physical Chemistry B* **2022**, *126* (31), 5842-5854.

33. Liu, P.; Zabala-Ferrera, O.; Beltramo, P. J., Fabrication and electromechanical characterization of freestanding asymmetric membranes. *Biophysical Journal* **2021**, *120* (9), 1755-1764.
34. Khangholi, N.; Finkler, M.; Seemann, R.; Ott, A.; Fleury, J.-B., Photoactivation of cell-free expressed archaerhodopsin-3 in a model cell membrane. *International Journal of Molecular Sciences* **2021**, *22* (21), 11981.
35. Salinas-Almaguer, S.; Mell, M.; Almendro-Vedia, V. G.; Calero, M.; Robledo-Sánchez, K. C. M.; Ruiz-Suarez, C.; Alarcón, T.; Barrio, R. A.; Hernández-Machado, A.; Monroy, F., Membrane rigidity regulates E. coli proliferation rates. *Scientific reports* **2022**, *12* (1), 933.
36. Masters, T. A.; Pontes, B.; Viasnoff, V.; Li, Y.; Gauthier, N. C., Plasma membrane tension orchestrates membrane trafficking, cytoskeletal remodeling, and biochemical signaling during phagocytosis. *Proceedings of the National Academy of Sciences* **2013**, *110* (29), 11875-11880.
37. Houk, A. R.; Jilkine, A.; Mejean, C. O.; Boltyanskiy, R.; Dufresne, E. R.; Angenent, S. B.; Altschuler, S. J.; Wu, L. F.; Weiner, O. D., Membrane tension maintains cell polarity by confining signals to the leading edge during neutrophil migration. *Cell* **2012**, *148* (1), 175-188.
38. Tsujita, K.; Takenawa, T.; Itoh, T., Feedback regulation between plasma membrane tension and membrane-bending proteins organizes cell polarity during leading edge formation. *Nature cell biology* **2015**, *17* (6), 749-758.
39. Bakhtiari, S.; Manshadi, M. K.; Candas, M.; Beskok, A., Changes in electrical capacitance of cell membrane reflect drug partitioning-induced alterations in lipid bilayer. *Micromachines* **2023**, *14* (2), 316.
40. Shendrik, P.; Golani, G.; Dharan, R.; Schwarz, U. S.; Sorkin, R., Membrane Tension Inhibits Lipid Mixing by Increasing the Hemifusion Stalk Energy. *ACS nano* **2023**, *17* (19), 18942-18951.
41. Goertz, M. P.; Goyal, N.; Montano, G. A.; Bunker, B. C., Lipid bilayer reorganization under extreme pH conditions. *Langmuir* **2011**, *27* (9), 5481-5491.
42. Pan, J.; Tristram-Nagle, S.; Kučerka, N.; Nagle, J. F., Temperature dependence of structure, bending rigidity, and bilayer interactions of dioleoylphosphatidylcholine bilayers. *Biophysical journal* **2008**, *94* (1), 117-124.
43. Bouvrais, H.; Duelund, L.; Ipsen, J. H., Buffers affect the bending rigidity of model lipid membranes. *Langmuir* **2014**, *30* (1), 13-16.

44. Fa, N.; Lins, L.; Courtoy, P. J.; Dufrêne, Y.; Van Der Smissen, P.; Bresseur, R.; Tyteca, D.; Mingeot-Leclercq, M.-P., Decrease of elastic moduli of DOPC bilayers induced by a macrolide antibiotic, azithromycin. *Biochimica et Biophysica Acta (BBA)-Biomembranes* **2007**, *1768* (7), 1830-1838.
45. Van Lehn, R. C.; Atukorale, P. U.; Carney, R. P.; Yang, Y.-S.; Stellacci, F.; Irvine, D. J.; Alexander-Katz, A., Effect of particle diameter and surface composition on the spontaneous fusion of monolayer-protected gold nanoparticles with lipid bilayers. *Nano letters* **2013**, *13* (9), 4060-4067.
46. Takei, T.; Yaguchi, T.; Fujii, T.; Nomoto, T.; Toyota, T.; Fujinami, M., Measurement of membrane tension of free standing lipid bilayers via laser-induced surface deformation spectroscopy. *Soft Matter* **2015**, *11* (44), 8641-8647.
47. Shitamichi, Y.; Ichikawa, M.; Kimura, Y., Mechanical properties of a giant liposome studied using optical tweezers. *Chemical Physics Letters* **2009**, *479* (4-6), 274-278.
48. Koster, G.; Cacciuto, A.; Derényi, I.; Frenkel, D.; Dogterom, M., Force barriers for membrane tube formation. *Physical review letters* **2005**, *94* (6), 068101.
49. Heinrich, M.; Tian, A.; Esposito, C.; Baumgart, T., Dynamic sorting of lipids and proteins in membrane tubes with a moving phase boundary. *Proceedings of the National Academy of Sciences* **2010**, *107* (16), 7208-7213.
50. Karimi, M.; Steinkühler, J.; Roy, D.; Dasgupta, R.; Lipowsky, R.; Dimova, R., Asymmetric ionic conditions generate large membrane curvatures. *Nano letters* **2018**, *18* (12), 7816-7821.
51. Spanke, H. T.; Agudo-Canalejo, J.; Tran, D.; Style, R. W.; Dufresne, E. R., Dynamics of spontaneous wrapping of microparticles by floppy lipid membranes. *Physical Review Research* **2022**, *4* (2), 023080.
52. Miller, E. J.; Phan, M. D.; Shah, J.; Honerkamp-Smith, A. R., Passive and reversible area regulation of supported lipid bilayers in response to fluid flow. *Biophysical Journal* **2023**, *122* (11), 2242-2255.
53. Färber, N.; Reitler, J.; Kamenac, A.; Westerhausen, C., Shear stress induced lipid order and permeability changes of giant unilamellar vesicles. *Biochimica et Biophysica Acta (BBA)-General Subjects* **2022**, *1866* (10), 130199.
54. Barlow, N. E.; Bolognesi, G.; Haylock, S.; Flemming, A. J.; Brooks, N. J.; Barter, L. M.; Ces, O., Rheological droplet interface bilayers (rheo-DIBs): Probing

the unstirred water layer effect on membrane permeability via spinning disk induced shear stress. *Scientific reports* **2017**, *7* (1), 17551.

55. Tero, R., Substrate effects on the formation process, structure and physicochemical properties of supported lipid bilayers. *Materials* **2012**, *5* (12), 2658-2680.

56. Kök, F. N.; Yildiz, A. A.; Inci, F., *Biomimetic lipid membranes: fundamentals, applications, and commercialization*. Springer: 2019.

57. Seddon, A. M.; Casey, D.; Law, R. V.; Gee, A.; Templer, R. H.; Ces, O., Drug interactions with lipid membranes. *Chemical Society Reviews* **2009**, *38* (9), 2509-2519.

58. Vrhovc, S.; Mally, M.; Kavčič, B.; Derganc, J., A microfluidic diffusion chamber for reversible environmental changes around flaccid lipid vesicles. *Lab on a Chip* **2011**, *11* (24), 4200-4206.

59. Khalifat, N.; Puff, N.; Bonneau, S.; Fournier, J.-B.; Angelova, M. I., Membrane deformation under local pH gradient: mimicking mitochondrial cristae dynamics. *Biophysical journal* **2008**, *95* (10), 4924-4933.

60. Azizi, M.; Davaji, B.; Nguyen, A. V.; Zhang, S.; Dogan, B.; Simpson, K. W.; Abbaspourrad, A., Gradient-based microfluidic platform for one single rapid antimicrobial susceptibility testing. *ACS sensors* **2021**, *6* (4), 1560-1571.

61. Nguyen, M. A.; Dinh, N. T.; Do Thi, M. H.; Nguyen Thi, D.; Pham, U. T.; Tran, T. Q.; Nguyen, V. M.; Le, N. H.; Nguyen, D. T.; Pham, D. T. N., Simple and Rapid Method of Microwell Array Fabrication for Drug Testing on 3D Cancer Spheroids. *ACS Omega* **2024**.

62. Nguyen, A. V.; Shourabi, A. Y.; Yaghoobi, M.; Zhang, S.; Simpson, K. W.; Abbaspourrad, A., A high-throughput integrated biofilm-on-a-chip platform for the investigation of combinatory physicochemical responses to chemical and fluid shear stress. *Plos one* **2022**, *17* (8), e0272294.

63. Shourabi, A. Y.; Kashaninejad, N.; Saidi, M. S., An integrated microfluidic concentration gradient generator for mechanical stimulation and drug delivery. *Journal of Science: Advanced Materials and Devices* **2021**, *6* (2), 280-290.

64. Ramadurai, S.; Sarangi, N. K.; Maher, S.; MacConnell, N.; Bond, A. M.; McDaid, D.; Flynn, D.; Keyes, T. E., Microcavity-Supported Lipid Bilayers; Evaluation of Drug-Lipid Membrane Interactions by Electrochemical Impedance and Fluorescence Correlation Spectroscopy. *Langmuir* **2019**, *35* (24), 8095-8109.

65. Barata, D.; van Blitterswijk, C.; Habibovic, P., High-throughput screening approaches and combinatorial development of biomaterials using microfluidics. *Acta biomaterialia* **2016**, *34*, 1-20.
66. Moffitt, J. R.; Chemla, Y. R.; Smith, S. B.; Bustamante, C., Recent advances in optical tweezers. *Annu. Rev. Biochem.* **2008**, *77* (1), 205-228.
67. Yang, Y.; Ren, Y.-X.; Chen, M.; Arita, Y.; Rosales-Guzmán, C., Optical trapping with structured light: a review. *Advanced Photonics* **2021**, *3* (3), 034001-034001.
68. Fazal, F. M.; Block, S. M., Optical tweezers study life under tension. *Nature photonics* **2011**, *5* (6), 318-321.
69. LaFratta, C. N., Optical tweezers for medical diagnostics. *Analytical and bioanalytical chemistry* **2013**, *405*, 5671-5677.
70. Zhu, Y.; You, M.; Shi, Y.; Huang, H.; Wei, Z.; He, T.; Xiong, S.; Wang, Z.; Cheng, X., Optofluidic tweezers: efficient and versatile micro/nano-manipulation tools. *Micromachines* **2023**, *14* (7), 1326.
71. Magazzù, A.; Marcuello, C., Investigation of soft matter nanomechanics by atomic force microscopy and optical tweezers: A comprehensive review. *Nanomaterials* **2023**, *13* (6), 963.
72. Jones, P.; Maragó, O.; Volpe, G., *Optical tweezers*. Cambridge University Press Cambridge: 2015.
73. Neuman, K. C.; Block, S. M., Optical trapping. *Review of scientific instruments* **2004**, *75* (9), 2787-2809.
74. Ghoddoosi Dehnavi, P.; Wei, D.; Aubin-Tam, M.; Tam, D., Optical Tweezers-based velocimetry: A method to measure microscale unsteady flows. *Experiments in Fluids: experimental methods and their applications to fluid flow* **2020**, *61* (9).
75. Joshi, V.; Goodwin, P. M.; Bowling, A., Power spectral density analysis of a scaled model simulation of an optical tweezer. *Optical Engineering* **2022**, *61* (10), 104103-104103.
76. Perkins, T. T., Optical traps for single molecule biophysics: a primer. *Laser & Photonics Reviews* **2009**, *3* (1-2), 203-220.
77. Jun, Y.; Tripathy, S. K.; Narayanareddy, B. R.; Mattson-Hoss, M. K.; Gross, S. P., Calibration of optical tweezers for in vivo force measurements: how do different approaches compare? *Biophysical journal* **2014**, *107* (6), 1474-1484.

78. Ambaum, M. H., *Thermal physics of the atmosphere*. Elsevier: 2020; Vol. 1.
79. Amador, G. J.; van Dijk, D.; Kieffer, R.; Aubin-Tam, M. E.; Tam, D., Hydrodynamic shear dissipation and transmission in lipid bilayers. *Proc Natl Acad Sci U S A* **2021**, *118* (21).
80. Yang, M.; Sun, N.; Luo, Y.; Lai, X.; Li, P.; Zhang, Z., Emergence of debubblers in microfluidics: A critical review. *Biomicrofluidics* **2022**, *16* (3), 031503.
81. Lochovsky, C.; Yasotharan, S.; Günther, A., Bubbles no more: in-plane trapping and removal of bubbles in microfluidic devices. *Lab on a Chip* **2012**, *12* (3), 595-601.
82. Wang, Y.; Lee, D.; Zhang, L.; Jeon, H.; Mendoza-Elias, J. E.; Harvat, T. A.; Hassan, S. Z.; Zhou, A.; Eddington, D. T.; Oberholzer, J., Systematic prevention of bubble formation and accumulation for long-term culture of pancreatic islet cells in microfluidic device. *Biomedical microdevices* **2012**, *14*, 419-426.
83. Blicher, A.; Wodzinska, K.; Fidorra, M.; Winterhalter, M.; Heimbürg, T., The temperature dependence of lipid membrane permeability, its quantized nature, and the influence of anesthetics. *Biophysical journal* **2009**, *96* (11), 4581-4591.
84. Ogishi, K.; Osaki, T.; Morimoto, Y.; Takeuchi, S., 3D printed microfluidic devices for lipid bilayer recordings. *Lab on a Chip* **2022**, *22* (5), 890-898.
85. Silvestrini, S.; Ferraro, D.; Tóth, T.; Pierno, M.; Carofiglio, T.; Mistura, G.; Maggini, M., Tailoring the wetting properties of thiolene microfluidic materials. *Lab on a Chip* **2012**, *12* (20), 4041-4043.
86. Wägli, P.; Homsy, A.; de Rooij, N. F., Norland optical adhesive (NOA81) microchannels with adjustable surface properties and high chemical resistance against IR-transparent organic solvents. *Procedia Engineering* **2010**, *5*, 460-463.
87. Catacutan, D. B.; Alexander, J.; Arnold, A.; Stokes, J. M., Machine learning in preclinical drug discovery. *Nature Chemical Biology* **2024**, *20* (8), 960-973.
88. Epanand, R. M.; Walker, C.; Epanand, R. F.; Magarvey, N. A., Molecular mechanisms of membrane targeting antibiotics. *Biochimica et Biophysica Acta (BBA)-Biomembranes* **2016**, *1858* (5), 980-987.
89. Buijs, N. P.; Matheson, E. J.; Cochrane, S. A.; Martin, N. I., Targeting membrane-bound bacterial cell wall precursors: a tried and true antibiotic

- strategy in nature and the clinic. *Chemical Communications* **2023**, 59 (50), 7685-7703.
90. Delcour, A. H., Outer membrane permeability and antibiotic resistance. *Biochimica et Biophysica Acta (BBA)-Proteins and Proteomics* **2009**, 1794 (5), 808-816.
91. Marín-Medina, N.; Ramírez, D. A.; Trier, S.; Leidy, C., Mechanical properties that influence antimicrobial peptide activity in lipid membranes. *Applied microbiology and biotechnology* **2016**, 100, 10251-10263.
92. Kresák, S.; Hianik, T.; Naumann, R. L., Giga-seal solvent-free bilayer lipid membranes: from single nanopores to nanopore arrays. *Soft Matter* **2009**, 5 (20), 4021-4032.
93. Ronen, R.; Kaufman, Y.; Freger, V., Formation of pore-spanning lipid membrane and cross-membrane water and ion transport. *Journal of Membrane Science* **2017**, 523, 247-254.
94. Azizi, M.; Nguyen, A. V.; Dogan, B.; Zhang, S.; Simpson, K. W.; Abbaspourrad, A., Antimicrobial susceptibility testing in a rapid single test via an egg-like multivolume microchamber-based microfluidic platform. *ACS Applied Materials & Interfaces* **2021**, 13 (17), 19581-19592.
95. Ju, F. N.; Kim, C.-H.; Lee, K.-H.; Kim, C.-D.; Lim, J.; Lee, T.; Park, C. G.; Kim, T.-H., Gold nanostructure-integrated conductive microwell arrays for uniform cancer spheroid formation and electrochemical drug screening. *Biosensors and Bioelectronics* **2023**, 222, 115003.
96. Sebaaly, C.; Greige-Gerges, H.; Charcosset, C., Lipid membrane models for biomembrane properties' investigation. In *Current trends and future developments on (bio-) membranes*, Elsevier: 2019; pp 311-340.
97. Zheng, X. T.; Yu, L.; Li, P.; Dong, H.; Wang, Y.; Liu, Y.; Li, C. M., On-chip investigation of cell–drug interactions. *Advanced drug delivery reviews* **2013**, 65 (11-12), 1556-1574.
98. Mally, M.; Božič, B.; Hartman, S. V.; Klančnik, U.; Mur, M.; Svetina, S.; Derganc, J., Controlled shaping of lipid vesicles in a microfluidic diffusion chamber. *RSC advances* **2017**, 7 (58), 36506-36515.
99. Fleury, J.-B.; Baulin, V. A., Aging affects the mechanical interaction between microplastics and lipid bilayers. *The Journal of Chemical Physics* **2024**, 161 (14).

100. Zagnoni, M.; Sandison, M. E.; Marius, P.; Lee, A. G.; Morgan, H., Controlled delivery of proteins into bilayer lipid membranes on chip. *Lab on a Chip* **2007**, *7* (9), 1176-1183.
101. Kawano, R.; Osaki, T.; Sasaki, H.; Takeuchi, S., A polymer-based nanopore-integrated microfluidic device for generating stable bilayer lipid membranes. *Small* **2010**, *6* (19), 2100-2104.
102. Shourabi, A. Y.; Kieffer, R.; de Jong, D.; Tam, D.; Aubin-Tam, M.-E., Mechanical characterization of freestanding lipid bilayers with temperature-controlled phase. *Soft Matter* **2024**.
103. Yahyazadeh Shourabi, A.; Salajeghe, R.; Barisam, M.; Kashaninejad, N., A Proof-of-Concept Study Using Numerical Simulations of an Acoustic Spheroid-on-a-Chip Platform for Improving 3D Cell Culture. *Sensors* **2021**, *21* (16), 5529.
104. Westein, E.; van der Meer, A. D.; Kuijpers, M. J.; Frimat, J.-P.; van den Berg, A.; Heemskerk, J. W., Atherosclerotic geometries exacerbate pathological thrombus formation poststenosis in a von Willebrand factor-dependent manner. *Proceedings of the National Academy of Sciences* **2013**, *110* (4), 1357-1362.
105. Ebadi, M.; Moshksayan, K.; Kashaninejad, N.; Saidi, M. S.; Nguyen, N.-T., A tool for designing tree-like concentration gradient generators for lab-on-a-chip applications. *Chemical Engineering Science* **2020**, *212*, 115339.
106. Shao, C.; Kendall, E. L.; DeVoe, D. L., Electro-optical BLM chips enabling dynamic imaging of ordered lipid domains. *Lab on a Chip* **2012**, *12* (17), 3142-3149.
107. Ensslen, T.; Behrends, J. C., A chip-based array for high-resolution fluorescence characterization of free-standing horizontal lipid membranes under voltage clamp. *Lab on a Chip* **2022**, *22* (15), 2902-2910.
108. Khangholi, N.; Seemann, R.; Fleury, J.-B., Simultaneous measurement of surface and bilayer tension in a microfluidic chip. *Biomicrofluidics* **2020**, *14* (2), 024117.
109. Nguyen, M.-A.; Srijanto, B.; Collier, C. P.; Retterer, S. T.; Sarles, S. A., Hydrodynamic trapping for rapid assembly and in situ electrical characterization of droplet interface bilayer arrays. *Lab on a Chip* **2016**, *16* (18), 3576-3588.
110. El-Beyrouthy, J.; Freeman, E., Characterizing the structure and interactions of model lipid membranes using electrophysiology. *Membranes* **2021**, *11* (5), 319.

111. Strutt, R.; Sheffield, F.; Barlow, N. E.; Flemming, A. J.; Harling, J. D.; Law, R. V.; Brooks, N. J.; Barter, L. M.; Ces, O., UV-DIB: label-free permeability determination using droplet interface bilayers. *Lab on a Chip* **2022**, *22* (5), 972-985.
112. Venkatesan, G. A.; Sarles, S. A., Droplet immobilization within a polymeric organogel improves lipid bilayer durability and portability. *Lab on a Chip* **2016**, *16* (11), 2116-2125.
113. Amador, G. J.; van Dijk, D.; Kieffer, R.; Aubin-Tam, M.-E.; Tam, D., Hydrodynamic shear dissipation and transmission in lipid bilayers. *Proc. Natl. Acad. Sci. U.S. A.* **2021**, *118* (21).
114. Yahyazadeh Shourabi, A.; Kieffer, R.; de Jong, D.; Tam, D.; Aubin-Tam, M.-E., Mechanical characterization of freestanding lipid bilayers with temperature-controlled phase. *Soft Matter* **2024**, *20* (42), 8524-8537.
115. Czekalska, M. A.; Kaminski, T. S.; Jakiela, S.; Sapra, K. T.; Bayley, H.; Garstecki, P., A droplet microfluidic system for sequential generation of lipid bilayers and transmembrane electrical recordings. *Lab on a Chip* **2015**, *15* (2), 541-548.
116. Rhee, M.; Light, Y. K.; Yilmaz, S.; Adams, P. D.; Saxena, D.; Meagher, R. J.; Singh, A. K., Pressure stabilizer for reproducible picoinjection in droplet microfluidic systems. *Lab on a Chip* **2014**, *14* (23), 4533-4539.
117. Södergren, S.; Svensson, K.; Hjort, K., Microfluidic active pressure and flow stabiliser. *Scientific reports* **2021**, *11* (1), 1-9.
118. Xiang, N.; Han, Y.; Jia, Y.; Shi, Z.; Yi, H.; Ni, Z., Flow stabilizer on a syringe tip for hand-powered microfluidic sample injection. *Lab on a Chip* **2019**, *19* (2), 214-222.
119. Lee, J.; Rahman, F.; Laoui, T.; Karnik, R., Bubble-induced damping in displacement-driven microfluidic flows. *Physical Review E* **2012**, *86* (2), 026301.
120. Wu, J.; Kumar-Kanojia, A.; Hombach-Klonisch, S.; Klonisch, T.; Lin, F., A radial microfluidic platform for higher throughput chemotaxis studies with individual gradient control. *Lab on a Chip* **2018**, *18* (24), 3855-3864.
121. Korner, J. L.; Stephenson, E. B.; Elvira, K. S., A bespoke microfluidic pharmacokinetic compartment model for drug absorption using artificial cell membranes. *Lab on a Chip* **2020**, *20* (11), 1898-1906.

122. Park, J. Y.; Kim, S.-K.; Woo, D.-H.; Lee, E.-J.; Kim, J.-H.; Lee, S.-H., Differentiation of neural progenitor cells in a microfluidic chip-generated cytokine gradient. *Stem cells* **2009**, *27* (11), 2646-2654.
123. Saadi, W.; Rhee, S. W.; Lin, F.; Vahidi, B.; Chung, B. G.; Jeon, N. L., Generation of stable concentration gradients in 2D and 3D environments using a microfluidic ladder chamber. *Biomedical microdevices* **2007**, *9*, 627-635.
124. Andrieux, S.; Muller, P.; Kaushal, M.; Vera, N. S. M.; Bollache, R.; Honorez, C.; Cagna, A.; Drenckhan, W., Microfluidic thin film pressure balance for the study of complex thin films. *Lab on a Chip* **2021**, *21* (2), 412-420.
125. Chatzigiannakis, E.; Veenstra, P.; Ten Bosch, D.; Vermant, J., Mimicking coalescence using a pressure-controlled dynamic thin film balance. *Soft Matter* **2020**, *16* (41), 9410-9422.
126. Araci, I. E.; Agaoglu, S.; Lee, J. Y.; Yepes, L. R.; Diep, P.; Martini, M.; Schmidt, A., Flow stabilization in wearable microfluidic sensors enables noise suppression. *Lab on a Chip* **2019**, *19* (22), 3899-3908.
127. Luo, Y.; Huang, Y.; Li, Y.; Duan, X.; Jiang, Y.; Wang, C.; Fang, J.; Xi, L.; Nguyen, N.-T.; Song, C., Dispersive phase microscopy incorporated with droplet-based microfluidics for biofactory-on-a-chip. *Lab on a Chip* **2023**.
128. Gao, Y.; Sun, J.; Lin, W.-H.; Webb, D. J.; Li, D., A compact microfluidic gradient generator using passive pumping. *Microfluidics and nanofluidics* **2012**, *12*, 887-895.
129. O'Connell, K. C.; Landers, J. P., Integrated membranes within centrifugal microfluidic devices: a review. *Lab on a Chip* **2023**.
130. Wu, J.; Tomsa, D.; Zhang, M.; Komenda, P.; Tangri, N.; Rigatto, C.; Lin, F., A passive mixing microfluidic urinary albumin chip for chronic kidney disease assessment. *ACS sensors* **2018**, *3* (10), 2191-2197.
131. Tazin, N.; Patel, D.; Lambert, C. J.; Shad, M. H.; Campbell, J.; Gale, B. K., Automated passive serial dilution microfluidic chip for calcium quantification based on the Arsenazo III method. *Sensors & Diagnostics* **2022**, *1* (4), 810-820.
132. Tice, J. D.; Desai, A. V.; Bassett, T. A.; Apblett, C. A.; Kenis, P. J., Control of pressure-driven components in integrated microfluidic devices using an on-chip electrostatic microvalve. *RSC Advances* **2014**, *4* (93), 51593-51602.

133. Atencia, J.; Morrow, J.; Locascio, L. E., The microfluidic palette: a diffusive gradient generator with spatio-temporal control. *Lab on a Chip* **2009**, *9* (18), 2707-2714.
134. Gao, Y.; Sun, J.; Lin, W.-H.; Webb, D. J.; Li, D., A compact microfluidic gradient generator using passive pumping. *Microfluidics and nanofluidics* **2012**, *12* (6), 887-895.
135. Mo, J.; Ding, Y.; Zhu, S.; Kuang, P.; Shen, L.; Xiang, N.; Sha, J.; Chen, Y., Passive microscopic fluidic diodes using asymmetric channels. *AIP Advances* **2019**, *9* (8).
136. Cho, H.; Kimteng, A.; Lee, L. P., BIOLOGICALLY INSPIRED BIDIRECTIONAL FLUIDIC DIODE.
137. Sweet, E.; Mehta, R.; Xu, Y.; Jew, R.; Lin, R.; Lin, L., Finger-powered fluidic actuation and mixing via MultiJet 3D printing. *Lab on a Chip* **2020**, *20* (18), 3375-3385.
138. Li, Z.; Liu, C.; Sun, J., Hydraulic–electric analogy for design and operation of microfluidic systems. *Lab on a Chip* **2023**.
139. Jain, R.; Lutz, B., Frequency tuning allows flow direction control in microfluidic networks with passive features. *Lab on a Chip* **2017**, *17* (9), 1552-1558.
140. Xia, H.; Wu, J.; Zheng, J.; Zhang, J.; Wang, Z., Nonlinear microfluidics: device physics, functions, and applications. *Lab on a Chip* **2021**, *21* (7), 1241-1268.
141. Geczy, R.; Sticker, D.; Bovet, N.; Häfeli, U. O.; Kutter, J. P., Chloroform compatible, thiol-ene based replica molded micro chemical devices as an alternative to glass microfluidic chips. *Lab on a Chip* **2019**, *19* (5), 798-806.
142. Maček Lebar, A.; Miklavčič, D.; Kotulska, M.; Kramar, P., Water pores in planar lipid bilayers at fast and slow rise of transmembrane voltage. *Membranes* **2021**, *11* (4), 263.
143. Gross, L. C.; Heron, A. J.; Baca, S. C.; Wallace, M. I., Determining membrane capacitance by dynamic control of droplet interface bilayer area. *Langmuir* **2011**, *27* (23), 14335-14342.
144. Ardham, V. R.; Zoni, V.; Adamowicz, S.; Campomanes, P.; Vanni, S., Accurate estimation of membrane capacitance from atomistic molecular dynamics simulations of zwitterionic lipid bilayers. *The Journal of Physical Chemistry B* **2020**, *124* (38), 8278-8286.

145. Freeman, E.; Najem, J.; Sukharev, S.; Philen, M.; Leo, D., The mechanoelectrical response of droplet interface bilayer membranes. *Soft matter* **2016**, *12* (12), 3021-3031.
146. Gohrbandt, M.; Lipski, A.; Grimshaw, J. W.; Buttress, J. A.; Baig, Z.; Herkenhoff, B.; Walter, S.; Kurre, R.; Deckers-Hebestreit, G.; Strahl, H., Low membrane fluidity triggers lipid phase separation and protein segregation in living bacteria. *The EMBO journal* **2022**, *41* (5), e109800.
147. Yang, S.; Kiessling, V.; Tamm, L., Line tension at lipid phase boundaries as driving force for HIV fusion peptide-mediated fusion. *Nat Commun* **7**: 11401. 2016.
148. Stone, M. B.; Shelby, S. A.; Núñez, M. F.; Wisser, K.; Veatch, S. L., Protein sorting by lipid phase-like domains supports emergent signaling function in B lymphocyte plasma membranes. *elife* **2017**, *6*, e19891.
149. Veatch, S. L.; Keller, S. L., Seeing spots: complex phase behavior in simple membranes. *Biochimica et Biophysica Acta (BBA)-Molecular Cell Research* **2005**, *1746* (3), 172-185.
150. Akabori, K.; Nagle, J. F., Structure of the DMPC lipid bilayer ripple phase. *Soft matter* **2015**, *11* (5), 918-926.
151. Peetla, C.; Stine, A.; Labhasetwar, V., Biophysical interactions with model lipid membranes: applications in drug discovery and drug delivery. *Molecular pharmaceuticals* **2009**, *6* (5), 1264-1276.
152. Scheidegger, L.; Stricker, L.; Beltramo, P. J.; Vermant, J., Domain Size Regulation in Phospholipid Model Membranes Using Oil Molecules and Hybrid Lipids. *The Journal of Physical Chemistry B* **2022**.
153. Davies, M.; Reyes-Figueroa, A.; Gurtovenko, A. A.; Frankel, D.; Karttunen, M., Elucidating lipid conformations in the ripple phase: Machine learning reveals four lipid populations. *Biophysical Journal* **2023**, *122* (2), 442-450.
154. Heimburg, T., Mechanical aspects of membrane thermodynamics. Estimation of the mechanical properties of lipid membranes close to the chain melting transition from calorimetry. *Biochimica et Biophysica Acta (BBA)-Biomembranes* **1998**, *1415* (1), 147-162.
155. Chen, D.; Santore, M. M., Large effect of membrane tension on the fluid–solid phase transitions of two-component phosphatidylcholine vesicles. *Proceedings of the national academy of sciences* **2014**, *111* (1), 179-184.

156. Bernchou, U.; Midtby, H.; Ipsen, J. H.; Simonsen, A. C., Correlation between the ripple phase and stripe domains in membranes. *Biochimica et Biophysica Acta (BBA)-Biomembranes* **2011**, *1808* (12), 2849-2858.
157. Zasadzinski, J.; Schneider, M., Ripple wavelength, amplitude, and configuration in lyotropic liquid crystals as a function of effective headgroup size. *Journal de Physique* **1987**, *48* (11), 2001-2011.
158. Tada, K.; Miyazaki, E.; Goto, M.; Tamai, N.; Matsuki, H.; Kaneshina, S., Barotropic and thermotropic bilayer phase behavior of positional isomers of unsaturated mixed-chain phosphatidylcholines. *Biochimica et Biophysica Acta (BBA)-Biomembranes* **2009**, *1788* (5), 1056-1063.
159. Du, K.; Sun, L.; Luo, Z.; Cao, Y.; Sun, Q.; Zhang, K.; Faizy, A.; Piomelli, D.; Lu, X.; Shan, J., Reduced DMPC and PMPC in lung surfactant promote SARS-CoV-2 infection in obesity. *Metabolism* **2022**, *131*, 155181.
160. Nickels, J. D.; Smith, M. D.; Alsop, R. J.; Himbert, S.; Yahya, A.; Corder, D.; Zolnierczuk, P.; Stanley, C. B.; Katsaras, J.; Cheng, X., Lipid rafts: buffers of cell membrane physical properties. *The Journal of Physical Chemistry B* **2019**, *123* (9), 2050-2056.
161. Betaneli, V.; Worch, R.; Schwille, P., Effect of temperature on the formation of liquid phase-separating giant unilamellar vesicles (GUV). *Chemistry and physics of lipids* **2012**, *165* (6), 630-637.
162. Yoon, Y. Z.; Hale, J. P.; Petrov, P. G.; Cicuta, P., Mechanical properties of ternary lipid membranes near a liquid-liquid phase separation boundary. *Journal of Physics: Condensed Matter* **2010**, *22* (6), 062101.
163. Shimokawa, N.; Nagata, M.; Takagi, M., Physical properties of the hybrid lipid POPC on micrometer-sized domains in mixed lipid membranes. *Physical Chemistry Chemical Physics* **2015**, *17* (32), 20882-20888.
164. Chen, D.; Santore, M. M., Hybrid copolymer-phospholipid vesicles: phase separation resembling mixed phospholipid lamellae, but with mechanical stability and control. *Soft Matter* **2015**, *11* (13), 2617-2626.
165. Bassereau, P.; Jin, R.; Baumgart, T.; Deserno, M.; Dimova, R.; Frolov, V. A.; Bashkurov, P. V.; Grubmüller, H.; Jahn, R.; Risselada, H. J., The 2018 biomembrane curvature and remodeling roadmap. *Journal of physics D: Applied physics* **2018**, *51* (34), 343001.

166. Thottacherry, J. J.; Kosmalska, A. J.; Kumar, A.; Vishen, A. S.; Elosegui-Artola, A.; Pradhan, S.; Sharma, S.; Singh, P. P.; Guadamillas, M. C.; Chaudhary, N., Mechanochemical feedback control of dynamin independent endocytosis modulates membrane tension in adherent cells. *Nature communications* **2018**, *9* (1), 4217.
167. Dinet, C.; Torres-Sánchez, A.; Lanfranco, R.; Di Michele, L.; Arroyo, M.; Staykova, M., Patterning and dynamics of membrane adhesion under hydraulic stress. *Nature Communications* **2023**, *14* (1), 7445.
168. Miller, E. J.; Ratajczak, A. M.; Anthony, A. A.; Mottau, M.; Gonzalez, X. I. R.; Honerkamp-Smith, A. R., Divide and conquer: How phase separation contributes to lateral transport and organization of membrane proteins and lipids. *Chemistry and Physics of Lipids* **2020**, *233*, 104985.
169. Roffay, C.; Molinard, G.; Kim, K.; Urbanska, M.; Andrade, V.; Barbarasa, V.; Nowak, P.; Mercier, V.; García-Calvo, J.; Matile, S., Passive coupling of membrane tension and cell volume during active response of cells to osmosis. *Proceedings of the National Academy of Sciences* **2021**, *118* (47), e2103228118.
170. Yamamoto, K.; Ando, J., Endothelial cell and model membranes respond to shear stress by rapidly decreasing the order of their lipid phases. *Journal of cell science* **2013**, *126* (5), 1227-1234.
171. Boycott, H. E.; Barbier, C. S.; Eichel, C. A.; Costa, K. D.; Martins, R. P.; Louault, F.; Dilanian, G.; Coulombe, A.; Hatem, S. N.; Balse, E., Shear stress triggers insertion of voltage-gated potassium channels from intracellular compartments in atrial myocytes. *Proceedings of the National Academy of Sciences* **2013**, *110* (41), E3955-E3964.
172. Cross, B.; Steinberger, A.; Cottin-Bizonne, C.; Rieu, J.-P.; Charlaix, E., Boundary flow of water on supported phospholipid films. *Europhysics Letters* **2006**, *73* (3), 390.
173. White, C. R.; Frangos, J. A., The shear stress of it all: the cell membrane and mechanochemical transduction. *Philosophical Transactions of the Royal Society B: Biological Sciences* **2007**, *362* (1484), 1459-1467.
174. Rappel, W.-J.; Edelstein-Keshet, L., Mechanisms of cell polarization. *Current opinion in systems biology* **2017**, *3*, 43-53.
175. Zurzolo, C., Tunneling nanotubes: Reshaping connectivity. *Current opinion in cell biology* **2021**, *71*, 139-147.

176. Nagle, J. F.; Jablin, M. S.; Tristram-Nagle, S.; Akabori, K., What are the true values of the bending modulus of simple lipid bilayers? *Chemistry and physics of lipids* **2015**, *185*, 3-10.
177. Dimova, R., Recent developments in the field of bending rigidity measurements on membranes. *Advances in colloid and interface science* **2014**, *208*, 225-234.
178. Yandrapalli, N.; Petit, J.; Bäumchen, O.; Robinson, T., Surfactant-free production of biomimetic giant unilamellar vesicles using PDMS-based microfluidics. *Communications Chemistry* **2021**, *4* (1), 100.
179. Deshpande, S.; Caspi, Y.; Meijering, A. E.; Dekker, C., Octanol-assisted liposome assembly on chip. *Nature communications* **2016**, *7* (1), 10447.
180. Parthasarathy, R.; Yu, C.-h.; Groves, J. T., Curvature-modulated phase separation in lipid bilayer membranes. *Langmuir* **2006**, *22* (11), 5095-5099.
181. Noguchi, H., Nonequilibrium Membrane Dynamics Induced by Active Protein Interactions and Chemical Reactions: A Review. *ChemSystemsChem* **2024**, e202400042.
182. Blosser, M. C.; Horst, B. G.; Keller, S. L., cDICE method produces giant lipid vesicles under physiological conditions of charged lipids and ionic solutions. *Soft matter* **2016**, *12* (35), 7364-7371.
183. Van de Cauter, L.; Jawale, Y. K.; Tam, D.; Baldauf, L.; van Buren, L.; Koenderink, G. H.; Dogterom, M.; Ganzinger, K. A., High-speed imaging of giant unilamellar vesicle formation in cDICE. *bioRxiv* **2023**, 2023.10.13.562183.
184. Baldauf, L.; Frey, F.; Perez, M. A.; Idema, T.; Koenderink, G. H., Branched actin cortices reconstituted in vesicles sense membrane curvature. *Biophysical journal* **2023**, *122* (11), 2311-2324.
185. Yu, Z.; Baptist, A. V.; Reinhardt, S. C.; Bertolin, E.; Dekker, C.; Jungmann, R.; Heuer-Jungemann, A.; Caneva, S., Compliant DNA Origami Nanoactuators as Size-Selective Nanopores. *Advanced Materials* **2024**, 2405104.
186. Keough, K.; Davis, P., Gel to liquid-crystalline phase transitions in water dispersions of saturated mixed-acid phosphatidylcholines. *Biochemistry* **1979**, *18* (8), 1453-1459.
187. Chen, D.; Santore, M. M., Three dimensional (temperature–tension–composition) phase map of mixed DOPC–DPPC vesicles: Two solid phases and a

- fluid phase coexist on three intersecting planes. *Biochimica et Biophysica Acta (BBA)-Biomembranes* **2014**, *1838* (11), 2788-2797.
188. Leirer, C.; Wunderlich, B.; Myles, V.; Schneider, M. F., Phase transition induced fission in lipid vesicles. *Biophysical chemistry* **2009**, *143* (1-2), 106-109.
189. Faxén, H., Der Widerstand gegen die Bewegung einer starren Kugel in einer zähen Flüssigkeit, die zwischen zwei parallelen ebenen Wänden eingeschlossen ist. *Annalen der Physik* **1922**, *373* (10), 89-119.
190. Rallabandi, B.; Oppenheimer, N.; Ben Zion, M. Y.; Stone, H. A., Membrane-induced hydroelastic migration of a particle surfing its own wave. *Nature Physics* **2018**, *14* (12), 1211-1215.
191. Dimova, R.; Pouligny, B.; Dietrich, C., Pretransitional effects in dimyristoylphosphatidylcholine vesicle membranes: optical dynamometry study. *Biophysical Journal* **2000**, *79* (1), 340-356.
192. Dimova, R.; Dietrich, C.; Hadjiisky, A.; Danov, K.; Pouligny, B., Falling ball viscosimetry of giant vesicle membranes: finite-size effects. *The European Physical Journal B-Condensed Matter and Complex Systems* **1999**, *12*, 589-598.
193. Gambin, Y.; Lopez-Esparza, R.; Reffay, M.; Sierecki, E.; Gov, N.; Genest, M.; Hodges, R.; Urbach, W., Lateral mobility of proteins in liquid membranes revisited. *Proceedings of the National Academy of Sciences* **2006**, *103* (7), 2098-2102.
194. Chwastek, G.; Petrov, E. P.; Sáenz, J. P., A Method for High-Throughput Measurements of Viscosity in Sub-micrometer-Sized Membrane Systems. *ChemBioChem* **2020**, *21* (6), 836-844.
195. Griffo, A.; Sparn, C.; Lolicato, F.; Nolle, F.; Khangholi, N.; Seemann, R.; Fleury, J.-B.; Brinkmann, M.; Nickel, W.; Hähl, H., Mechanics of biomimetic free-standing lipid membranes: insights into the elasticity of complex lipid compositions. *RSC advances* **2024**, *14* (19), 13044-13052.
196. Anishkin, A.; Loukin, S. H.; Teng, J.; Kung, C., Feeling the hidden mechanical forces in lipid bilayer is an original sense. *Proceedings of the National Academy of Sciences* **2014**, *111* (22), 7898-7905.
197. Koster, G.; VanDuijn, M.; Hofs, B.; Dogterom, M., Membrane tube formation from giant vesicles by dynamic association of motor proteins. *Proceedings of the National Academy of Sciences* **2003**, *100* (26), 15583-15588.
198. Derényi, I.; Jülicher, F.; Prost, J., Formation and interaction of membrane tubes. *Physical review letters* **2002**, *88* (23), 238101.

199. Armond, J. W.; Macpherson, J. V.; Turner, M. S., Pulling nanotubes from supported bilayers. *Langmuir* **2011**, *27* (13), 8269-8274.
200. Jahnke, K.; Maurer, S. J.; Weber, C.; Bücher, J. E. H.; Schoenit, A.; D'Este, E.; Cavalcanti-Adam, E. A.; Göpfrich, K., Actomyosin-Assisted Pulling of Lipid Nanotubes from Lipid Vesicles and Cells. *Nano Letters* **2022**, *22* (3), 1145-1150.
201. Lyatskaya, Y.; Liu, Y.; Tristram-Nagle, S.; Katsaras, J.; Nagle, J. F., Method for obtaining structure and interactions from oriented lipid bilayers. *Physical Review E* **2000**, *63* (1), 011907.
202. Drabik, D.; Chodaczek, G.; Kraszewski, S.; Langner, M., Mechanical properties determination of DMPC, DPPC, DSPC, and HSPC solid-ordered bilayers. *Langmuir* **2020**, *36* (14), 3826-3835.
203. Lee, C.-H.; Lin, W.-C.; Wang, J., All-optical measurements of the bending rigidity of lipid-vesicle membranes across structural phase transitions. *Physical Review E* **2001**, *64* (2), 020901.
204. Wu, H.-L.; Tsao, H.-K.; Sheng, Y.-J., Dynamic and mechanical properties of supported lipid bilayers. *The Journal of chemical physics* **2016**, *144* (15), 154904.
205. Huang, C., Mixed-chain phospholipids and interdigitated bilayer systems. *Klinische Wochenschrift* **1990**, *68*, 149-165.
206. Reinhard, J.; Mattes, C.; Väh, K.; Radanović, T.; Surma, M. A.; Klose, C.; Ernst, R., A quantitative analysis of cellular lipid compositions during acute proteotoxic ER stress reveals specificity in the production of asymmetric lipids. *Frontiers in Cell and Developmental Biology* **2020**, *8*, 756.
207. Ali, S.; Smaby, J. M.; Momsen, M. M.; Brockman, H. L.; Brown, R. E., Acyl chain-length asymmetry alters the interfacial elastic interactions of phosphatidylcholines. *Biophysical journal* **1998**, *74* (1), 338-348.
208. Evans, E.; Needham, D., Physical properties of surfactant bilayer membranes: thermal transitions, elasticity, rigidity, cohesion and colloidal interactions. *Journal of Physical Chemistry* **1987**, *91* (16), 4219-4228.
209. Jiang, H.; Powers, T. R., Curvature-driven lipid sorting in a membrane tubule. *Physical review letters* **2008**, *101* (1), 018103.
210. Smith, P.; Owen, D. M.; Lorenz, C. D.; Makarova, M., Asymmetric glycerophospholipids impart distinctive biophysical properties to lipid bilayers. *Biophysical Journal* **2021**, *120* (9), 1746-1754.

211. Sharma, V. K.; Sarwa, K. K.; Mazumder, B., Fluidity enhancement: a critical factor for performance of liposomal transdermal drug delivery system. *Journal of liposome research* **2014**, *24* (2), 83-89.
212. Bodratti, A. M.; Alexandridis, P., Amphiphilic block copolymers in drug delivery: Advances in formulation structure and performance. *Expert opinion on drug delivery* **2018**, *15* (11), 1085-1104.
213. Frewein, M. P.; Piller, P.; Semeraro, E. F.; Batchu, K. C.; Heberle, F. A.; Scott, H. L.; Gerelli, Y.; Porcar, L.; Pabst, G., Interdigitation-Induced Order and Disorder in Asymmetric Membranes. *The Journal of Membrane Biology* **2022**, *255* (4-5), 407-421.
214. Kaino, T.; Tonoko, K.; Mochizuki, S.; Takashima, Y.; Kawamukai, M., Schizosaccharomyces japonicus has low levels of CoQ10 synthesis, respiration deficiency, and efficient ethanol production. *Bioscience, biotechnology, and biochemistry* **2018**, *82* (6), 1031-1042.
215. Makarova, M.; Peter, M.; Balogh, G.; Glatz, A.; MacRae, J. I.; Mora, N. L.; Booth, P.; Makeyev, E.; Vigh, L.; Oliferenko, S., Delineating the rules for structural adaptation of membrane-associated proteins to evolutionary changes in membrane lipidome. *Current Biology* **2020**, *30* (3), 367-380. e8.
216. Kučerka, N.; Nieh, M.-P.; Katsaras, J., Fluid phase lipid areas and bilayer thicknesses of commonly used phosphatidylcholines as a function of temperature. *Biochimica et Biophysica Acta (BBA)-Biomembranes* **2011**, *1808* (11), 2761-2771.
217. Goto, M.; Ishida, S.; Tamai, N.; Matsuki, H.; Kaneshina, S., Chain asymmetry alters thermotropic and barotropic properties of phospholipid bilayer membranes. *Chemistry and physics of lipids* **2009**, *161* (2), 65-76.
218. Swaney, J. B.; Chang, B. C., Thermal dependence of apolipoprotein AI/phospholipid recombination. *Biochemistry* **1980**, *19* (24), 5637-5644.
219. Mattai, J.; Sripada, P.; Shipley, G., Mixed-chain phosphatidylcholine bilayers: structure and properties. *Biochemistry* **1987**, *26* (12), 3287-3297.
220. Illya, G.; Lipowsky, R.; Shillcock, J., Effect of chain length and asymmetry on material properties of bilayer membranes. *The Journal of chemical physics* **2005**, *122* (24), 244901.
221. Garvey, C. J.; Bryant, S. J.; Elbourne, A.; Hunt, T.; Kent, B.; Kreuzer, M.; Strobl, M.; Steitz, R.; Bryant, G., Phase separation in a ternary DPPC/DOPC/POPC

- system with reducing hydration. *Journal of colloid and interface science* **2023**, *638*, 719-732.
222. Kučerka, N.; Gallová, J.; Uhríková, D.; Balgavý, P.; Bulacu, M.; Marrink, S.-J.; Katsaras, J., Areas of monounsaturated diacylphosphatidylcholines. *Biophysical Journal* **2009**, *97* (7), 1926-1932.
223. Ollila, S.; Hyvönen, M. T.; Vattulainen, I., Polyunsaturation in lipid membranes: dynamic properties and lateral pressure profiles. *The Journal of Physical Chemistry B* **2007**, *111* (12), 3139-3150.
224. Huang, C.-h.; Mason, J. T., Structure and properties of mixed-chain phospholipid assemblies. *Biochimica et Biophysica Acta (BBA)-Reviews on Biomembranes* **1986**, *864* (3-4), 423-470.
225. Chen, R.; Poger, D.; Mark, A. E., Effect of high pressure on fully hydrated DPPC and POPC bilayers. *The Journal of Physical Chemistry B* **2011**, *115* (5), 1038-1044.
226. Rosetti, C. M.; Montich, G. G.; Pastorino, C., Molecular insight into the line tension of bilayer membranes containing hybrid polyunsaturated lipids. *The Journal of Physical Chemistry B* **2017**, *121* (7), 1587-1600.
227. van der Veen, J. N.; Kennelly, J. P.; Wan, S.; Vance, J. E.; Vance, D. E.; Jacobs, R. L., The critical role of phosphatidylcholine and phosphatidylethanolamine metabolism in health and disease. *Biochimica et Biophysica Acta (BBA)-Biomembranes* **2017**, *1859* (9), 1558-1572.
228. Gumí-Audenis, B.; Costa, L.; Ferrer-Tasies, L.; Ratera, I.; Ventosa, N.; Sanz, F.; Giannotti, M. I., Pulling lipid tubes from supported bilayers unveils the underlying substrate contribution to the membrane mechanics. *Nanoscale* **2018**, *10* (30), 14763-14770.
229. Fessler, F.; Sharma, V.; Muller, P.; Stocco, A., Entry of microparticles into giant lipid vesicles by optical tweezers. *Physical Review E* **2023**, *107* (5), L052601.
230. Liu, X.; Auth, T.; Hazra, N.; Ebbesen, M. F.; Brewer, J.; Gompper, G.; Crassous, J. J.; Sparr, E., Wrapping anisotropic microgel particles in lipid membranes: Effects of particle shape and membrane rigidity. *Proceedings of the National Academy of Sciences* **2023**, *120* (30), e2217534120.
231. de Almeida, M. S.; Susnik, E.; Drasler, B.; Taladriz-Blanco, P.; Petri-Fink, A.; Rothen-Rutishauser, B., Understanding nanoparticle endocytosis to improve

- targeting strategies in nanomedicine. *Chemical Society Reviews* **2021**, *50* (9), 5397-5434.
232. Strachan, J. B.; Dyett, B. P.; Nasa, Z.; Valery, C.; Conn, C. E., Toxicity and cellular uptake of lipid nanoparticles of different structure and composition. *Journal of colloid and interface science* **2020**, *576*, 241-251.
233. Kubo, K.; Freitas-Astua, J. d.; Machado, M.; Kitajima, E. W., Orchid fleck symptoms may be caused naturally by two different viruses transmitted by *Brevipalpus*. *Journal of General Plant Pathology* **2009**, *75*, 250-255.
234. Mitragotri, S., Devices for overcoming biological barriers: the use of physical forces to disrupt the barriers. *Advanced drug delivery reviews* **2013**, *65* (1), 100-103.
235. Blanco, E.; Shen, H.; Ferrari, M., Principles of nanoparticle design for overcoming biological barriers to drug delivery. *Nature biotechnology* **2015**, *33* (9), 941-951.
236. Koltover, I.; Raedler, J. O.; Safinya, C. R., Membrane mediated attraction and ordered aggregation of colloidal particles bound to giant phospholipid vesicles. *Physical Review Letters* **1999**, *82* (9), 1991.
237. Cuvelier, D.; Chiaruttini, N.; Bassereau, P.; Nassoy, P., Pulling long tubes from firmly adhered vesicles. *Europhysics Letters* **2005**, *71* (6), 1015.
238. Tzima, E.; Del Pozo, M. A.; Shattil, S. J.; Chien, S.; Schwartz, M. A., Activation of integrins in endothelial cells by fluid shear stress mediates Rho-dependent cytoskeletal alignment. *The EMBO journal* **2001**, *20* (17), 4639-4647.
239. Ratajczak, A. M.; Sasidharan, S.; Gonzalez, X. I. R.; Miller, E. J.; Socrier, L.; Anthony, A. A.; Honerkamp-Smith, A. R., Measuring flow-mediated protein drift across stationary supported lipid bilayers. *Biophysical journal* **2023**, *122* (9), 1720-1731.
240. Karaz, S.; Senses, E., Liposomes Under Shear: Structure, Dynamics, and Drug Delivery Applications. *Advanced NanoBiomed Research* **2023**, 2200101.
241. Mo, J.; Simha, A.; Raizen, M. G., Brownian motion as a new probe of wettability. *The Journal of Chemical Physics* **2017**, *146* (13).
242. Panconi, L.; Lorenz, C.; May, R. C.; Owen, D.; Makarova, M., Phospholipid tail asymmetry allows cellular adaptation to anoxic environments. *bioRxiv* **2022**, 2022.08.04.502790.

243. Liu, S.-L.; Sheng, R.; Jung, J. H.; Wang, L.; Stec, E.; O'Connor, M. J.; Song, S.; Bikkavilli, R. K.; Winn, R. A.; Lee, D., Orthogonal lipid sensors identify transbilayer asymmetry of plasma membrane cholesterol. *Nature chemical biology* **2017**, *13* (3), 268-274.
244. Sackmann, E., Biological membranes architecture and function. *Structure and dynamics of membranes* **1995**, *1*, 1-63.
245. Zhang, Y.; Li, Q.; Dong, M.; Han, X., Effect of cholesterol on the fluidity of supported lipid bilayers. *Colloids and Surfaces B: Biointerfaces* **2020**, *196*, 111353.
246. Ribas, V.; García-Ruiz, C.; Fernández-Checa, J. C., Mitochondria, cholesterol and cancer cell metabolism. *Clinical and translational medicine* **2016**, *5* (1), 1-24.
247. Zhang, X.; Cheng, R.; Rowe, D.; Sethu, P.; Daugherty, A.; Yu, G.; Shin, H. Y., Shear-sensitive regulation of neutrophil flow behavior and its potential impact on microvascular blood flow dysregulation in hypercholesterolemia. *Arteriosclerosis, thrombosis, and vascular biology* **2014**, *34* (3), 587-593.
248. Wang, Y.; Gkeka, P.; Fuchs, J. E.; Liedl, K. R.; Cournia, Z., DPPC-cholesterol phase diagram using coarse-grained Molecular Dynamics simulations. *Biochimica et Biophysica Acta (BBA)-Biomembranes* **2016**, *1858* (11), 2846-2857.
249. Falck, E.; Patra, M.; Karttunen, M.; Hyvönen, M. T.; Vattulainen, I., Lessons of slicing membranes: interplay of packing, free area, and lateral diffusion in phospholipid/cholesterol bilayers. *Biophysical journal* **2004**, *87* (2), 1076-1091.
250. Róg, T.; Pasenkiewicz-Gierula, M., Cholesterol effects on a mixed-chain phosphatidylcholine bilayer: a molecular dynamics simulation study. *Biochimie* **2006**, *88* (5), 449-460.
251. Filippov, A.; Orädd, G.; Lindblom, G., The effect of cholesterol on the lateral diffusion of phospholipids in oriented bilayers. *Biophysical journal* **2003**, *84* (5), 3079-3086.
252. Alwarawrah, M.; Dai, J.; Huang, J., A molecular view of the cholesterol condensing effect in DOPC lipid bilayers. *The journal of physical chemistry B* **2010**, *114* (22), 7516-7523.
253. Plochberger, B.; Stockner, T.; Chiantia, S.; Brameshuber, M.; Weghuber, J.; Hermetter, A.; Schwille, P.; Schütz, G. J., Cholesterol slows down the lateral mobility of an oxidized phospholipid in a supported lipid bilayer. *Langmuir* **2010**, *26* (22), 17322-17329.

254. Bagheri, B.; Boonnoy, P.; Wong-Ekkabut, J.; Karttunen, M., Effect of oxidation on POPC lipid bilayers: anionic carboxyl group plays a major role. *Physical Chemistry Chemical Physics* **2023**, *25* (27), 18310-18321.
255. Maghraby, G. M. E.; Williams, A. C.; Barry, B. W., Skin hydration and possible shunt route penetration in controlled estradiol delivery from ultradeformable and standard liposomes. *Journal of Pharmacy and Pharmacology* **2001**, *53* (10), 1311-1322.
256. Hoepelman, I.; Schneider, M., Azithromycin: the first of the tissue-selective azalides. *International journal of antimicrobial agents* **1995**, *5* (3), 145-167.
257. Greenwood, D., *Antimicrobial drugs: chronicle of a twentieth century medical triumph*. OUP Oxford: 2008.
258. Hirsch, R.; Deng, H.; Laohachai, M., Azithromycin in periodontal treatment: more than an antibiotic. *Journal of periodontal research* **2012**, *47* (2), 137-148.
259. Haffajee, A. D.; Torresyap, G.; Socransky, S. S., Clinical changes following four different periodontal therapies for the treatment of chronic periodontitis: 1-year results. *Journal of clinical periodontology* **2007**, *34* (3), 243-253.
260. Gbinigie, K.; Frie, K., Should azithromycin be used to treat COVID-19? A rapid review. *BJGP open* **2020**, *4* (2).
261. Imamura, Y.; Higashiyama, Y.; Tomono, K.; Izumikawa, K.; Yanagihara, K.; Ohno, H.; Miyazaki, Y.; Hirakata, Y.; Mizuta, Y.; Kadota, J.-i., Azithromycin exhibits bactericidal effects on *Pseudomonas aeruginosa* through interaction with the outer membrane. *Antimicrobial agents and chemotherapy* **2005**, *49* (4), 1377-1380.
262. Cordeiro, M. M.; Filipe, H. A.; Santos, P. d.; Samelo, J.; Ramalho, J. P. P.; Loura, L. M.; Moreno, M. J., Interaction of Hoechst 33342 with POPC Membranes at Different pH Values. *Molecules* **2023**, *28* (15), 5640.
263. Kournoutou, G. G.; Dinos, G., Azithromycin through the Lens of the COVID-19 Treatment. *Antibiotics* **2022**, *11* (8), 1063.
264. Pradas, I.; Huynh, K.; Cabré, R.; Ayala, V.; Meikle, P. J.; Jové, M.; Pamplona, R., Lipidomics reveals a tissue-specific fingerprint. *Frontiers in physiology* **2018**, *9*, 1165.

265. Gerl, M. J.; Sampaio, J. L.; Urban, S.; Kalvodova, L.; Verbavatz, J.-M.; Binnington, B.; Lindemann, D.; Lingwood, C. A.; Shevchenko, A.; Schroeder, C., Quantitative analysis of the lipidomes of the influenza virus envelope and MDCK cell apical membrane. *Journal of Cell Biology* **2012**, *196* (2), 213-221.
266. Jurkiewicz, P.; Cwiklik, L.; Vojtíšková, A.; Jungwirth, P.; Hof, M., Structure, dynamics, and hydration of POPC/POPS bilayers suspended in NaCl, KCl, and CsCl solutions. *Biochimica et Biophysica Acta (BBA)-Biomembranes* **2012**, *1818* (3), 609-616.
267. Janosi, L.; Gorfe, A. A., Simulating POPC and POPC/POPG bilayers: conserved packing and altered surface reactivity. *Journal of chemical theory and computation* **2010**, *6* (10), 3267-3273.
268. Lu, L.; Doak, W. J.; Schertzer, J. W.; Chiarot, P. R., Membrane mechanical properties of synthetic asymmetric phospholipid vesicles. *Soft Matter* **2016**, *12* (36), 7521-7528.
269. Elani, Y.; Purushothaman, S.; Booth, P. J.; Seddon, J. M.; Brooks, N. J.; Law, R. V.; Ces, O., Measurements of the effect of membrane asymmetry on the mechanical properties of lipid bilayers. *Chemical Communications* **2015**, *51* (32), 6976-6979.
270. Karamdad, K.; Law, R.; Seddon, J.; Brooks, N.; Ces, O., Studying the effects of asymmetry on the bending rigidity of lipid membranes formed by microfluidics. *Chemical Communications* **2016**, *52* (30), 5277-5280.
271. Berquand, A.; Fa, N.; Dufrene, Y.; Mingéot-Leclercq, M.-P., Interaction of the macrolide antibiotic azithromycin with lipid bilayers: effect on membrane organization, fluidity, and permeability. *Pharmaceutical research* **2005**, *22*, 465-475.
272. Chen, T.; Gomez-Escoda, B.; Munoz-Garcia, J.; Babic, J.; Griscom, L.; Wu, P.-Y. J.; Coudreuse, D., A drug-compatible and temperature-controlled microfluidic device for live-cell imaging. *Open biology* **2016**, *6* (8), 160156.
273. Tyteca, D.; Schanck, A.; Dufrene, Y.; Deleu, M.; Courtoy, P. J.; Tulkens, P. M.; Mingéot-Leclercq, M.-P., The macrolide antibiotic azithromycin interacts with lipids and affects membrane organization and fluidity: studies on Langmuir-Blodgett monolayers, liposomes and J774 macrophages. *The Journal of membrane biology* **2003**, *192*, 203-215.

274. Montenez, J.-P.; Van Bambeke, F.; Piret, J.; Brasseur, R.; Tulkens, P. M.; Mingeot-Leclercq, M.-P., Interactions of macrolide antibiotics (Erythromycin A, roxithromycin, erythromyclamine [Dirithromycin], and azithromycin) with phospholipids: computer-aided conformational analysis and studies on acellular and cell culture models. *Toxicology and applied pharmacology* **1999**, *156* (2), 129-140.
275. Ackerman, D. G.; Feigenson, G. W., Lipid bilayers: clusters, domains and phases. *Essays in biochemistry* **2015**, *57*, 33-42.
276. Eid, J.; Razmazma, H.; Jraij, A.; Ebrahimi, A.; Monticelli, L., On calculating the bending modulus of lipid bilayer membranes from buckling simulations. *The journal of physical chemistry B* **2020**, *124* (29), 6299-6311.
277. den Otter, W. K.; Shkulipa, S., Intermonolayer friction and surface shear viscosity of lipid bilayer membranes. *Biophysical journal* **2007**, *93* (2), 423-433.

Acknowledgements

More than four years have passed since I embarked on my PhD journey, and it has been both challenging and deeply rewarding. Throughout this time, I have been fortunate to be supported by a number of remarkable individuals who have made this experience truly memorable. I would like to take this opportunity to express my gratitude to them:

First and foremost, I extend my heartfelt thanks to my supervisor, **Marie-Eve**. The support you've provided has gone beyond anything I could have imagined. Your trust in me and the opportunity to work on this project have been invaluable. Over the years, I have learned so much from you, and I greatly admire your kindness, patience, and support, especially your patience in listening to my musings beyond work.

I am also deeply grateful to **Gijse** for co-supervising this thesis. Our meetings have been an incredible source of energy, and I've always been inspired by your positivity.

Also, I want to express my sincere appreciation to **Daniel**. This thesis would not have come to fruition without your consultancy and the thorough, insightful feedback you provided on my measurement results.

Additionally, I would like to thank the **committee members**. Thank you for reviewing my PhD thesis and agreeing to participate in my PhD defense ceremony.

Djanick, you know how much I enjoyed your company, and probably you don't need this paragraph to be reminded of it. But, I would like to thank you for being a good friend and not just a colleague. I really like our friendship. I enjoyed the times we spent on- and off-campus and the talks and laughs we shared. I hope we can keep in touch also afterward as well. Also, thanks for being my coach in the gym. Without you, I probably wouldn't have lost even the few grams of weight I managed to shed.

Roland, thank you for all your teachings, technical solutions, and handling my numerous lipid orders. I understand how confusing their names can be. **Ramon**, I always admired your professional attitude toward the wet lab and safety while combining it with your delicate comedy style. Thank you also for your entertaining group activity plans and the candies!

Nemo, I truly appreciate all the time and effort you dedicated to teaching and training me for the cleanroom tests. You are indeed a true teacher. I greatly value your attention to the tiniest details and your strong sense of responsibility. I also greatly appreciate your patience in

answering all my technical questions. Some chapters of this thesis wouldn't have been possible without your kind and generous help.

I would also like to thank my students, **Daan, Martina, and Maria**. It was a great pleasure to collaborate with you. You are all very talented, hardworking, and motivated. I was always impressed by how well you handled technically challenging experiments. I wish you all a lot of success and happiness.

One of the most rewarding experiences during my PhD was meeting many new people in the MEA lab. I will always remember all the lab activities, funny lunch times, the extremely funny NWO conferences, and many other things. Thank you: **Franka** (and Tom for the beautiful marriage ceremony), **Likkitha** (I know you were always jealous of my lunch), **Horia** (and specifically your boat), **JJ** (Chetori?), **Fredrich** (I missed some history-related discussions), and specifically our MEA bouldering group (**Pang, Zan, Djanick, and Fan**) for all the nice times we experienced together. I specifically want to wish a successful PhD for **Zan and Pang**, I know how tricky it is to work with lipids and optical tweezers.

Specifically, I will always cherish the memories of the enjoyable times I had both on and off-campus with some of the **former MEA members: Samy, Ingo, Chaline, Josine, and Arjen**. I want to give a special thanks to **Samy** for being such a good friend. I truly appreciated our long, deep discussions, the funny moments we shared, and all the Hip-hop music we listened to together in the wet lab. I would also thank **Guillermo** for always answering my emails and questions I had at the beginning of my PhD. A special thank you also goes to **Kui** for being such a good colleague; I enjoyed your company and the guidance you were giving to me specifically at the beginning of my PhD.

I would like to thank many nice people in **BN and Civil engineering department**. A huge thank you to our BN Minecraft members, **Nemo** (creative mode cheater and server), **Reza, Ali, Yash, Jan** and specifically **Ramon**, my Minecraft housemate and companion, for all the Lan parties and the funny moments we had together. **Sam**, the Dutch Shams, it was a pivotal point when I met you. I really liked our spiritual and poetical talks and the off-campus activities we did together.

A huge thank you should also go to my friends in the civil engineering department. **Katerina, Stavros** (off-course I can make better kababs than you), **Yro, Lili, Eli, Yulong, Ajay, Chris, Avi, Cor, Ruxin, and Mahmoud**. All the parties, adventurous trips, and activities we did together will always remain in my mind.

Meanwhile, I want to thank my **off-campus friends** who made my life in the Netherlands amazing. **Kaveh, Nasrin, Rasoul, Negar, Babak Faezeh, Majid, Sepideh, Ashkan,**

Maedeh, Abbas, Sahar, Parviz, Zahra, Mohammad, and Faranak. I really enjoyed all the activities we had together. You are not just friends but somehow my family in the Netherlands. I also want to thank my game night friends and also my other friends for all the weekly sessions and outings we shared: **Marjan, Mohammad, Morteza, Saeed, Amirhossein, Azadeh, Hani, Arash, MJ, Alireza, Neda, Ahmad, Reza, Hamid, Sajjad, Soheila, Nima & Parisa** and many other wonderful people in the group.

Kiana, my dear sister, I want to thank you for all the emotional and spiritual support you have always given me. Also, I appreciate the time and effort you put helping me finding a PhD position. Thank you! I also want to thank my **family** members in Europe for their support and warm presence with me: **Uncle Shahin, Neda, Aunt Mahin, Aunt Nahid, Arash, Uncle Mami, and Sara.**

At this point, I would also like to thank my **parents**, and especially my mother, for her involvement in all stages of my education. **Maman**, this thesis is already dedicated to you. Without you, none of this would have been possible. It's hard to express in another language how much I owe you. I wish I could write a full book of poetry in sweet Persian to tell you how much I love you.

Finally, I want to express my deepest gratitude to my wife, **Sadaf**, for her unwavering support during this journey. Your warm hugs during my most stressful moments and the confidence you bestowed upon me were truly invaluable. Your presence was a soothing balm to my soul, alleviating the pain of being far from home. Of course, my appreciation for you extends far beyond the confines of this simple paragraph in my thesis.

Curriculum Vitae

Arash Yahyazadeh Shourabi

- | | |
|------------|--|
| 21-03-1995 | Born in Damavand, Greater Tehran, Iran |
| 2013-2017 | Bachelor in Mechanical Engineering
K.N.Toosi University of Technology, Tehran, Iran |
| 2017-2019 | Master in Mechanical Engineering
Sharif University of Technology, Tehran, Iran |
| 2021-2025 | PhD in Bio-nanoscience
Delft University of Technology, Delft, the Netherlands |

List of Publications

Papers:

- (1). **Yahyazadeh Shourabi, Arash**, Navid Kashaninejad, and Mohammad Said Saidi. "An integrated microfluidic concentration gradient generator for mechanical stimulation and drug delivery." *Journal of Science: Advanced Materials and Devices* 6.2 (2021): 280-290.
- (2). **Yahyazadeh Shourabi, A.**, Salajeghe, R., Barisam, M., & Kashaninejad, N. (2021). A Proof-of-Concept Study Using Numerical Simulations of an Acoustic Spheroid-on-a-Chip Platform for Improving 3D Cell Culture. *Sensors*, 21(16), 5529.
- (3). Nguyen, Ann V.#, **Arash Yahyazadeh Shourabi#**, Mohammad Yaghoobi, Shiyang Zhang, Kenneth W. Simpson, and Alireza Abbaspourrad. "A high-throughput integrated biofilm-on-a-chip platform for the investigation of combinatory physicochemical responses to chemical and fluid shear stress." *Plos one* 17, no. 8 (2022): e0272294
- (4). **Yahyazadeh Shourabi, A.**, Kieffer, R., de Jong, D., Tam, D., & Aubin-Tam, M. E. (2024). Mechanical characterization of freestanding lipid bilayers with temperature-controlled phase. *Soft Matter*, 20(42), 8524-8537.
- (5). **Yahyazadeh Shourabi**, Arash, Martina Iacona, and Marie-Eve Aubin-Tam. "Microfluidic system for efficient molecular delivery to artificial cell membranes." *Lab on a Chip* 25.7 (2025): 1842-1853.
- (6). **Yahyazadeh Shourabi, A.** & Aubin-Tam, M. Effect of lipid tail-asymmetry and cholesterol on the mechanical properties of freestanding planar lipid bilayers (Ready to submit)

Patents:

- (1). Microfluidic drug delivery to artificial cell-membranes (submitted, June/07/2024)
- (2). Passive microfluidic bubble-trapping (submitted, June/07/2024)



**Microfluidics for Biophysical
Studies on Artificial
Lipid Membranes**

Arash Yahyazadeh Shourabi